To James
my pillar of strength
and
the love of my life.

Hunter A. Knox
New Mexico Institute of Mining and Technology
May, 2012

ERUPTIVE CHARACTERISTICS AND GLACIAL EARTHQUAKE INVESTIGATION ON EREBUS VOLCANO, ANTARCTICA

by

Hunter A. Knox

Submitted in Partial Fulfillment

of the Requirements for the Degree of

Doctor of Philosophy in Earth and Environmental Science

with Dissertation in Geophysics

New Mexico Institute of Mining and Technology

Socorro, New Mexico

May, 2012

Out of the night that covers me,
Black as the pit from pole to pole,
I thank whatever gods may be
For my unconquerable soul.

In the fell clutch of circumstance
I have not winced nor cried aloud.
Under the bludgeonings of chance
My head is bloody, but unbowed.

Beyond this place of wrath and tears
Looms but the Horror of the shade,
And yet the menace of the years
Finds and shall find me unafraid.

It matters not how strait the gate,
How charged with punishments the scroll,
I am the master of my fate:
I am the captain of my soul.

Invictus by William Ernest Henley

ABSTRACT

This work investigates the seismic activity observed on Erebus volcano, Antarctica, through detailed analyses of two seismic databases. Chapter one presents the newly developed Strombolian eruption database, evidence for temporal evolution of seismic characteristics, and an expanded eruption model . Chapter two introduces the largest seismic event database created for Erebus volcano to date, examines the apparent seasonality seen in the seismic record, and evaluates cryoseismic sources. The appendices contain information for database reconstruction, station and shot metadata, an evaluation of individual station performance, and maps of the study area.

The newly developed Strombolian eruption catalog contains broadband seismograms of 2,974 eruptions originating in the persistent phonolitic lava lake. The catalog spans 8 years from 2003 through May of 2011. It was constructed using matched filter techniques, the similar eruption seismic characteristics, and the nearly decadal record from the Mount Erebus Volcano Observatory (MEVO) permanent seismic network. The catalog was examined for temporal changes in eruptive behavior as indicated by the timing of seismic observables. Cross-correlation analysis of the eruption events reveals systematically changing time lags (of up to several seconds) between the arrival of short period (SP) and associated post-eruptive very long period (VLP) signals. These timing variations are consistently observed at five broadband seismic stations. No obvious correlations between the time lags and eruption size, spectral characteristics, eruption frequency, SP and VLP waveform similarity, or lava lake morphology were apparent. The VLP-SP lag changes can be attributed to the sensitivity of the Strombolian eruptive system to conduit geometry changes occurring on time scales of weeks to months.

The non-eruptive seismic event database examines both long-running and temporary dense deployments of seismographs spanning seven years (2003-2009). The 84,317 seismic events are evaluated for general event frequency, seasonality, and geographic distribution. A subset of 166 well-observed icequakes recorded by the MEVO permanent network in consort with two dense IRIS PASSCAL-supported temporary networks (2007-2008) were further analyzed. Specifically these events were examined for size distribution, location, and event mechanisms consistent with the high-elevation (above 2000 m), cold (ambient air temperatures varying from $\sim$-10°C to $\sim$-60°C annually), and dry Antarctic glacial environment. A large number of icequake swarms (up to many hundreds of distinct impulsive events per day) were detected and show a highly seasonal pattern of occurrence. It is seen that $\sim$86% of the events occur between March and November each year. This annual time period is coincident with colder ambient air temperatures that arise due to the high latitude appearance and disappearance of the sun at the far southerly ($\sim$78°S) latitude of the volcano. The study concludes that most events occurring outside of the crater are brittle fracturing of the shallow firn/ice regime and that the seasonality represents the transition between ductile and brittle behavior of the medium.

Keywords: Erebus Volcano; Volcano Seismology; Glacier Seismology; Strombolian Eruptions

ACKNOWLEDGMENTS

I would first like to thank my advisor, Dr. Richard Aster, for teaching me that research is about ”constant forward progress”. A PhD is truly a marathon and his knowledge, guidance, insight, and support will forever be genuinely appreciated. I would also like to thank my committee members Dr. Philip Kyle, Dr. Jeff Johnson, Dr. Charlotte Rowe, and Dr. Ronald Thomas for significantly improving both the research and the manuscripts. It is true that it takes a village to raise a child. The research presented here was greatly aided by UNAVCO, the IRIS-PASSCAL Instrument Center at New Mexico Tech, IRIS, the National Science Foundation, the NSF Office of Polar Programs, the DOE National Nuclear Security Administration, Raytheon Polar Services Company, Extreme CCTV, Video-Comm Technologies, and New Mexico Tech. Grants that supported this research include ANT-0538414 and ANT-0838817. Finally, I would like to thank all of the MEVO researchers past and present.

An enormous amount of thanks goes out to my family and friends who encouraged and supported me throughout this process. I am fortunate enough to say that there are too many of you to list here, but you know who you are and that I am eternally grateful. My greatest thanks goes to my wonderful husband James. This work is dedicated to him.

This dissertation was typeset with LaTeX[1] by the author.

---

[1] The LaTeX document preparation system was developed by Leslie Lamport as a special version of Donald Knuth's TeX program for computer typesetting. TeX is a trademark of the American Mathematical Society. The LaTeX macro package for the New Mexico Institute of Mining and Technology dissertation format was written for the Tech Computer Center by John W. Shipman.

CONTENTS

LIST OF TABLES

LIST OF FIGURES

This dissertation is accepted on behalf of the faculty of the Institute by the following committee:

Richard Aster, Advisor

I release this document to the New Mexico Institute of Mining and Technology.

Hunter A. Knox Date

INTRODUCTION

Volcano monitoring has always been challenged by the differentiation between seismic events relating to volcanic activity and those related to either background noise or other interesting but unrelated phenomena. This is especially the case on glaciated volcanoes, both dormant and active, where the majority of all transient signals may not be associated with volcanic processes [e.g., *McNutt*, 2002]. The problem is often further complicated by the highly heterogeneous structure intrinsic to volcanoes, as seismograms may be very strongly influenced by path or site effects [*Wegler*, 2004].

Background

The persistently active Erebus volcano, along with its surrounding extinct volcanoes, form Ross Island, Antarctica. The Inner Crater of the volcano has hosted a convecting phonolitic lava lake for at least 40 years [*Giggenbach et al.*, 1973; *Kaminuma*, 1994; *Caldwell and Kyle*, 1994; *Aster et al.*, 2003; *Wright and Pilger*, 2008]. Strombolian eruptions from the lava lake and adjacent vents have dominated the eruptive and seismic activity of the volcano. During its active periods (most recently 2006-2007), Erebus volcano produces five or more Strombolian eruptions per day, with as many as 50 or more events per week. The eruptions are characterized by large gas slugs buoyantly rising from depth and exploding at the lava lake surface [e.g., *Aster et al.*, 2003; *Gerst*, 2010]. A persistent open-conduit situation is indicated by ongoing degassing and a general lack of internal long period or volcano-tectonic seismic sources [e.g., *Rowe et al.*, 2000].

Previous studies related to the seismic structure of Mount Erebus have incorporated several refraction seismic surveys, local earthquake studies, teleseismic studies, and velocity modeling of the magma conduit. This work began in 1974 with the deployment of a temporary five-station seismic network [*Dibble et al.*, 1994]. These instruments recorded local controlled source explosions during their deployment and were used to determine apparent velocity results ranging from 1.4 to 1.8 km/s in the upper 300 m of material surrounding the crater (out to $\sim$ 1.25km) [*Kyle et al.*, 1982; *Dibble et al.*, 1984].

In 1980, four permanent telemetry short period seismic stations were deployed by the International Mount Erebus Seismic Study (IMESS). During the 1981-1982 field season, 162 earthquake events were recorded on the array. These events were used to infer a best-fit homogeneous volcano model with a velocity of 2.1 km/s [*Shibuya et al.*, 1983]. *McGinnis et al.* [1983] measured seismic refraction velocities within McMurdo Sound near the flanks of Mount Erebus. Their results showed velocities ranging between 2 to 4.7 km/s in a 3-km thick Cenozoic layer, underlain by the seismic basement with velocities ranging between 5 and 6.5 km/s. This study was relevant to the velocity structure of Mount Erebus and Ross Island because the Cenozoic layer is older than Mount Erebus and presumably underlies the volcano [*Moore and Kyle*, 1987]. *Dibble et al.* [1984] estimated a vertical velocity of 4.5 ± 1.3 km/s through Mount Erebus using teleseisms and estimated an apparent velocity of 7.5 km/s below the basement using the data acquired from a shot located 40 km from the Erebus seismic network. Unfortunately, due to significant errors in the shot time, the depth of the material below the basement was not well constrained.

Small-scale and large-scale seismic studies were conducted through a series of field campaigns in the 1980s and 1990s. This included three seismic refraction lines located at the Lower Hut, the Upper Hut, and Tower Ridge [*Dibble et al.*, 1994]. In the 1984 field season, IMESS conducted an active seismic survey consisting of nine shots fired in crevasses and in the sea. The energy from these detonations was recorded on an eight station seismic network [*Dibble et al.*, 1994; *Rowe*, 1988]. Also, beginning in 1986, volcanic explosions were analyzed using timed video surveillance to provide further constraints on material near the crater [*Dibble et al.*, 1994].

Utilizing the above referenced surveys and their associated data (shots and eruptions), *Dibble et al.* [1994] and *Rowe* [1988] determined the bulk velocity model for Mount Erebus. The model contains a permafrost layer that has a velocity of approximately 3 km/s, and is sometimes underlain by a thin layer with significantly lower velocities (approximately 1.0 to 2 km/s). These velocities and depths, which were determined using eruptions from 1986 and 1988, are spatially variable but generally apply to the top 360 m of material near the crater. The next layer in the sequence was determined to have a velocity of 4.1- 4.3 km/s and a thickness of up to 5.5 km. It is believed that this layer is constructed of massive phonolitic lava flows. The Cenozoic sediments that are present in the McMurdo Sound constitute the next layer. The velocity of these sediments must be adjusted for the load of the volcano, and are therefore determined to be approximately 2.5 to 5.5 km/s with a thickness likely ranging between 3 and 4 km. The final layer developed through the combined studies is that of the basaltic basement rock, which likely has a velocity 6.5 km/s [*Dibble et al.*, 1994 and *Rowe*, 1988].

Dibble [1994] calculated the velocity structure of the magma column in the conduit underlying the lava lake for various water contents and surface porosities by constraining near-surface vesicularity using lava bombs and producing realistic bubble growth models, . The best fit model has 0.5% water, 75% surface porosity, and a 10 m explosion depth [*Dibble*, 1994]. One of the most important results from this study is the convergence of the velocity at depth to approximately 2 km/s. This velocity is considerably slower than the P-wave velocity (4.1 km/s) associated with the same depths [*Dibble et al.*, 1994]. It is important to note that there are two fundamental assumptions made in the calculation of this magma conduit velocity model. First, the model assumes that the magma column is laterally homogeneous, which is likely an oversimplification. The second assumption pertains to the theory for the velocity-depth curves used. The curves assume small bubble fractions and become unreliable when high bubble fractions are present [*Dibble*, 1994]. If higher bubble fractions are present in the Erebus magma column, then the velocity depression could be less than the model accounts for.

Other relevant studies include those conducted to investigate the very long period (VLP) oscillations of Erebus volcano. The results of moment tensor analysis, Mogi modeling, gravity, body, and surface wave studies, tilt measurements, and flow models suggest that the summit magmatic system is large and complex, as reflected in the multiplicity of summit eruptive vents [*Aster et al.*, 2003; *Aster et al.*, 2008]. This is supported by recent tomographic [*Zandomeneghi et al.*, 2011] and scattering inversion [*Chaput et al.*, 2012] results, which indicate that the uppermost conduit system of the volcano is indeed geometrically complicated. Gas measurements between the lava lake and a second ephemeral lava lake, Werner's Fumarole, furthermore support a complicated multithreaded conduit system in the summit region [*Oppenheimer and Kyle*, 2008].

Volcano monitoring at Erebus volcano prior to late 2001 largely used short period (∼1 Hz and higher) seismic and infrasonic instrumentation [*Dibble et al.*, 1994]. Early studies noted both a great number (>100s per year) Strombolian eruption signals and a variety of earthquake types, including large numbers of presumed icequakes [*Kaminuma* 1994]. In 2001 a broadband reference digital seismic network deployment was initiated with the installation of a broadband seismic station at E1S and a video surveillance system. The configuration of the current "permanent" network was largely in place with unified sample rates, locations, and battery life to optimize power through most of the austral winter by 2004 [*Aster et al.*, 2004]. This network facilitated higher dynamic range analysis of all events and broadband study of a number of non-eruptive signals, including regional iceberg-generated tremor [*MacAyeal et al.*, 2006]. During the 2007/2008 field season, 24 broadband stations were deployed in two concentric rings around the vertical axis of the volcano as part of a tomographic imaging effort on the upper volcano. These imaging efforts continued into the 2008-2009 field season, when 99 short period stations were deployed in the summit region and along the Terror-Erebus axis of Ross Island. This dense network allowed for the detection and location of a much greater number and diversity of events.

Objectives

The principle objectives of this study were: 1) develop techniques useful for discriminating between volcanic and glacier related seismicity on Erebus volcano, 2) construct two distinct databases containing these signals, 3) investigate eruptive activity on a nearly decadal scale, and 4) determine the source mechanism, location, and general seismic characteristics of icequakes observed on the volcano. This endeavor required the use of matched filter techniques, Antelope database tools, and earthquake methodologies. All of which are documented throughout this work.

Content

This dissertation is comprised of two independent and self-contained sections. The first chapter (Chapter 1) examines the timing between the onset of the Very Long Period (VLP) seismic signal and the Short Period (SP) seismic signal for temporal changes. It uses a newly constructed database of 2,974 Strombolian eruptions originating at the Erebus lava lake. The VLP and SP seismic signals can be attributed to different processes before, during, and after an eruption. The second section (Chapter 2) discusses the investigation of icequakes/firnquakes frequently observed on Erebus volcano. This study examines the seismic characteristics, seasonality, locations, and sizes of a database of 84,317 events in order to determine the source mechanism and depth. Finally, this work concludes with detailed Appendices, which document the specifics of the research . They include a detailed discussion of the matched filter, eruption databases, plotting and processing codes, metadata for all stations, station performance measurements, Antelope Database specifics, and GMT Maps.

Coworker Contributions

This work contains many maps of Ross Island and the summit region that were created with the help of Dr. Jonathan MacCarthy, who developed the GMT codes to load and display a Digital Elevation Model (DEM). The construction of the matched filter was a collaborative effort between Julien Chaput and the author. All parts of the research and associated work were equally divided between the individuals. The Antelope Database construction was greatly aided by the employees of IRIS PASSCAL and their training courses. The Antelope Database itself was created entirely by the author. The Antelope Database processing was aided by Dr. Natalie Balfour, who helped the author adjust the STA/LTA detectors and the associators so that the processing would work properly and the project goals would be achieved. All other processing in Antelope was conducted solely by the author. Two codes previously developed by Dr. Richard Aster and Brent Henderson were expanded and used to process the data for the VLP study. Most of the results, however, were obtained using code written by the author. Dr. Richard Aster wrote the code for the Fourier fit used in Chapter 2. All other research, unless otherwise noted, was conducted by the author.

References

Aster, R., S. Mah, P. Kyle, W. McIntosh, N. Dunbar, J. Johnson, M. Ruiz, and S. McNamara (2003), Very long period oscillations of Mount Erebus Volcano, *J. Geophys. Res., 108* (B11), 2522, doi:10.1029/2002JB002101.

Aster, R., et al. (2004), Real-time data received from Mount Erebus Volcano, Antarctica, *Eos Trans. AGU, 85* (10), 97, doi:10.1029/2004EO100001.

Aster, R., D. Zandomeneghi, S. Mah, S. McNamara, D. B. Henderson, H. Knox, and K. Jones (2008), Moment tensor inversion of very long period seismic signals from Strombolian eruptions of Erebus Volcano, *J. Volcanol. Geotherm. Res., 177* (3), pp. 635-647, doi:10.1016/j.jvolgeores.2008.08.013.

Caldwell, D., and P. R. Kyle (1994), Mineralogy and geochemistry of ejecta erupted from Mount Erebus, Antarctica between 1972 and 1986, in *Volcanological and Environmental Studies of Mount Erebus, Antarctica, Antarct. Res. Ser.*, vol. 66, edited by P. Kyle, pp. 147-162, AGU, Washington, D. C.

Chaput, J., R. Aster, D. Zandomeneghi, H. Knox, and P. Kyle (2011), 3-D reflectivity model of shallow magmatic structure using body wave seismic interferometry applied to Strombolian eruption coda for Erebus Volcano, *Eos Trans. AGU*, Fall Meet. Suppl.

Dibble R., J. Kienle, P. Kyle, and K. Shibuya (1984), Geophysical studies of Erebus Volcano, Antarctica, from 1974 December to 1982 January, *N.Z.J. Geol. Geophys.*, 27, pp. 425-455.

Dibble, R., B. OBrien, and C. Rowe (1994), The velocity structure of Mount Erebus, Antarctica, and its lava lake, in *Volcanological and Environmental Studies of Mount Erebus, Antarctica, Antarct. Res. Ser.*, vol. 66, edited by P. Kyle, pp. 1-16, AGU, Washington, D. C.

Dibble, R. (1994), Velocity modeling in the erupting magma column of Mount Erebus, Antarctica, in *Volcanological and Environmental Studies of Mount Erebus, Antarctica, Antarct. Res. Ser.*, vol. 66, edited by P. Kyle, pp. 17-33, AGU, Washington, D. C.

Gerst, A. (2010), The First Second of a Strombolian Volcanic Eruption, Dissertation (Doctorate in Natural Sciences), Institute of Geophysics, University of Hamburg, Germany.

Giggenbach, W., P. Kyle, and G. Lyon (1973), Present volcanic activity on Mt. Erebus, Ross Island, Antarctica, *Geology, 1*, pp. 135-136.

Kaminuma, K. (1994), The Seismic Activity of Mount Erebus in 1981-1990, in *Volcanological and Environmental Studies of Mount Erebus, Antarctica, Antarct. Res. Ser.*, vol. 66, edited by P. Kyle, pp. 35-50, AGU, Washington, D. C.

Kyle, P. R., R. R. Dibble, W. F. Giggenbach, and J. Keys (1982), Volcanic activity associated with anorthoclase phonolite lava lake, Mount Erebus, Antarctica, in *Antarctic Geoscience*, edited by C. Craddock, pp. 734-745, University of Wisconsin Press, Madison.

MacAyeal, D. R., E. Okal, R. Aster, and J. Bassis (2008), Seismic and hydroacoustic tremor generated by colliding icebergs, *J. Geophys. Res., 113*, F03011, doi:10.1029/2008JF001005.

McGinnis, L., D. Wilson, W. Burdelik, and T. Larson (1983), Crust and upper mantle study of McMurdo Sound, in *Antarctic Earth Science*, edited by R. L. Oliver, P. R. James, and J. B. Jago, pp. 204-208, Australian Academy of Science, Canberra.

McNutt, S. R. (2002), Volcano seismology and monitoring for eruptions, in *International Handbook of Earthquake and Engineering Seismology, Int. Geophys. Ser.*, vol. 81, chap. 25, pp. 383 - 406, edited by W. H. Lee et al., Elsevier, New York.

Moore, J. and P. Kyle (1987), Volcanic geology of Mt. Erebus, Ross Island, Antarctica, *Proc. NIPR Symp. Antarct. Geosci., 1*, pp. 46-65.

Rowe, C. (1988), Seismic velocity structure and seismicity on Mount Erebus Volcano, Ross Island, Antarctica, M.S. thesis, University of Alaska, Fairbanks.

Rowe, C. A., R. C. Aster, P. R. Kyle, R. R. Dibble, and J. W. Schlue (2000), Seismic and acoustic observations at Mount Erebus Volcano, Ross Island, Antarctica, 1994-1998, *J. Volcanol. Geotherm. Res. 101* (1-2), pp. 105-128, doi:10.1016/S0377-0273(00)00170-0.

Shibuya, K., M. Baba, J. Kienle, R. Dibble, and P. Kyle (1983), Study of the seismic and volcanic activity of Mount Erebus, Antarctica, 1981-1982, in *Proceedings of 3rd Symposium on Antarctic Geoscience, Mem. Natl. Inst. Polar Res. Tokyo Spec. Issue, 28*, pp. 54-66.

Wegler, U. (2004), Diffusion of seismic waves in a thick layer: Theory and application to Vesuvius Volcano, *J. Geophys. Res., 109*, B07303, doi:10.1029/2004JB003048.

Wright, R. and E. Pilger (2008), Satellite observations reveal little inter-annual variability in the radiant flux from the Mount Erebus lava lake, *J. Volcanol. Geotherm. Res. 177* (3), pp. 687-694, doi:10.1016/j.jvolgeores.2008.03.005.

Zandomeneghi, D., R. Aster, A. Barclay, J. Chaput, and P. Kyle (2011), Tomographic high-resolution 3D imaging of the shallow magmatic system of Erebus Volcano, Antarctica, *Eos Trans. AGU*, Fall Meet. Suppl.

CHAPTER 1

MULTIYEAR TIMING VARIATIONS BETWEEN SHORT PERIOD AND VERY LONG PERIOD STROMBOLIAN ERUPTION SEISMOGRAMS: EVIDENCE FOR UPPER CONDUIT GEOMETRY CHANGES AT EREBUS VOLCANO, ANTARCTICA

Abstract

Broadband seismograms of 2,974 Strombolian eruptions from Erebus volcano are used to investigate temporal changes in eruptive dynamics across an eight-year period (2003-2011). Cross-correlation analysis of these seismograms reveals changing time lags between associated short period (SP) and extended (minutes) very long period (VLP) signals of up to $\sim \pm 1$ s on time scales of weeks to months. The timing variations are consistently observed at five seismic stations, and show no discernible dependency on eruption size, spectral characteristics, eruption frequency, SP and VLP waveform similarity, instrumentation environment, or lava lake morphology. We suggest that changing delays between the lava lake eruption origin (represented by the SP seismic signal) and the subsequent refilling of the conduit system (represented by the stable post-eruptive VLP seismic signal) arise from variable elastodynamic communication velocity in the magma-filled upper conduit system. We further propose that associated variable communication velocities are driven by geometry changes (e.g., thinning or thickening) that influence the speed of trapped seismic waves propagating between the lava lake and the VLP source centroid, which prior moment tensor inversion work suggests resides at a depth of ~450 m and is offset from the lava lake by several hundred m.

1.1 Introduction

The timing, duration, moment tensor characterization, and spectral characteristics of Very Long Period (VLP) seismic signals provide important clues into the nature of magmatic and gas transport in volcanic systems. For these reasons, VLP seismic signals associated with eruptions have been studied at volcanoes world-wide and on laboratory scales [e.g., *Rowe et al.*, 1998; *Aster et al.*, 2000; *Nishimura et al.*, 2000; *Chouet et al.*, 2003; *D'Auria and Martini*, 2008; *O'Brien and Bean*, 2008; *Lyons and Waite*, 2011].

Many VLP seismic studies constrain source mechanisms and examine conduit geometries using moment tensor inversions and other seismic waveform-based analyses. Although the mechanism specifics and inferred conduit geometric constraints differ from location to location, it is clear that VLP sources can involve fluid flow [e.g., *Nishimura et al.*, 2000], slow elastic/viscous fracture guided waves [e.g., *Ferrazzini and Aki*, 1987] and/or pressure transients [e.g., *Lyons and Waite*, 2011] within a network of cracks and conduits occurring pre-, syn-, and post-eruption.

Proposed source mechanisms for pre-eruptive VLP signals vary, and include mechanisms as diverse as gas slug formation and ascent [*Chouet et al.*, 2003] and degassing-driven crystallization followed by brittle failure [*Lyons and Waite*, 2011]. Post-eruptive VLPs have been attributed to mechanisms such as a repressurization of the conduit through either slumping of a magmatic film [*Chouet et al.*, 2003] or recharge of fresh magma [*Aster et al.*, 2003; *Lyons and Waite*, 2011], and slow trapped body waves [*Garces et al.*, 2000].

Although many VLPs are repeatable, and are thus associated with a self-reconstructing mechanism, systematic changes in timing, location, and frequency have been previously noted (for example, *Giudicepietro et al.* [2009] evaluated changes in the VLP source location, amplitude, and occurrence rate during 2007 at Stromboli). VLP changes have been modeled and/or hypothesized to reflect evolution in conduit geometry, the ability to sequester large gas slugs, and/or fluid dynamic processes that directly affect magmatic transport in the absence of measurable geochemical changes [*Rowe et al.*, 1998; *Aster et al.*, 2003; *Chouet et al.*, 2003; *James et al.*, 2006; *D'Auria and Martini*, 2008].

In this study, we document and discuss seismological observations of temporal changes in lava lake Strombolian eruption seismogram characteristics at Erebus volcano and use this information to infer changes in the shallow magmatic conduit system. The changes are observed in the relative timing of lava lake eruption (explosion) short period (SP) signals and the ubiquitously associated VLP signals, both of which exhibit high degrees of event-to-event similarity. The nature of this change is a progressive variation, with time scales of weeks to months.

1.2 Erebus volcano

Erebus volcano, a large active stratovolcano, along with its surrounding extinct volcanoes, forms Ross Island, Antarctica [*Giggenbach et al.*, 1973; *Kyle et al.*, 1982; *Kaminuma*, 1994]. The summit cone consists of an approximately 500 by 600 by 120 m deep elliptical Main Crater, which hosts a smaller Inner Crater containing a phonolitic lava lake and other vents. The lava lake has been a persistent feature for at least 40 years [*Giggenbach et al.*, 1973; *Caldwell and Kyle*, 1994; *Wright and Pilger*, 2008], thus indicating a remarkably stable near-summit magma-filled conduit system.

Conduits terminating in lava lakes are rare (with some other notable examples of various persistence being Erta Ale, Nyiragongo, Ambrym, and Villarica). Such systems are commonly associated with open conduit conditions that easily release internal pressurization and gas flux, and which exhibit bubble-initiated surface disturbance [*Bouche et al.*, 2010] and convection. An extraordinarily open-conduit conceptualization of the magmatic system at Erebus is supported by a general lack of internal seismic sources at the volcano [e.g. *Rowe et al.*, 2000] and persistent low-level eruptive activity.

During its most active recent periods (e.g., during 2005-2007), Erebus volcano has produced five or more Strombolian eruptions per day, with as many as 50 or more events per week. These eruptions are characterized by a largely intact, conduit or near conduit-spanning gas slug decompressing and buoyantly rising to the surface of the lava lake where it explodes (Figure 1.1). The emerging and exploding gas slugs have been observed via video and doppler radar at a distance of $\sim$350 meters and commonly have diameters on the order of tens of meters at emergence [*Dibble*, 1994; *Aster et al.*, 2003; *Johnson et al.*, 2003; *Dibble et al.*, 2008; *Gerst*, 2010].

Eruption monitoring prior to 2001 was largely accomplished with a robust telemetered short period (1 Hz seismometers) seismic and infrasonic network [*Dibble et al.*, 1994]. Construction of a broader-band digital seismic network using Guralp 40-T (30 s) seismometers began in 2001. By the 2003-2004 field season, the current configuration of the permanent network was achieved with unified sample rates, locations, state-of-health and environmental data streams, and optimized battery life providing power through at least a portion of the austral winter [Figure 1.2; *Aster et al.*, 2004]. We utilize data from this network in this study.

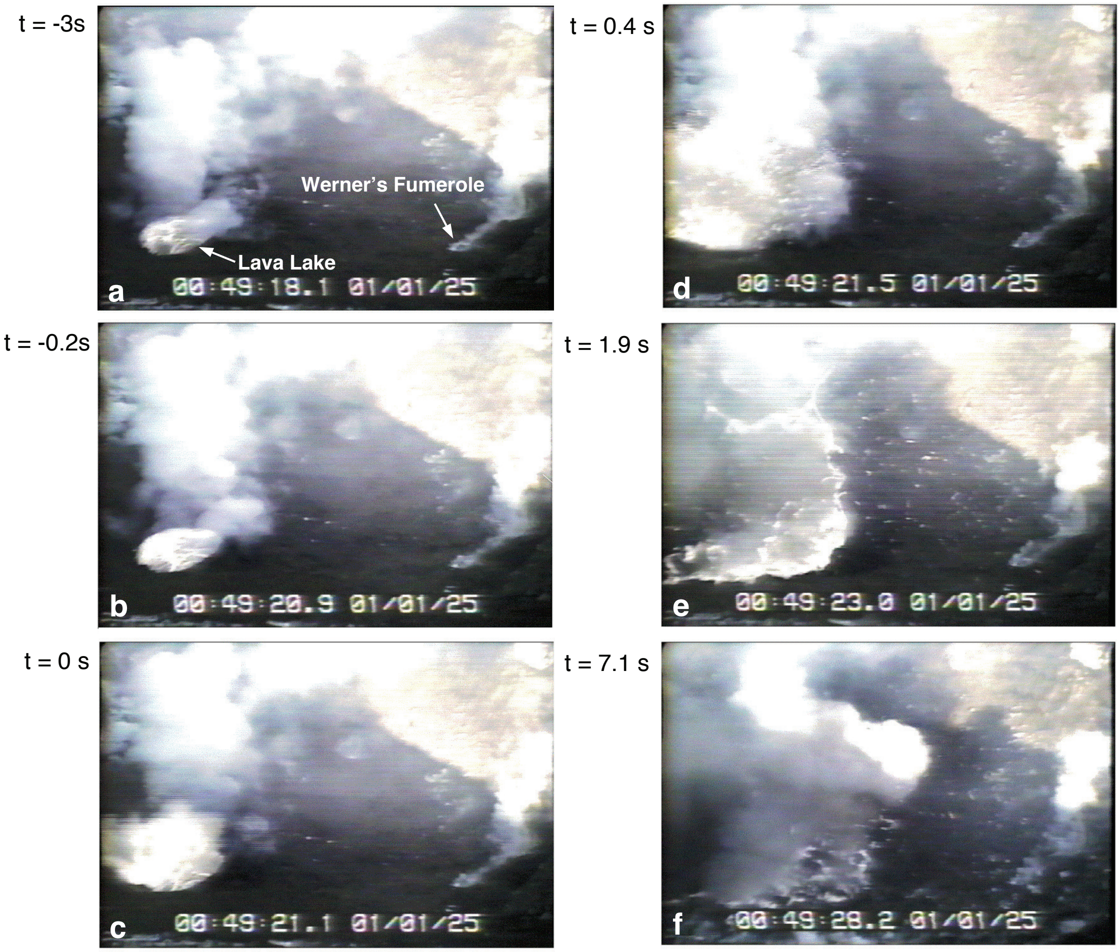

Figure 1.1: Characteristic Erebus lava lake eruption from January 25, 2001 viewed in false IR color from the VID video camera site (Figure 1.2). Times are relative to the SP origin time that is defined as occuring at slug burst (frame c). The field of view spans ∼100 m of the crater floor. After *Aster et al.* [2003]. An ephemeral Inner Crater secondary lava lake, Werner's Fumerole, is also labeled.

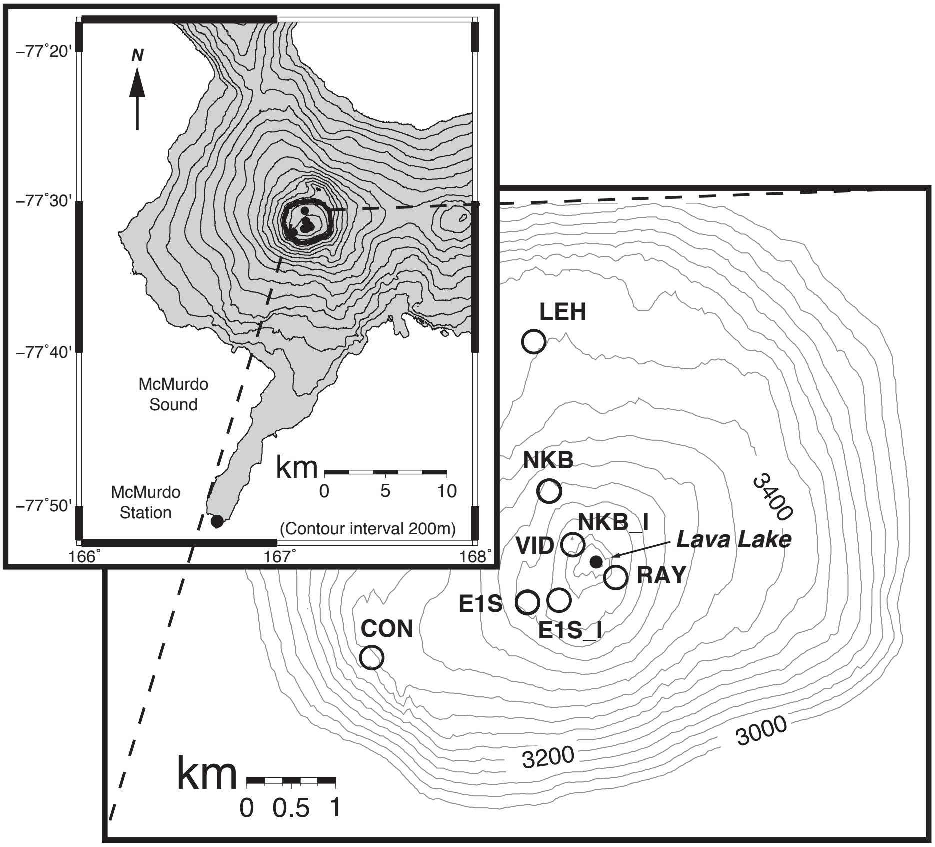

Figure 1.2: Digital elevation model of Erebus volcano (inset contour interval 50 m) . Circles show seismic and infrasound stations (denoted by the suffix I) used in this study. Video data from the camera site (VID) was used to monitor eruptive behavior and the state of the lava lake. The camera is co-located with the infrasound sensor NKB_I. The RAY seismic and infrasound stations were approximately co-located, and are therefore represented only by RAY. Only ∼4 y of RAY seismic data exists because the station was destroyed by an eruption in 2007.

1.3 Seismic Characteristics and Event Detection

1.3.1 Seismic Characteristics

Two distinct eruption-related seismic signals that occupy distinct frequency bands are observed at Erebus volcano in association with lava lake eruptions that we refer to here as SP and VLP signals [*Aster et al.*, 2003]. Because the eruptions are small and the noise levels on Ross Island can be high, both signals are best jointly recorded at ranges less than about 2 km from the lava lake. Beyond this range the near-field VLP signal becomes especially difficult to observe without substantial event stacking because of low amplitude oceanic microseism noise.

The SP signal consists primarily of elastic body waves generated by highly impulsive Strombolian eruptions [e.g., *Rowe et al.*, 2000; *Chaput et al.*, 2012; Figure 1.1] with dominant frequencies between 1 and 8 Hz. These signals are accompanied by strong infrasonic signals (up to tens of Pa in peak pressure amplitude at ranges of 1 km) with similar frequency content [e.g., *Jones et al.*, 2008]. The SP seismic energy is strongly scattered by the heterogeneous volcano; when seismograms are filtered above $\sim$1 Hz, they ubiquitiously display highly emergent first motions and a robust coda that persists above background noise for 30 s or longer [*Aster et al.*, 2003].

The VLP signals associated with Strombolian eruptions at Erebus volcano can be usefuly classified as consisting of pre-eruptive and post-eruptive segments. The pre-eruptive VLP signal, which can last up to several s, is generated by the decompressing gas slug interacting with the conduit walls and displacing magma as it ascends to the surface of the lava lake. Polarity and amplitude characteristics of this phase are variable [e.g., *Aster et al.*, 2003]. The post-eruptive

VLP signal is much more repeatable and exhibits well resolved stable and distinct nonharmonically related modal spectral components with periods near 8, 11, and 21 s [e.g., *Rowe et al., 1998*]. Stacking a large number of events reveals additional shorter period VLP spectral components [*Aster et al.*, 2003]. These spectral modes have been hypothesized to represent superimposed low-Q resonant periods of a surging oscillatory refill system that become excited when the system is gravitationally perturbed by eruptive mass removal from the conduit tip [*Aster et al.*, 2003; 2008a]. This is supported by the observation that stacked VLP signals persist for over 400 s, and cease when the lava lake is restored to its pre-eruptive level [*Aster et al.*, 2003].

1.3.2 Event Detection

To detect and catalog eruptions, a correlation-based multichannel matched filter [e.g., *Shearer*, 1994] was designed to scan the continuous archived data. The filter retrieves events based on the moving-window correlation between continuous data streams and the multichannel template. The template (Figure 1.3) was created by stacking bandpass filtered (2 - 6 Hz) high signal-to-noise eruption seismograms and infrasound channels at individual stations while preserving their characteristic interstation timing. The template is then correlated against continuous multichannel data to detect events. We do not use the VLP band for detection purposes because it is commonly obscured by the similar period microseism.

As seen in Figure 1.3, seismic signals from six stations were used in the construction of the template; locations for five of these stations are shown in Figure 1.2. The other seismic station (HOO) was not used for the detailed study presented here, since, although it records SP signals, the near-field VLP signal

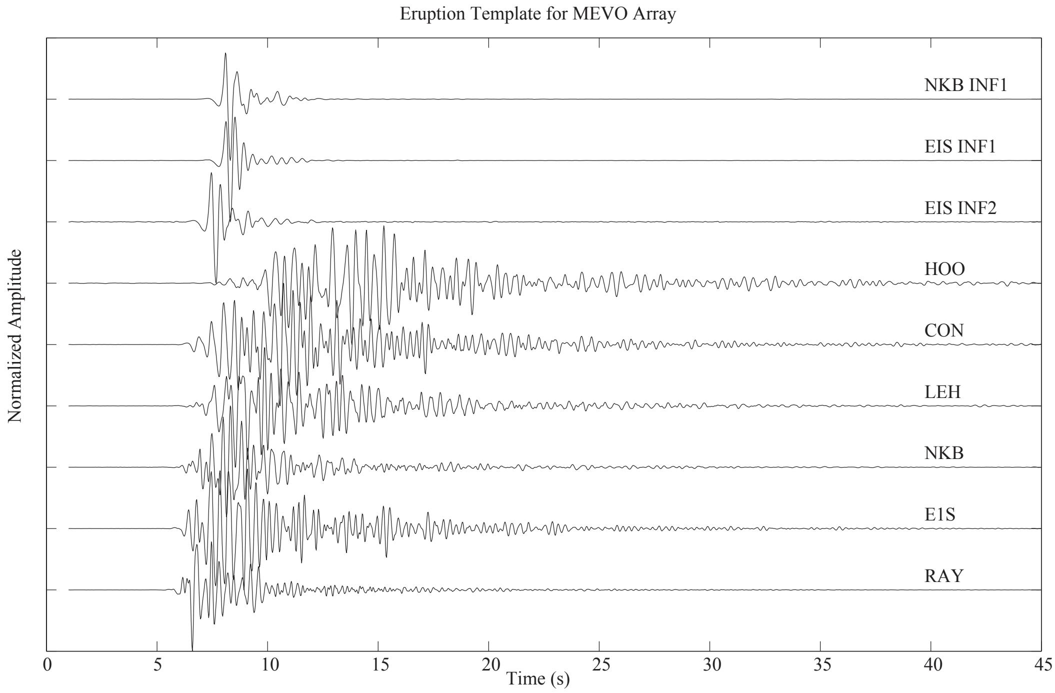

Figure 1.3: 9-channel matched filter template used for scanning continuous data for eruption detection from 2003 through 2011. Seismic channels are vertical-component and INF channels are infrasound sites. All of these seismic signals have been self-scaled for plotting and have been zero-phase filtered between 2 and 6 Hz to optimize SP band signal-to-noise.

Table 1.1: Matched Filter: Event Correlation Statistics

Station	Mean Correlation Coefficient	Variance
E1S	0.5398	0.0173
CON	0.4869	0.0229
NKB	0.6175	0.0288
RAY	0.5483	0.0319
LEH	0.4816	0.0282

is poorly resolved at its distant location from the lava lake (∼5.6 km). Three infrasound stations were also included in the matched filter template (Figure 1.2; Figure 1.3).

Correlation analyses of the 20 eruptions used to create the template are shown in Table 1.1. The mean correlation coefficients for the event pairs recorded at an individual seismic station are in the 0.4 to 0.6 range, with variances up to 0.03. The correlation coefficients were calculated using 45 s of the seismic signal and 25 s of the infrasound signal. The mean correlations for the infrasound signals were ∼0.6 with a variance of ∼0.03.

Upon the final construction of the matched filter template, we began processing identically band-passed continuous data to produce an eruption catalog. The correlation criteria for a detection was 0.16 between the template and continuous data, with at least three of the nine channels being operational. Although this threshold may seem low, the background levels were typically around 0.005 for the multichannel correlation coefficient. Once the catalog was constructed, we systematically verified that we had detected only eruptions and that we were detecting all of the clear events in random time periods. Final review of the events, both detected and in the continuous record, was conducted using move-out criteria and the diagnostic infrasound signal. In the end, a catalog of 2,974 lava lake eruption events was constructed and is analyzed here (Figure 1.4; the event-by-event similarity of SP band seismograms can also be seen in the aligned seismograms of Figure 1.9).

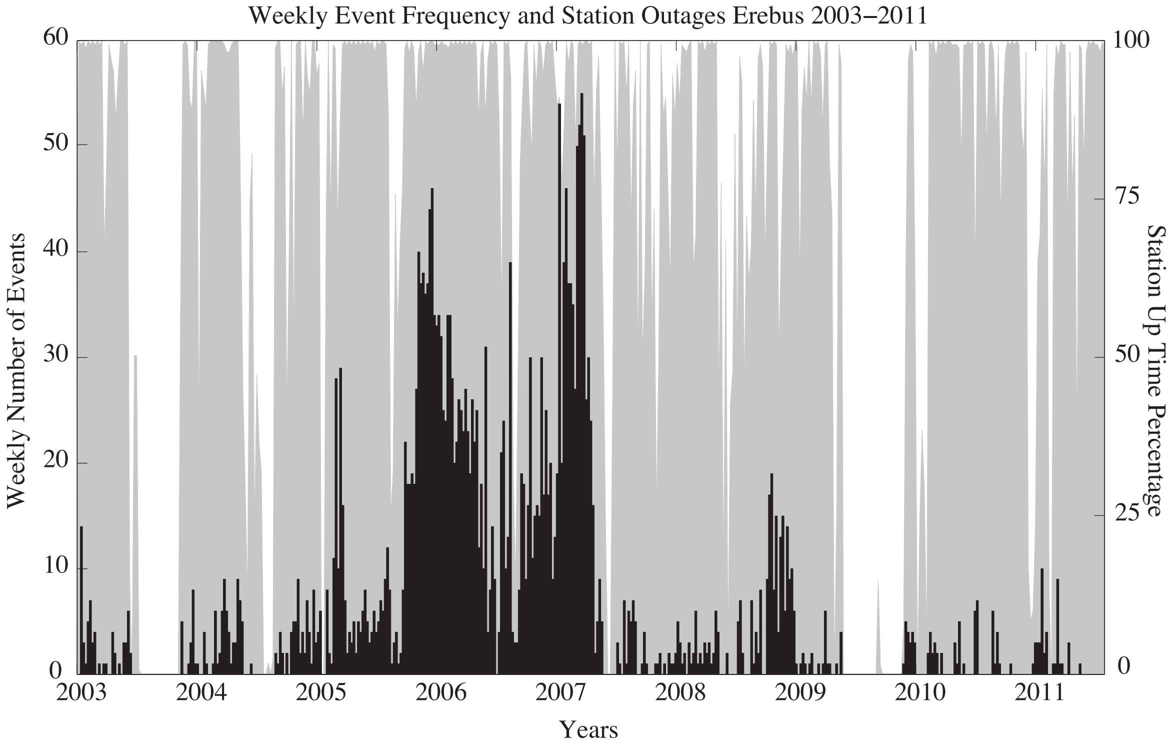

Figure 1.4: Weekly distribution of 2,974 eruptions detected using the matched filter shown in Figure 1.3. Gray shaded time intervals indicate periods when 3 or more broadband stations were contemporaneously operational, with uptime percentage on a weekly basis noted on scale at left. Network gaps generally correspond with austral winter periods when power resources were insufficient to maintain operation.

1.4 Event Selection, Similarity, and Pre-Eruptive VLP Variability

1.4.1 Event Selection

Because they occupy distinct period ranges, SP and VLP signals are easily isolated by bandpass filtering. The seismograms were first filtered between 1-8 Hz for the SP and 0.03-0.2 Hz for the VLP bands. We then further improve VLP signal-to-noise by integrating the VLP signal from native velocity to displacement at periods shorter than the seismometer corner period (30 s) [*Aster et al.*, 2003]. This is simply achieved by high pass filtering the already bandpass filtered VLP, keeping only frequencies between 0.33 and 0.2 Hz, and then integrating the signal.

After the appropriate filters were applied, each event was cut into 1-minute segments from 5 s before the SP eruption to 55 s after the eruption, where eruption times were determined by the lag of the maximum matched filter correlation. The events were then culled to remove events that were corrupted by transients, high noise levels, or superimposed signals. This was accomplished by: 1) stacking all of the events bandpass filtered in the SP band, 2) cross-correlating each event with the stack, 3) removing events with a correlation coefficient lower than 0.4, and 4) removing any event that differed from the stack at any sample by more than three times the standard deviation of the entire population. The stack for each station's subset of aligned events is shown in Figure 1.5, along with the Power Spectral Density (PSD) of the E1S stack. The number of events comprising each stack is shown in the individual plots (designated by n) and the three dominant VLP periods are noted on the PSD.

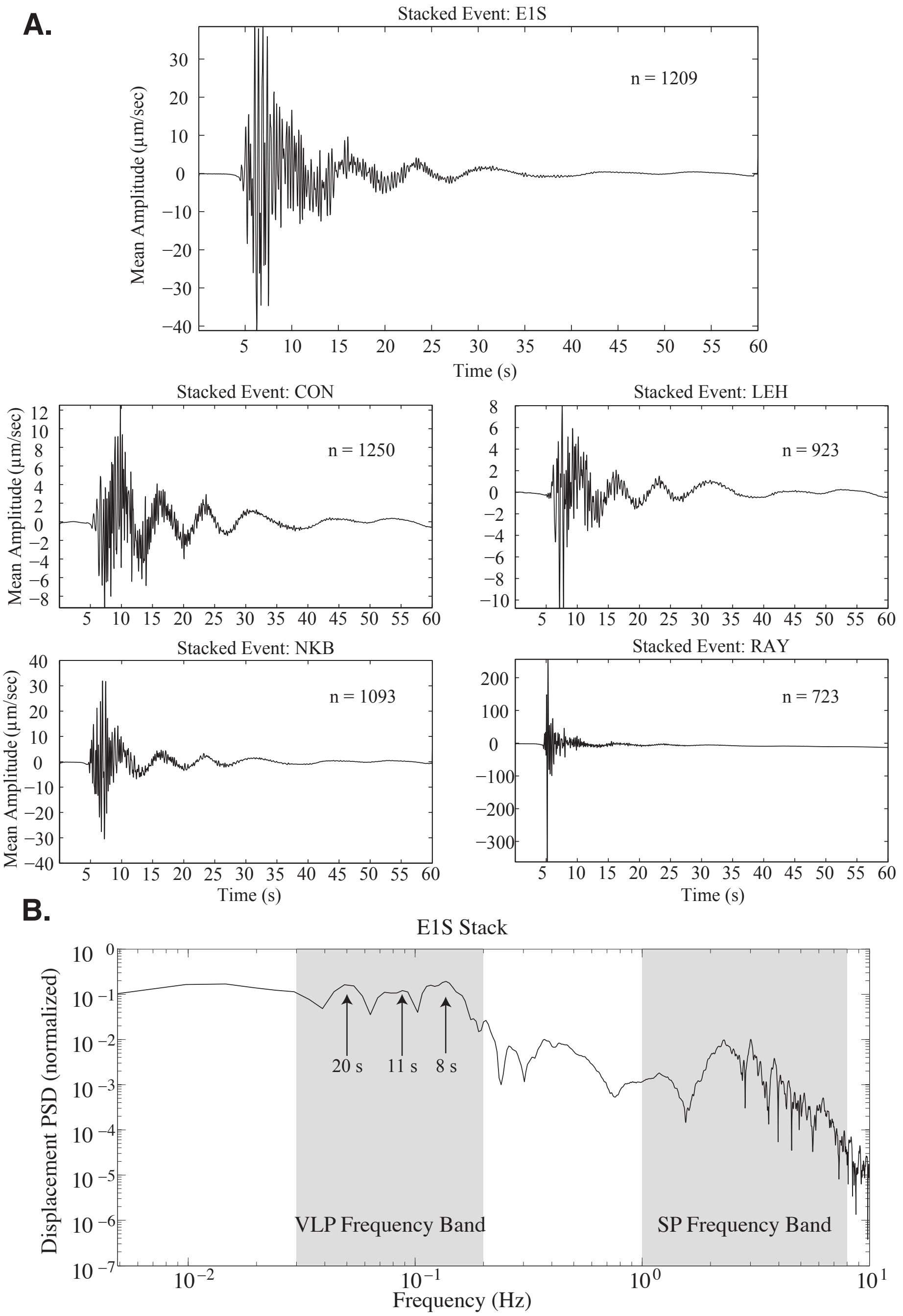

Figure 1.5: A) Stacked broadband vertical-component Strombolian eruption seismograms from stations E1S, CON, LEH, NKB, and RAY (Figure 1.2) scaled to show relative vertical seismic velocity amplitudes. Note that both the superimposed SP and VLP signal components are both readily apparent in the time domain. B) Stack displacement Power Spectral Densities (PSD) for station E1S, showing the distinct VLP and SP frequency bands associated with eruption signals [*Aster et al.*, 2003]. The three predominant VLP spectral modes near 8, 11, and 20 s period are indicated.

1.4.2 Event Similarity

Using the 1,209 events comprising the stack at E1S, we calculated the maximum inter-event correlation coefficients for the SP seismograms described above. The inter-event comparison shows that correlation values typically range from 0.3 to 0.7, with a median value of 0.42 (Figure 1.6). *De Lauro et al.* [2009] reported similar correlation values for a subset of eruptions recorded in 2005 and 2006. VLP filtered displacement seismograms show a much higher degree of inter-event similarity than SP signals. Maximum correlations typically range between 0.4 to nearly 1.0, with a median value of 0.75. Approximately 80% of the inter-event coefficients are greater than 0.7 (Figure 1.6). Unfortunately, the VLP signal-to-noise level is commonly low for smaller eruptions and during high noise periods, especially on the horizontal components because the VLP signal frequency band overlaps with that of the frequently strong oceanic microseism [e.g., *Aster et al.*, 2008b].

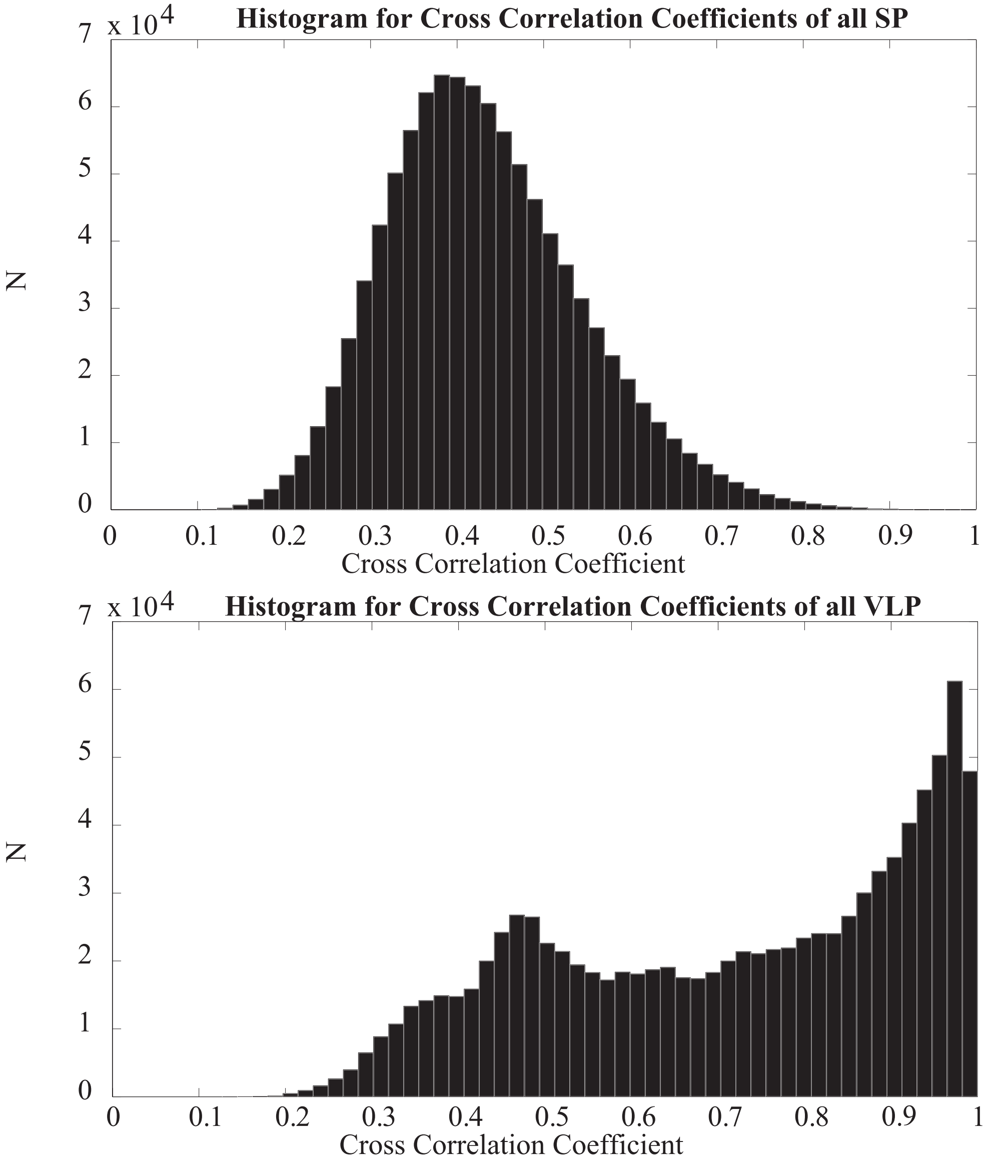

Figure 1.6: Maximum cross-correlation coefficients for 1-minute eruption seismograms in the SP (1-8 Hz) and VLP (0.02-0.3 Hz; integrated to displacement) bands. Expectations for corresponding correlation modes of band limited white noise are 0.12 and 0.7 for the SP and VLP bands, respectively. The minor secondary mode for the VLP correlations near 0.45 is a windowing artifact of the 1-minute truncated VLP seismograms used in this crosscorrelation calculations.

1.4.3 Pre-eruptive VLP Variability

The polarity and timing characteristics of the pre-eruptive VLP signal are variable *Aster et al.* [2003; 2008]. To more quantitatively evaluate this variability, we calculated the 95th, 80th, and 65th percentiles for the entire population of E1S VLP vertical-component displacement signals (Figure 1.7). Figure 1.7 shows that in each percentile calculation the initial portion (-5 to 2.5 s) and the later portion ($>$ 45 s) of the VLP are show more variability that the rest of the population. We further display this pre-eruptive VLP variability by displaying the variability in pre-eruptive vertical-component seismograms from ten eruptions in the study period (Figure 1.8). These seismograms display positive, negative, and indeterminate polarities just before the slug rupture. We also show that the amplitudes vary by a factor of $\sim$5 across the 10 events. Aa few of the pre-eruptive signals show little to no pre-eruptive displacement.

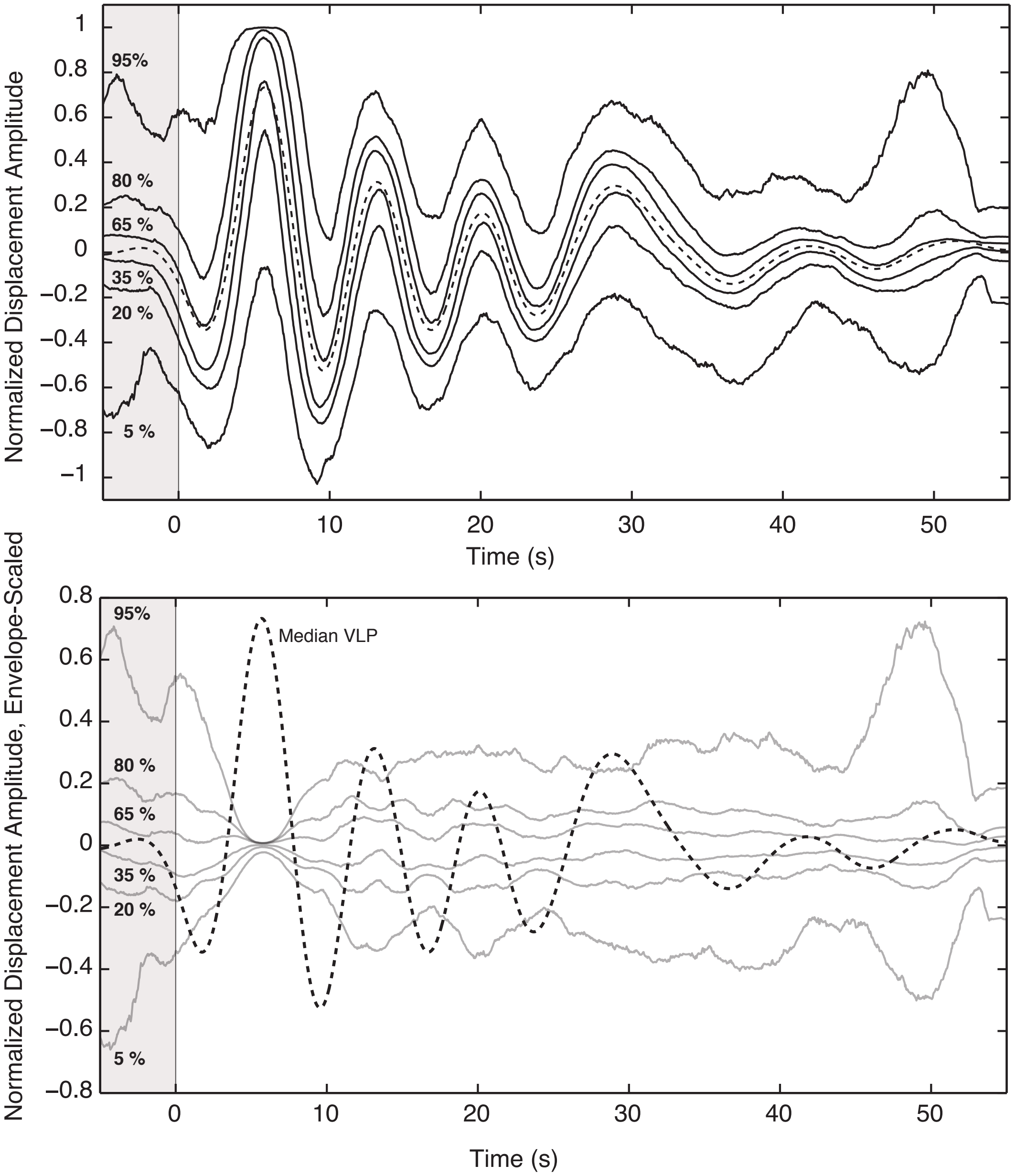

Figure 1.7: A) Median displacement VLP signal (dashed trace) calculated from the 1,209 events recorded by station E1S with sample-by-sample percentiles indicated. Zero time marks the onset of the SP signal and the slug's rupture at the lava lake surface. B) Data from (A) scaled by the Hilbert transform envelope to show seismogram variability relative to signal amplitude. Pre-eruptive VLP signal period is indicated with shading. Note the much larger variability of the pre-eruptive, relative to post-eruptive, VLP signals.

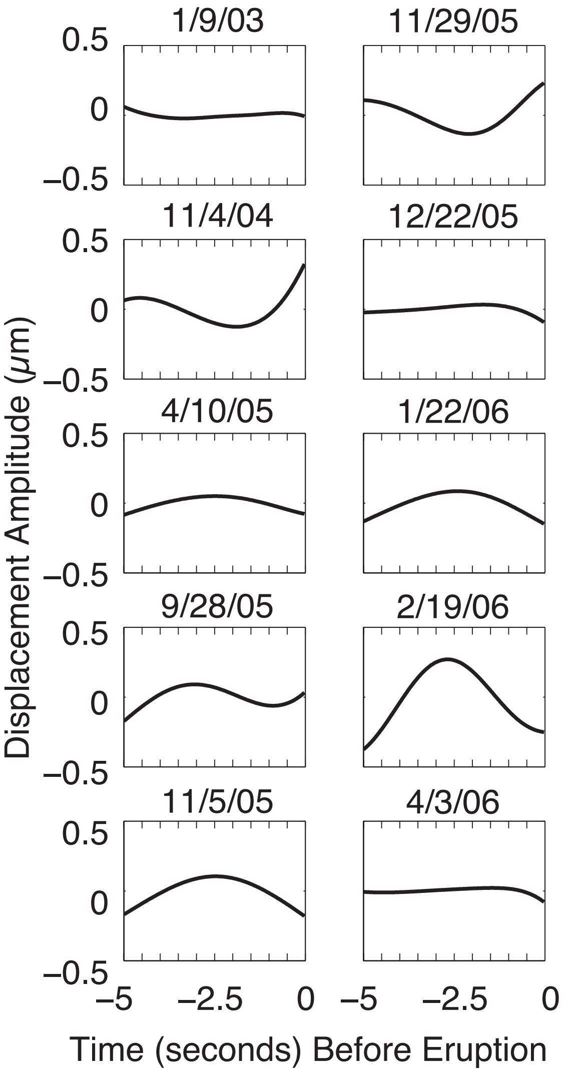

Figure 1.8: Representative pre-eruptive VLP vertical-component displacement signals from ten of the 1,209 events recorded at E1S (dates indicated) displaying pre-eruptive polarity and amplitude variability. Zero time marks the onset of the SP signal and the slug rupture at the lava lake surface.

1.5 Results

Following filtering and event selection, the relative event-to-event timing of the SP and VLP signals was estimated via crosscorrelation at 1 sample (0.025 s) time resolution. The relative correlation lags were then examined across the more than eight years of available recording for temporal variations. Aligned SP vertical-component seismograms displayed on a station by station basis are shown in Figure 1.9. To compare the relative timing of the SP and VLP signals, VLP waveforms are displayed using time alignment corresponding to peak SP signal correlation (Figure 1.10).

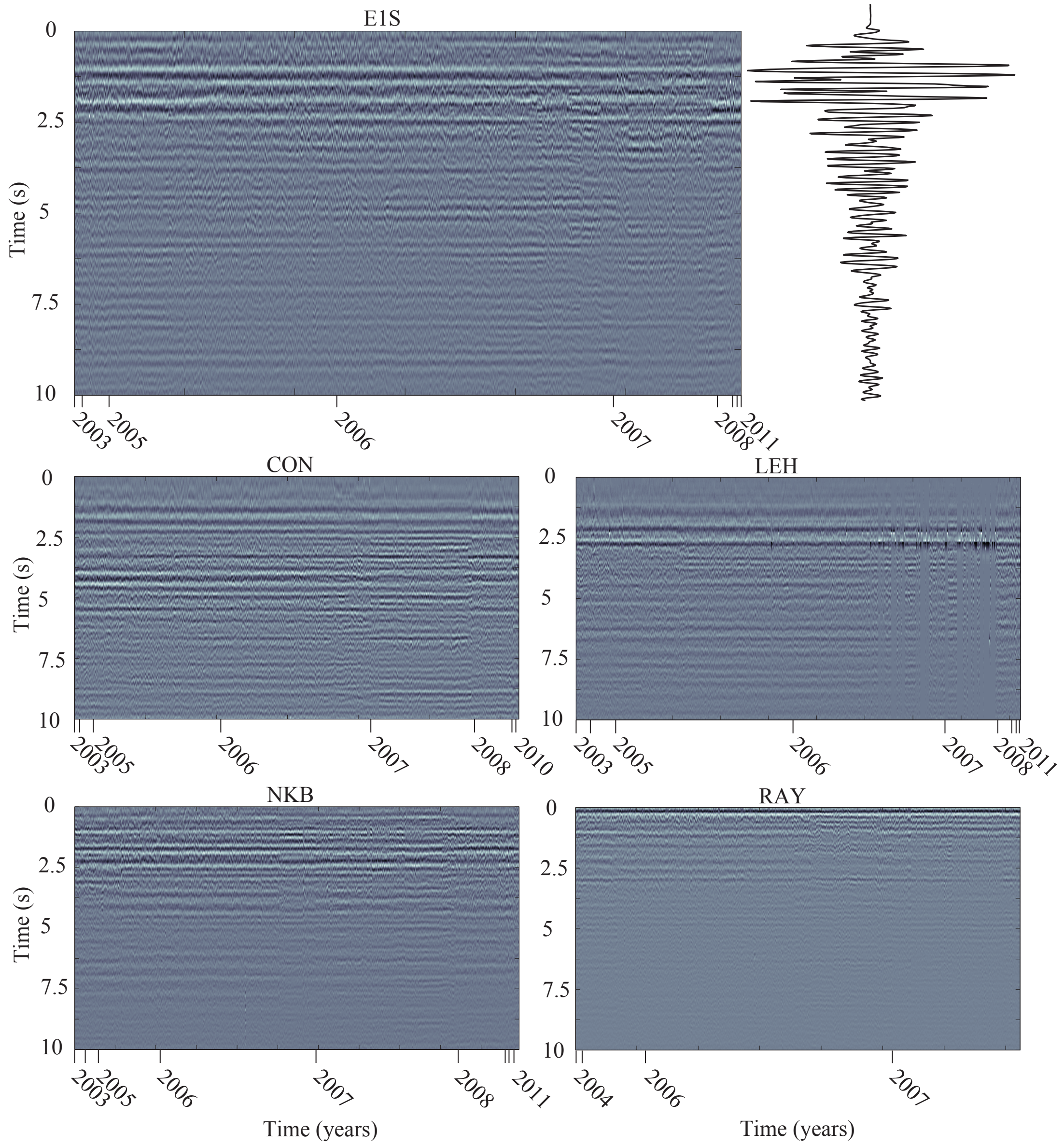

Figure 1.9: Vertical-component SP signals (1-8 Hz) aligned by full-waveform crosscorrelation at each station (Figure 1.2). The greatest number of events is drawn from the unusually active eruptive period between 2005-2007 (Figure 1.4). Seismogram time (referenced to eruption origin time) increases in the downward direction of the y-axis. Velocity seismogram at right shows the corresponding SP stack for station E1S.

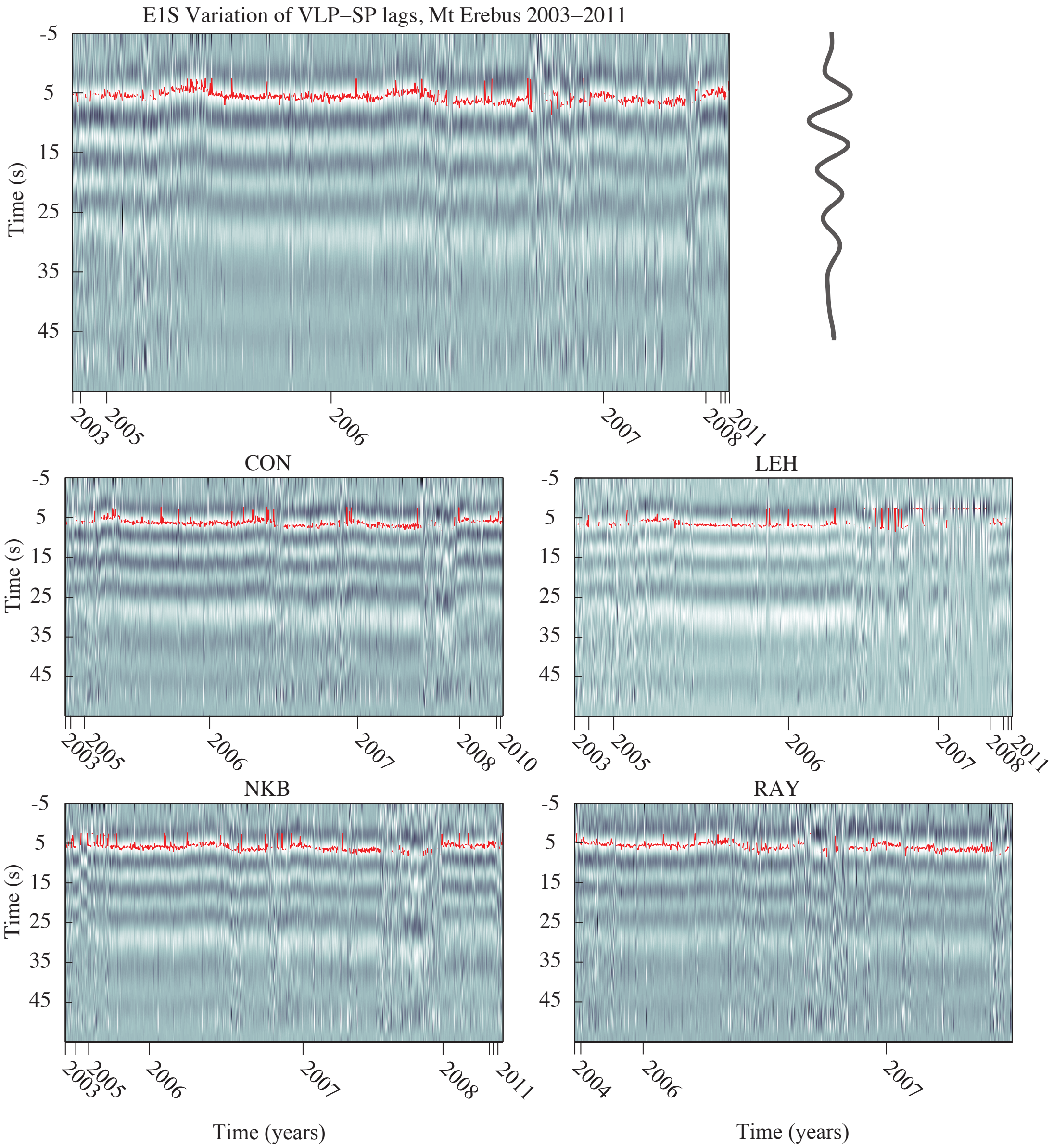

Figure 1.10: VLP signals displayed in the same fashion as in Figure 1.9 and aligned using the identical SP correlation-determined lags. The first VLP peak detection (red) and general seismograms display time-progressive shifts of up to 1 s relative to the SP correlation alignment. Breaks in the red curve correspond to intervals where VLP signal-to-noise levels were insufficient to follow the trend due to background noise levels. Displacement seismogram at right shows the corresponding VLP-filtered correlation-aligned stack for station E1S.

We observed systematic shifts of the VLP signals relative to the SP alignment of approximately ±1 s from their mean values occurring over days to months (Figure 1.10) within the more than eight-year data set (Figure 1.4). These time shift fluctuations are observed over multiple time periods (Figure 1.11) and are best resolved in calendar time during times of greater eruption activity, when they are more densely sampled. We note a smooth multi-month VLP-SP delay decrease and subsequent increase with approximately ±1 s of lag variation during late 2005 and early 2006, and another comparable variation between November 2006 and March 2007. Less well-resolved decreasing trends in the relative time delay of approximately ±1 s are also suggested between late 2007 and mid-2008, and between late 2008 and early 2009. Figure 1.12 displays the nature of the relative lag changes during late 2005 and early 2006 by showing five example eruption seismograms recorded during an approximately 7-month period at a representative station (E1S).

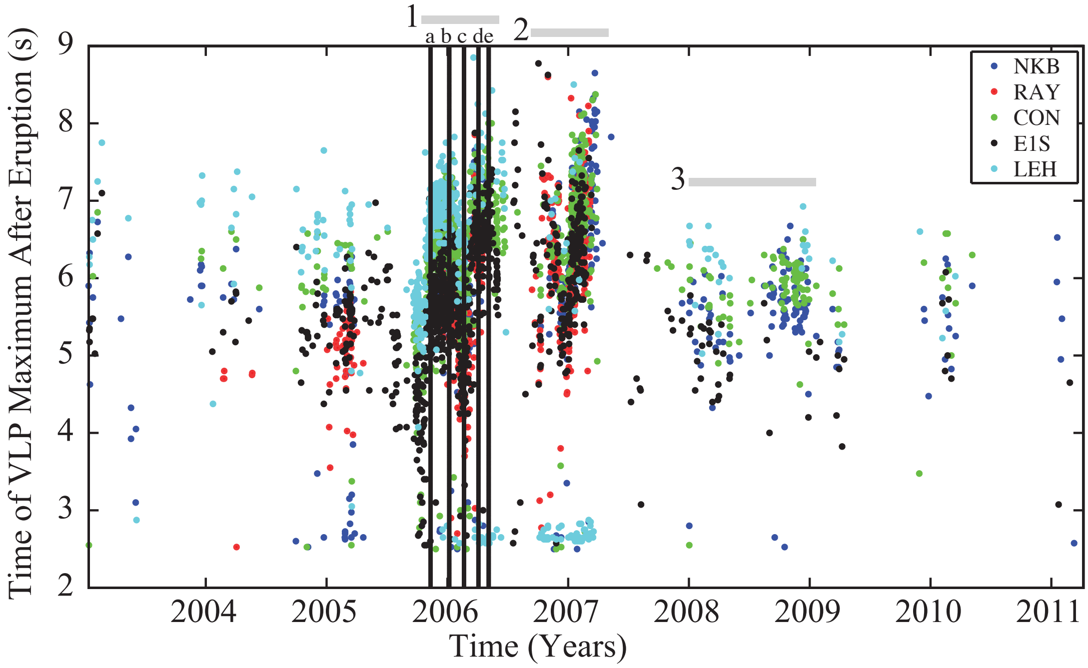

Figure 1.11: Temporal variations of the VLP-SP delay (Figure 1.10) for seismic stations (Figure 1.2; Figure 1.10) as indicated by color legend. Variations during 2006-2007 are well sampled due to an especially high rate of lava lake eruptions during that period (Figure 1.4). Note the consistent station-to-station tracking of trends, with some propagation delay (RAY is the closest and LEH is the furthest station from the lava lake). The three primary time periods of variation are indicated with gray bars: 1) A decrease and subsequent increase between late 2005 and early 2006; 2) A decrease and subsequent increase in late 2006 and early 2007; 3) Two episodes of less well-resolved decreases between late 2007 and early 2009. Vertical lines correspond to the times of representative seismograms shown in Figure 1.12.

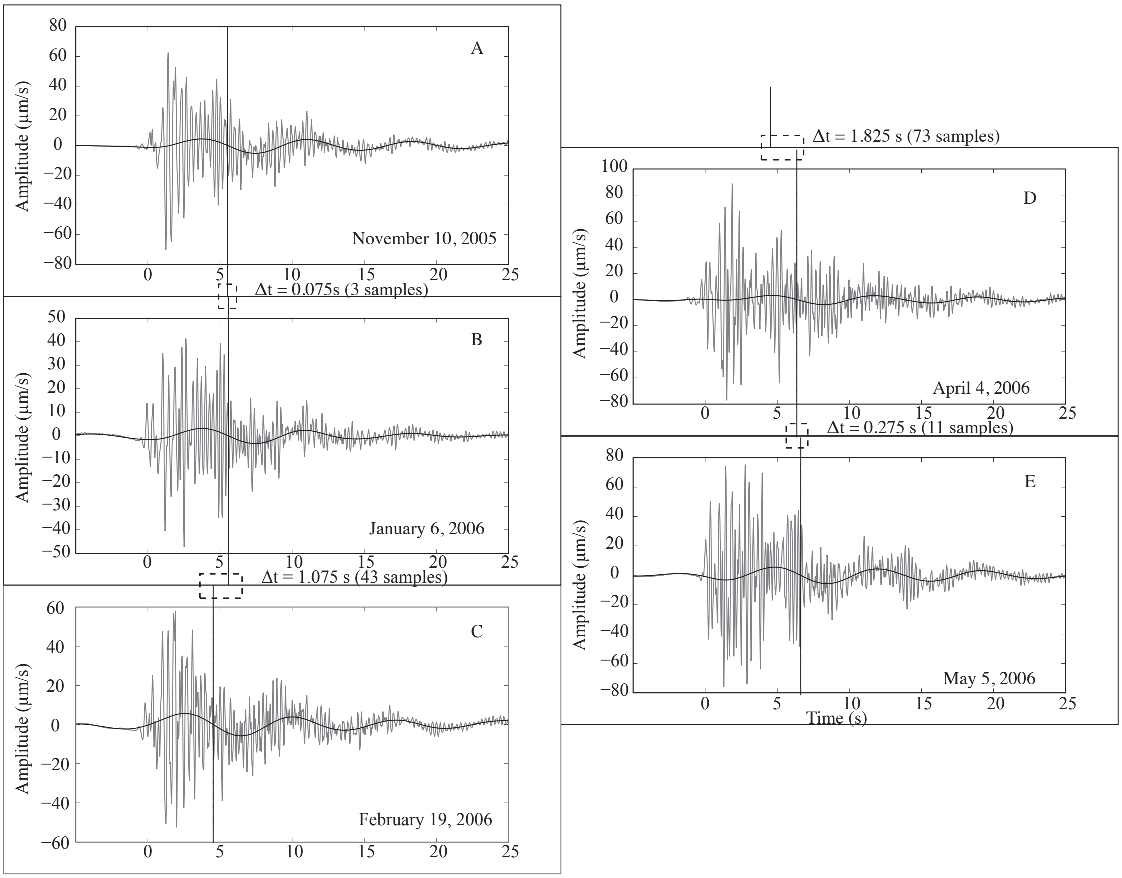

Figure 1.12: Representative vertical-component SP and VLP seismograms recorded at station E1S (Figure 1.2) between November 2005 and May 2006 corresponding to the marked times in Figure 1.11 . The selected VLP zero crossing, indicated by a vertical line in each case, illustrates VLP-SP delay changes, and its difference in s relative to the previous seismogram is noted at the top of each panel.

1.5.1 Station-to-Station Comparison

We rule out the possibility of station-specific effects, aside from seismic propagation path lengths from source to station, influencing these observations by noting the systematically similar nature of the variations across the network (Figure 1.11). Correlation analysis of the VLP-SP delay variations is shown in Table 1.2. This processing was conducted by isolating all of the event lags recorded on two stations and then computing the correlation coefficient between the two time series. This is an important step since each station's lag variation (Figure 1.11) is represented by a non-uniformly sampled time series; the events are not evenly spaced in time and/or all events are not necessary recorded by the two stations subject to the correlation analysis.

Comparing the observed trends between stations, we see the lowest correlation in station comparisons with LEH. This is unsurprising because LEH, being the most distant station from the lava lake, has a much lower VLP signal-to-noise ratio relative to the other stations analyzed here[*Aster et al.*, 2008]. For this reason, we disregard the very noisy correlation trends at station LEH. VLP-SP trends between other station pairs show interstation correlations varying from 0.69 to 0.91..

Table 1.2: Station-to-station correlation matrix of the temporal trends shown in Figure 1.11. Number of events used for each measurement is shown parenthetically.

	E1S	NKB	RAY	LEH	CON
E1S	1				
NKB	0.703 (314)	1			
RAY	0.851(247)	0.687 (227)	1		
LEH	-0.213 (376)	-0.204 (280)	-0.496 (194)	1	
CON	0.914 (406)	0.768 (369)	0.755 (217)	-0.108 (367)	1

1.5.2 Frequency Independence of VLP-SP Timing Changes

Tracking the maximum peak in the VLP signal with respect to the SP-determined alignment, as in Figure 1.11, is an effective way of displaying the VLP-SP delay variation. A more robust method of examining this variation in detail, given the high degree of waveform similarity, is to estimate relative lags via cross-correlation. This analysis, which is performed by aligning each of the filtered VLP signals with an iteratively aligned stack, shows the same temporal variations as tracking the maximum (Figure 1.13). The correlation coefficient for the two time series is 0.56 when all data points are taken into consideration. If we constrain the correlation shifts for low signal to noise events (typically represented by lags $> \pm 3$ seconds in Figure 1.13), the correlation coefficient is improved to 0.79.

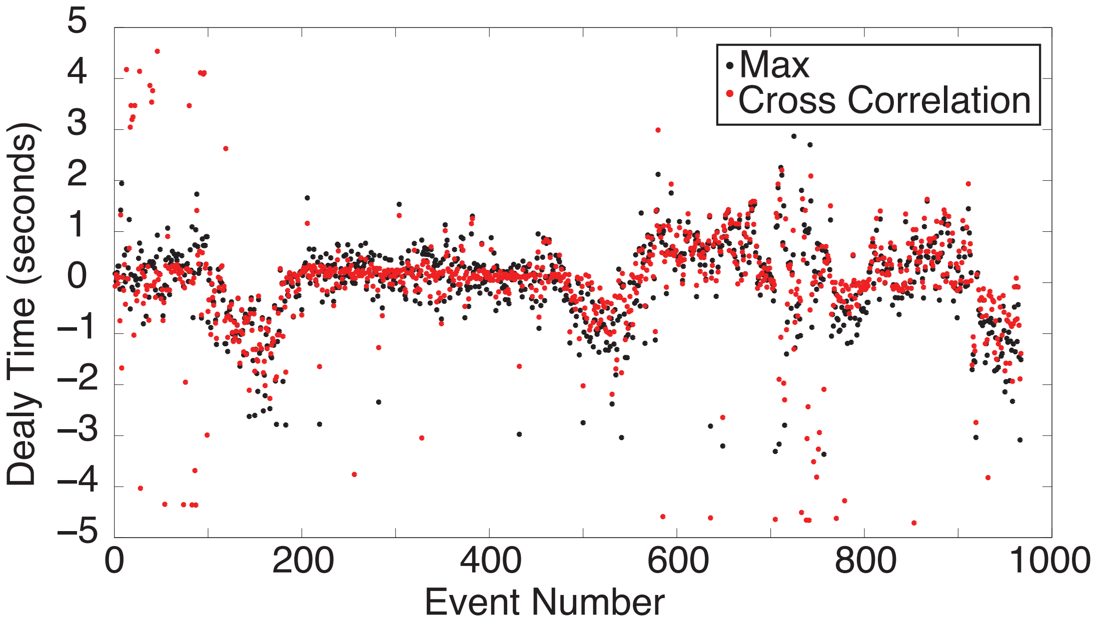

Figure 1.13: Temporal variations of the VLP-SP delay at E1S estimated via maximum tracking (Figure 1.11) and seismogram cross-correlation with an iteratively aligned stack of the post-eruptive VLP seismograms as described in the text.

Next, we analyzed the VLP-SP lags for frequency dependence, such as would arise from different delays for different VLP spectral modal components. This was performed by first filtering the post-eruptive VLP for its three primary spectral modes (spectral peaks near 21, 11, and 8 s; Figure 1.5), as well as across the entire VLP band (Figure 1.14). This analysis shows that the VLP-SP delay variation is a shift in the entire signal rather than a band-limited or frequency-dependent phase shift. We also examined the evolution of modal peaks to see if there were period shifts that correlate with the VLP-SP delay changes. Figure 1.15, shows normalized spectra VLP signals at the E1S station. Although some significant changes are seen in the width and relative amplitudes of the spectral peaks (driven primarily by variable signal-to-noise), the overall modal peak trend is stable in frequency. These observations indicate that the predominant nature of the observed temporal change is a broadband delay change between the SP and VLP source processes, rather than a change in the VLP source itself.

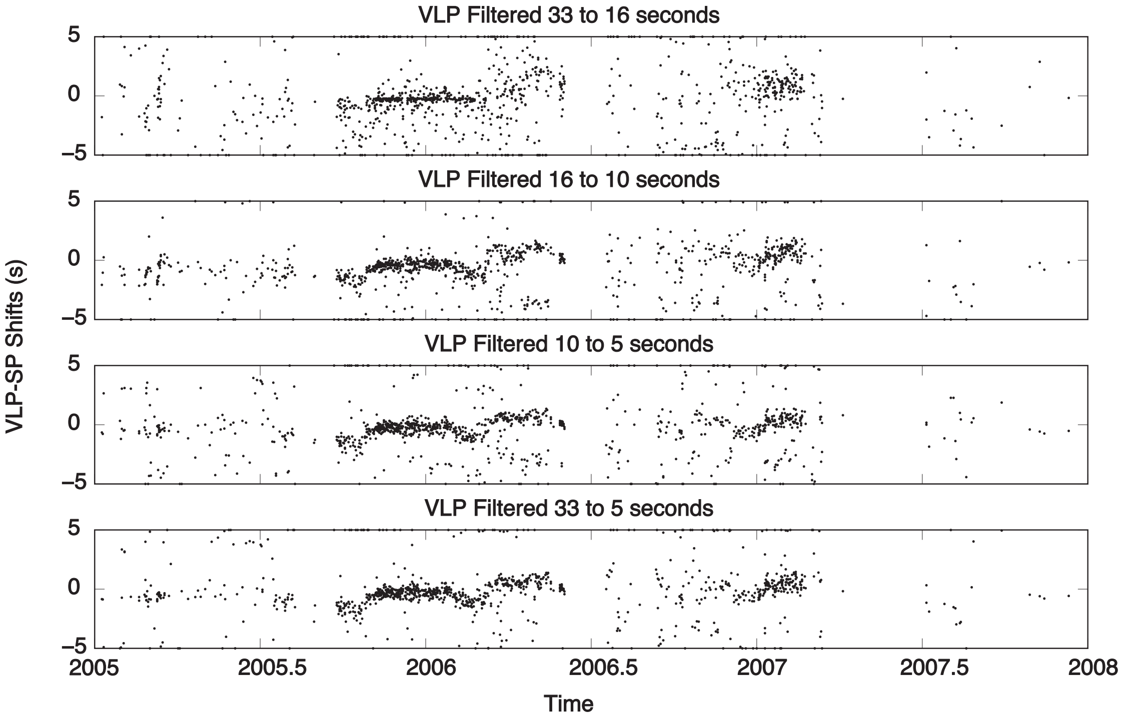

Figure 1.14: Temporal variations of the VLP-SP delay at E1S obtained via seismogram cross-correlation of the post-eruptive VLP seismograms. The time shift variations are apparent and similar in each of the three primary periods of the VLP (20.7, 11.3 and 7.8 s; Figure 1.5), although low signal-to-noise reduces detection ability for the gravest period band, indicating that VLP signal time shifts are not frequency dependent.

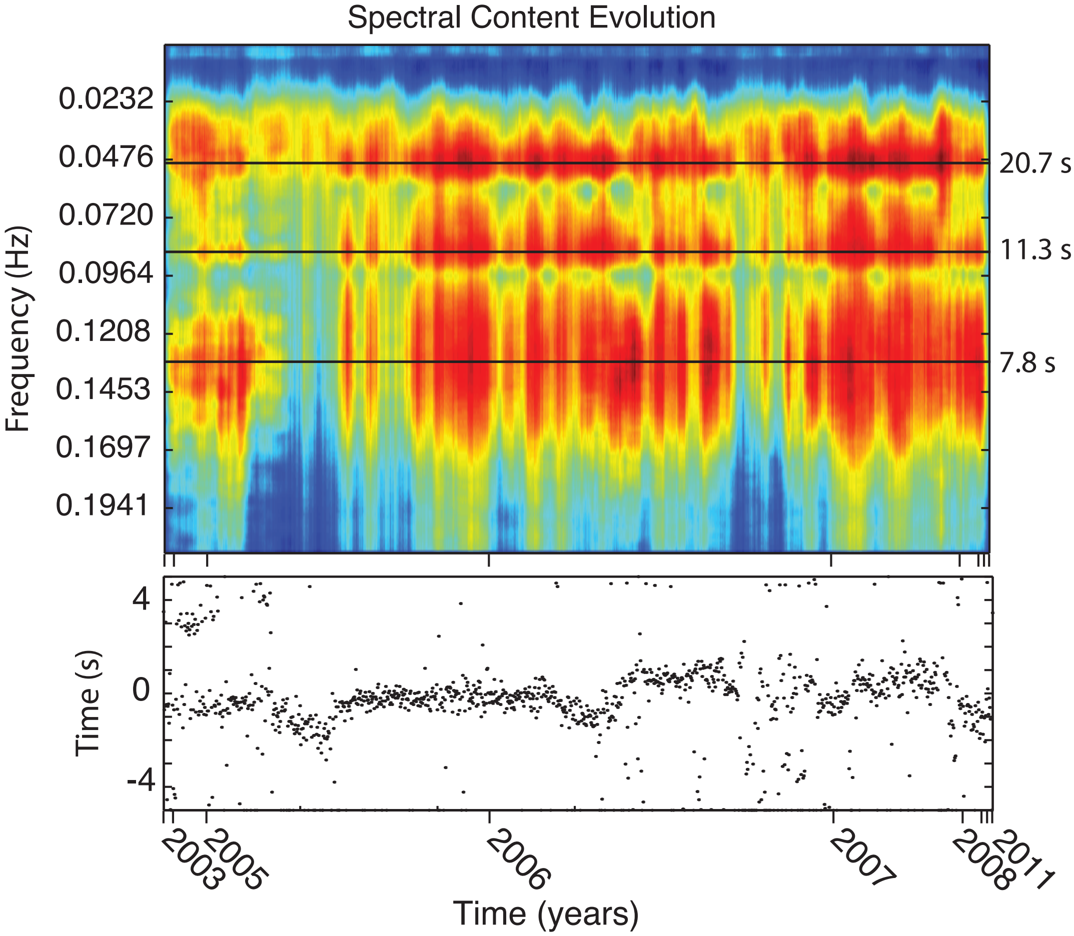

Figure 1.15: VLP spectral power for events recorded at E1S (top) and full-bandwidth VLP-SP delays estimated via cross-correlation (bottom). This figure demonstrates the stability of modal VLP periods (Figure 1.5). Eruptions where VLP spectral peaks are less visible correspond to low signal-to-noise events.

1.5.3 Stability of VLP Decay

The modal excitation of the VLP with periods near 8, 11, and 21 s can be modeled as three damped low-Q oscillators with Q values of approximately 4, 18, and 11, respectively [*Aster et al.*, 2003]. To investigate if these decay rates exhibit change across the study period, we examined VLP signal envelopes. This was assessed by computing the absolute value of the normalized Hilbert envelope (the amplitude of the analytic time series $A(t) = \|x(t) + \imath H(x(t)\|$, where H is the Hilbert transform), and plotting the smoothed envelopes (see Figure 1.16). The changes in timing for the first peak of these envelopes correspond, unsurprisingly, to the correlation-determined VLP-SP delay changes; however, we note no systematic changes in the decay of the VLP signal with time.

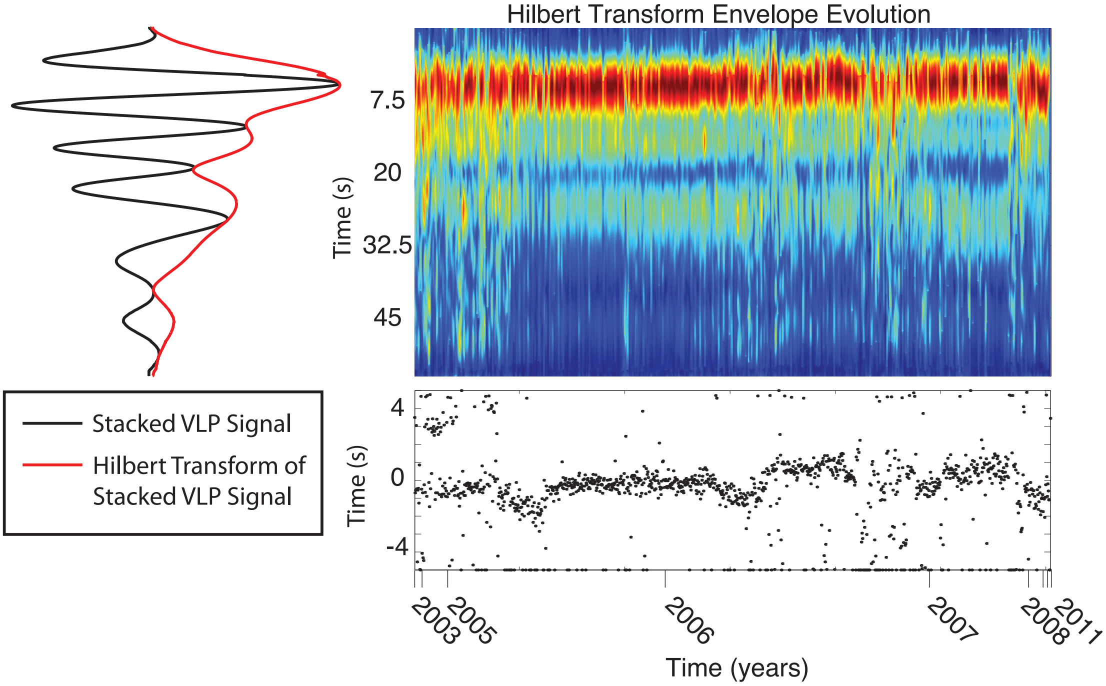

Figure 1.16: Amplitude-normalized Hilbert transform analytic envelopes, calculated as described in the text, for SP-aligned VLP seismograms (top) compared with full-bandwidth VLP-SP delays estimated via cross-correlation (bottom) at station E1S. Stability in VLP decay characteristics can be seen across the study period. A stacked VLP displacement signal is shown at left with its corresponding calculated envelope.

1.5.4 Pre- and Post-Eruptive VLP-SP Comparative Delay Changes

Final evaluation of the nature of the VLP-SP delay change was conducted by independently examining pre-eruptive signals, which correspond to the ascent of the gas slug, and calculating VLP-SP delays for these signal segments via cross correlation. We found that the pre-eruptive VLP signals showed no consistent lag relationship with the SP signal. This finding ultimately reflects the variability of this pre-eruptive signal, which was noted by *Aster et al.* [2003] and shown in Figure 1.8.

1.6 Discussion

Analyses of the VLP-SP delay and its corresponding changes show that the timing variations represent a frequency-independent delay between the SP signal and the post-eruptive VLP signal (Figure 1.14). We hypothesize that the VLP-SP delay changes may reflect a gradual (days to weeks time scale) process that alters the timing between the unloading of the conduit in the eruption and the subsequent onset of oscillatory recharge. To evaluate this hypothesis, we next consider physical processes that could explain these observed temporal variations. This analysis includes the assessment of possible instrument artifacts, variations in eruption size, evolution of eruption location in the lava lake, and a review of changes in lava lake morphology.

1.6.1 Instrumentation Temperatures

We first examined the possibility that the VLP-SP delay variations could be associated with a temperature-dependent system phase or other electromechanical response change in the Guralp 40T sensors, which employ force-feedback to achieve a low frequency response. Erebus seismometers and data logging components undergo large-scale annual and diurnal temperature fluctuations, with outside wire temperatures varying between approximately -22 and -55°C. Each broadband seismometer is deployed with an Applied Geomechanics model 701-2A tiltmeter, which has an internal temperature sensor that is continuously logged at 4 samples/s [*Aster et al.*, 2004]. The internal power dissipation of the tiltmeter is comparable to that of the broadband seismometer, so it is a useful proxy for measuring vault temperature. These vault temperatures are approximately 12°C higher than the outside air temperature. Figure 1.17 demonstrates that VLP-SP lag variations are not significantly correlated with the instrumentation temperature or seasonal trends.

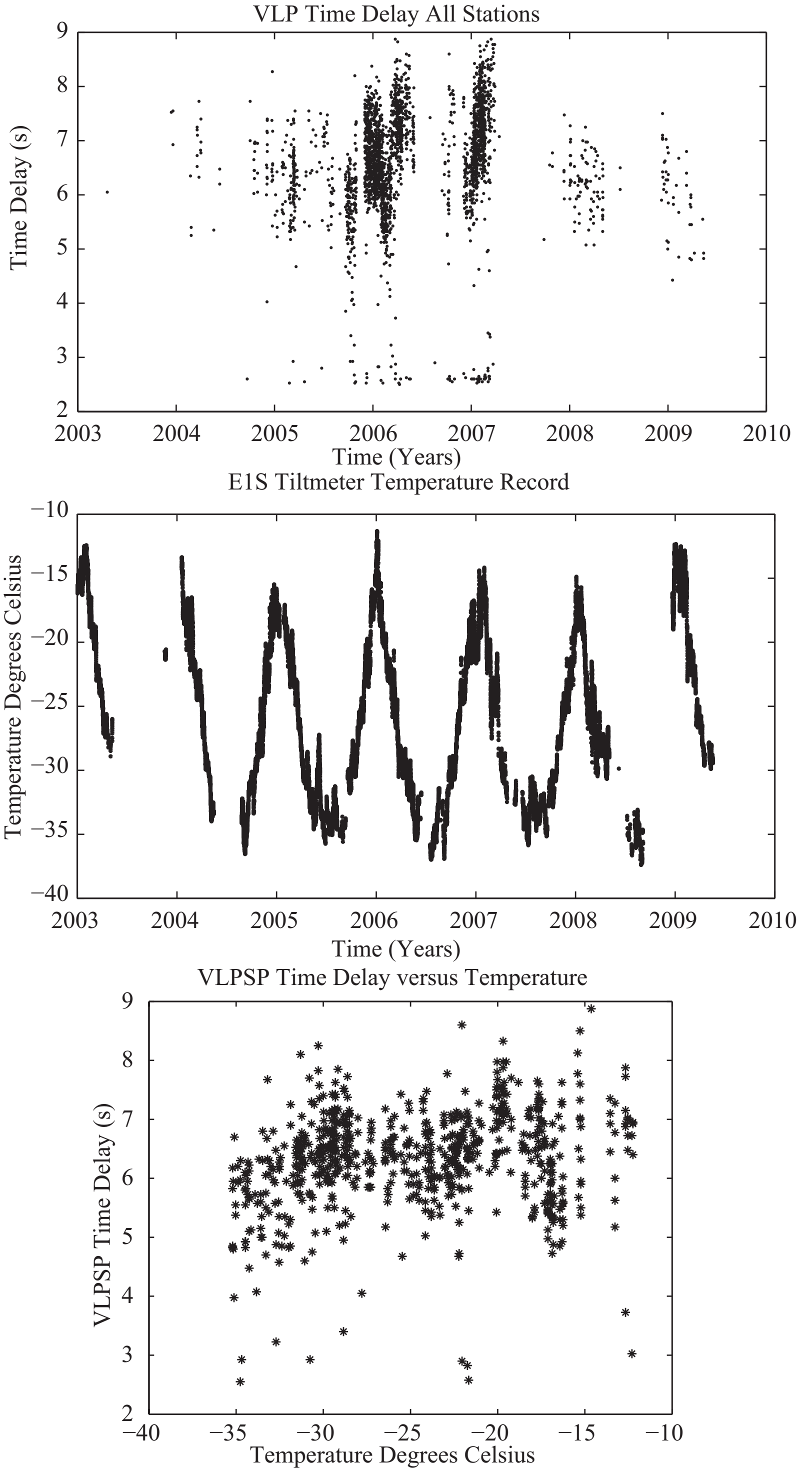

Figure 1.17: VLP-SP delay and instrumentation temperature variations across the study period at representative station E1S. The top plot shows the E1S temporal trends (Figure 1.11), the central plot shows seismometer temperatures estimated from the co-sited tiltmeter temperature sensor, and the lower plot shows VLP-SP lag versus temperature.

1.6.2 Eruption Sizes

We next examine the possibility that the VLP-SP delay variations are linked to systematically varying eruption sizes, since eruption size is related to slug size and to the amount of material removed from the lava lake during an explosion. Eruption sizes in our catalog, quantified via either maximum or root-mean-square [RMS] seismic or infrasonic amplitude, vary by approximately two orders of magnitude (Figure 1.18). This is consistent with the size range noted in previous compilations [*Rowe et al.*, 2000; *Aster et al.*, 2003; *Johnson and Aster*, 2005].

SP and infrasonic amplitudes show a strong linear correlation, that breaks down for very small events [*Rowe et al.*, 2000]. The general correlation between SP and infrasound amplitude is unsurprising, given that they are both principally excited by the high acceleration initiation of the Strombolian bubble burst [*Gerst*, 2010]. *Aster et al.* [2003] also noted a strong proportionality between VLP amplitudes and infrasonic/SP event size, which is also seen here (Figure 1.18). We propose that this trend arises because the VLP amplitude is controlled by the amount of mass removed from the conduit system tip in eruptions, which is in turn roughly proportional to the SP/infrasound explosion size.

We compared VLP-SP delay times to the event size metrics of Figure 1.18 and found no significant relationship between the VLP-SP delay and event size trends, which are essentially uncorrelated from event to event (Figure 1.19; correlation between delays and sizes is 0.24). It is intriguing, however, that the times of clearest VLP-SP variation (shown with grey background in Figure 1.19) exhibit a greater range of event sizes than the surrounding years. To characterize this phenomenon, we construct moving window Q-Q (quantile-quantile) plots (e.g., *Aster*

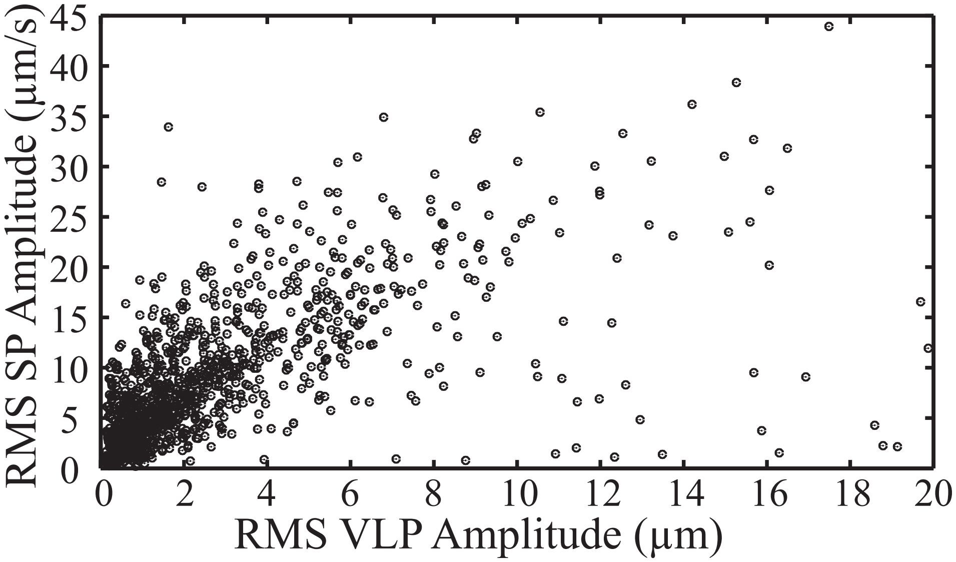

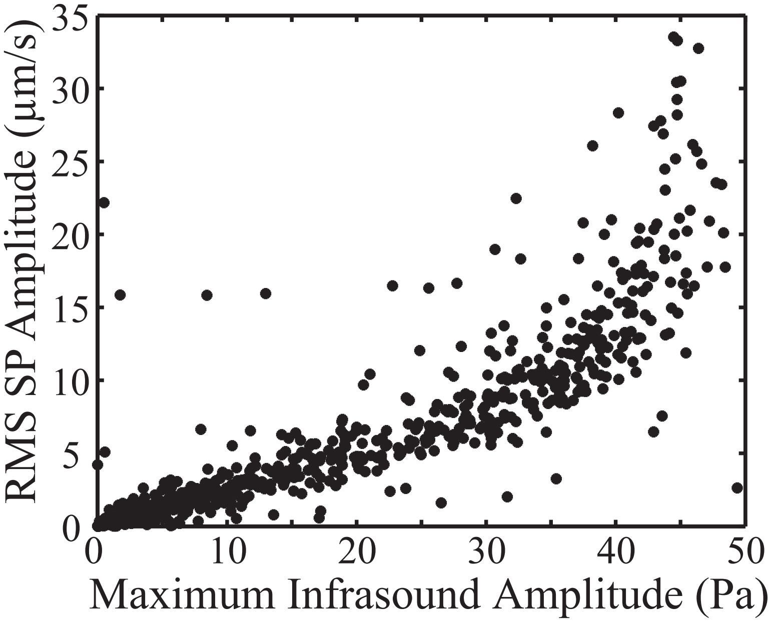

Figure 1.18: Top: RMS seismic amplitudes of SP vs. VLP signals (1209 events from station E1S). The SP size is calculated from velocity seismograms filtered between 1 and 8 Hz, while the VLP size is calculated from displacement seismograms filtered between 0.03 and 0.2 Hz. Bottom: RMS SP seismic amplitude vs. infrasound peak pressure (783 events from station E1S; infrasound data is not available for every event in the top figure). Nonlinearity above ∼40 Pa is due to infrasound sensor clipping for the largest events.

et al., 2012) and compare sample distributions. In these Q-Q plot analyses, the emperical cumulative distribution functions for two populations (i.e. eruption sizes) are aranged in to regular intervals (quantiles), and plotted against each other. If the populations are drawn from proportional distributions, the Q-Q points will lie on a straight line.

We binned the 582 events recorded at E1S that occurred between October 23, 2005 and May 30, 2006 into three illustrative separate populations and examined Q-Q plots between all combinations of these bins (Figure 1.20). Because bin C in Figure 1.20 had slightly fewer events than A or B, a random subset of A and B was used. Two of the Q-Q plots show a systematic deviation from a linear trend, indicating that the event size distributions varied in the distribution tail (with increased preponderance of larger events) during the time period between December 16, 2005 and February 23, 2006 (Figure 1.20: Comparisons A-B and B-C). This time period was chosen for analysis because it spans the VLP-SP change described by phase 1 in Figure 1.11.

Investigation of relative size statistics through time (via Q-Q comparison) continued by comparing eruption sizes associated with relatively short VLP-SP time delays ($\leq$ 5.7 s after the eruption as determined by the onset of the SP) to those with relative long VLP-SP time delays ($>$ 5.7 s; Figure 1.21). Because there were fewer event size determinations for the relatively long time delays, a subset of event sizes for the shorter time delays was used. The cutoff between the two was chosen because it represents the mean value. This analysis showed that the distributions were fairly similar.

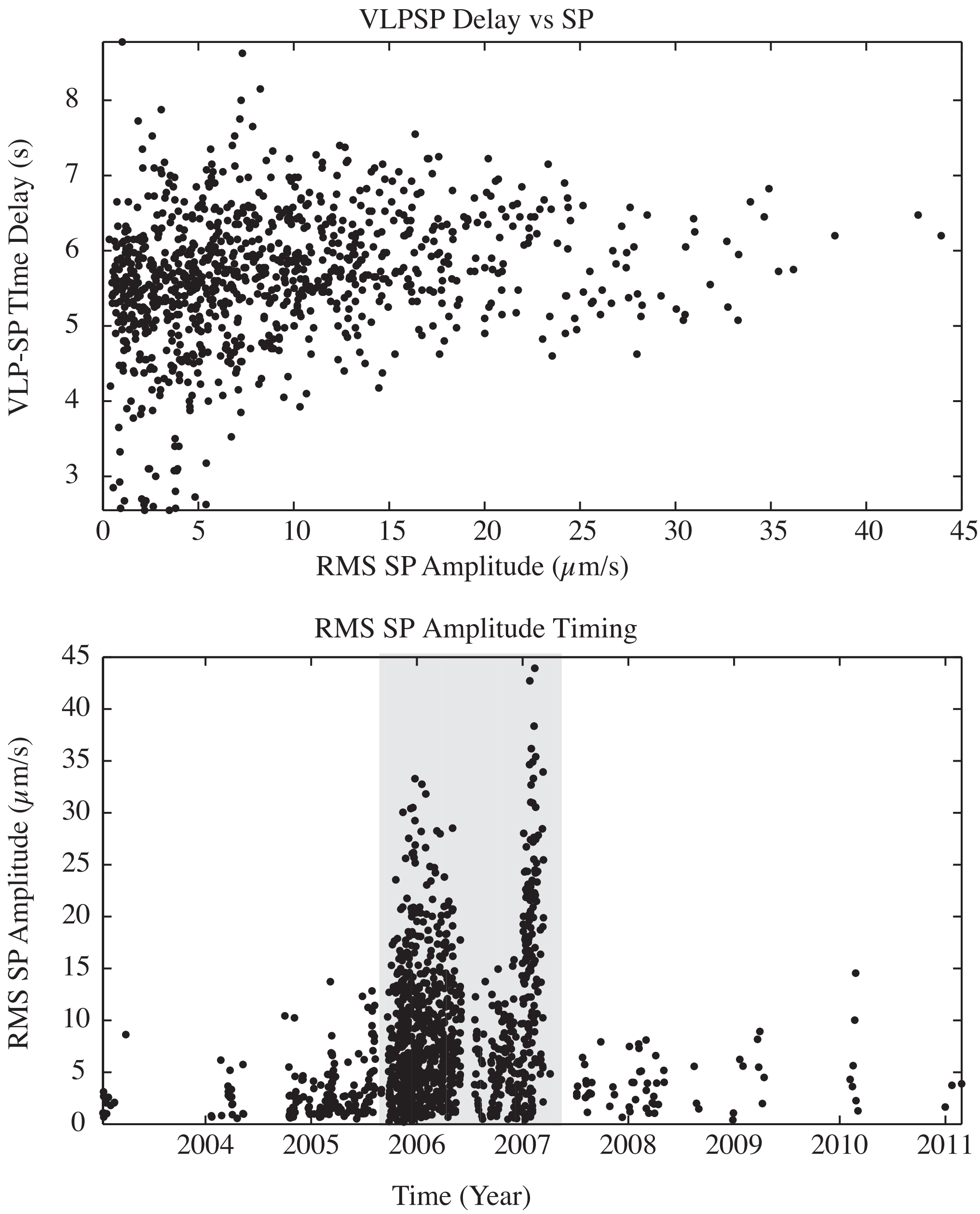

Figure 1.19: Top: VLP-SP time delay versus SP event size (Figure 1.18). Bottom: RMS SP amplitude as a function of time.

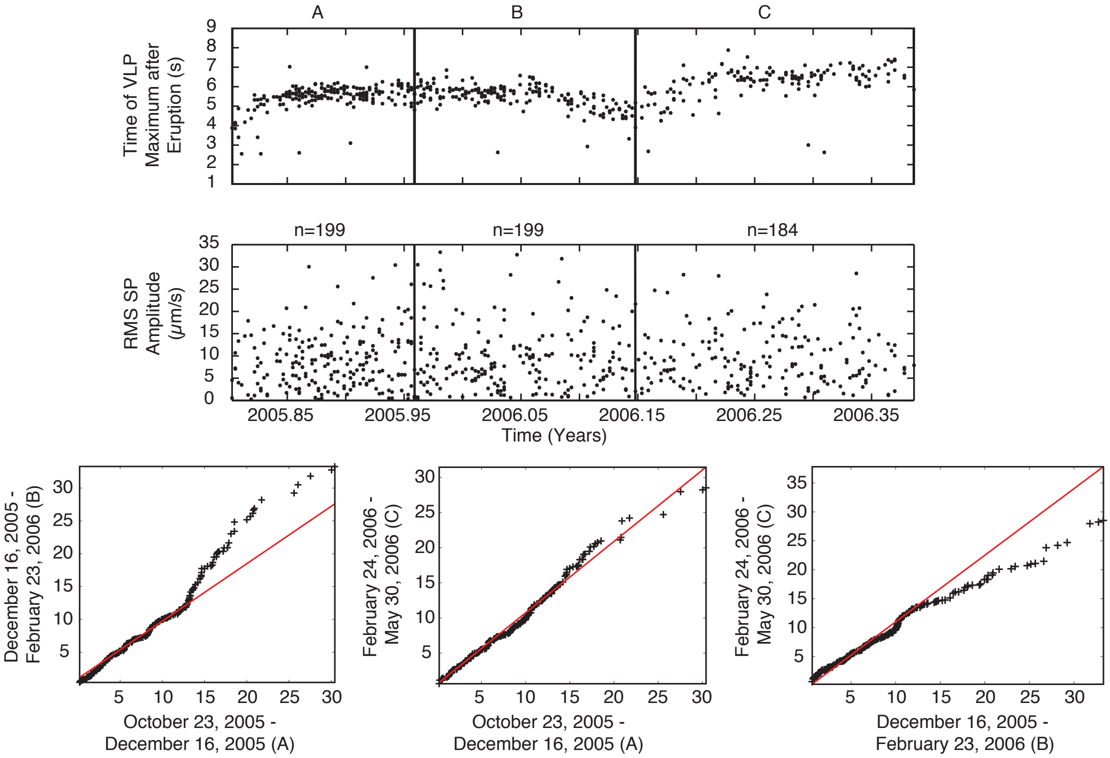

Figure 1.20: (Top) VLP-SP time delays from Figure 1.11. Note the individual bins and the number of events included in each one. (Middle) Event Sizes shown in Figure 1.19. (Bottom) Q-Q plots for temporally binned subsets of 582 eruption size estimates measured at E1S between October 23, 2005 and May 30, 2006. The events were binned so that eruption sizes could be compared between a relatively stable VLP-SP delay time period (A) and a time period when the VLP-SP delays are decreasing (B) and increasing (C). The comparison between A and B shows that the B distribution is comparatively long-tailed (i.e., indicationg an increased proportional frequency of relatively larger events). Between A and C, we see that the event sizes are from roughly the same distribution. Comparison between B and C shows, that again the B distribution is comparatively long-tailed.

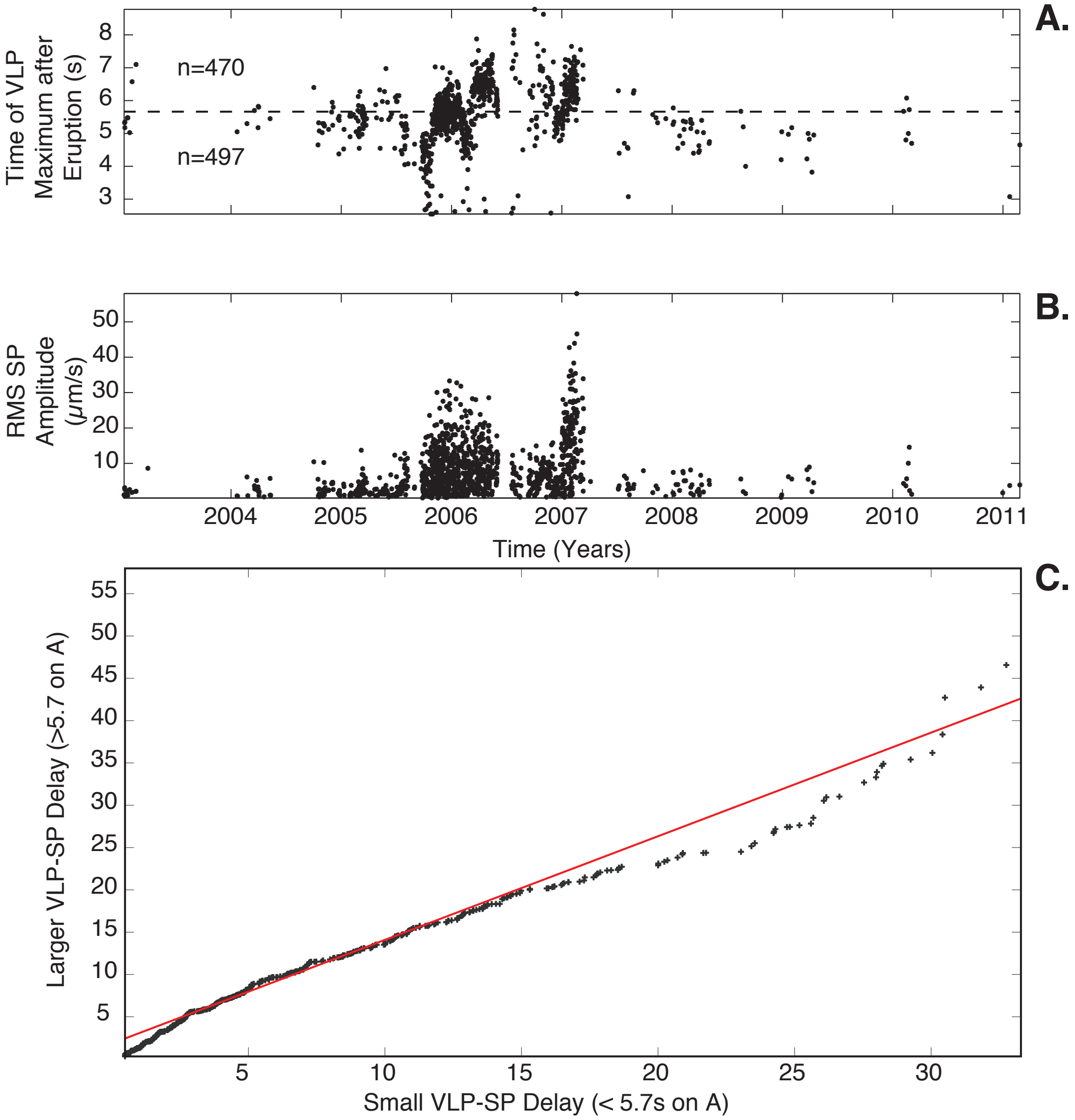

Figure 1.21: A) VLP-SP time delays from Figure 1.11. Note the two bins and the number of events included in each one. B)Event Sizes shown in Figure 1.19. C) Q-Q plot for event sizes binned based on their relative VLP-SP time delays (≤ 5.7 and >5.7 s after the eruption). The distributions are generally similar.

1.6.3 Eruption Locations

We examine whether changes in VLP-SP delay might be associated with the location of slug emergence in the lava lake and/or in the location of the first slug rupture that initiates the SP signal [*Rowe et al.*, 2000; *Gerst*, 2010]. The potential variation in location is tightly constrained by the dimensions of the ($\sim$50 m diameter) lava lake. It is possible, however, that if the eruption burst locations show similar systematic variations, then both measurements could reflect a common underlying process (i.e. changing shallow conduit geometry that effects slug delivery to the surface). We evaluated this possibility using a subset of eruptions between January 2, 2005 and April 8, 2009 that were well-recorded on crater rim-sited infrasound sensors, and thus have well-located acoustic hypocenters [*Jones et al.*, 2008].

To locate SP infrasonic sources, we employed the methodology of *Johnson et al.* [2010] and *Johnson and Jones* [2010] that uses semblance and a grid search to find the infrasound source location. We applied a 100 by 100 m grid with 5 m resolution covering the lava lake and located all eruptions that were recorded on three infrasound sensors (Figure 1.2). Although some weak trends were noted in the locations, this procedure did not yield any obvious systematic changes in location or temporal association with the pattern of VLP-SP delays (Figure 1.22). When the VLP-SP delay trends were compared to location trends relative to the center of the lava lake (laterally and longitudinally) the measured correlation coefficients were poor (0.14 and 0.31 respectively). The deviations were measured from the center, since this is believed to be a good proxy for the deepest part of the funnel-shaped lava lake bottom and therefore perhaphs the most likely point of rupture. A possibly similar trend in longitudinal variation and VLP-SP delay times during early 2006 was further investigated, but no strong correlation was found (correlation coefficient < 0.1).

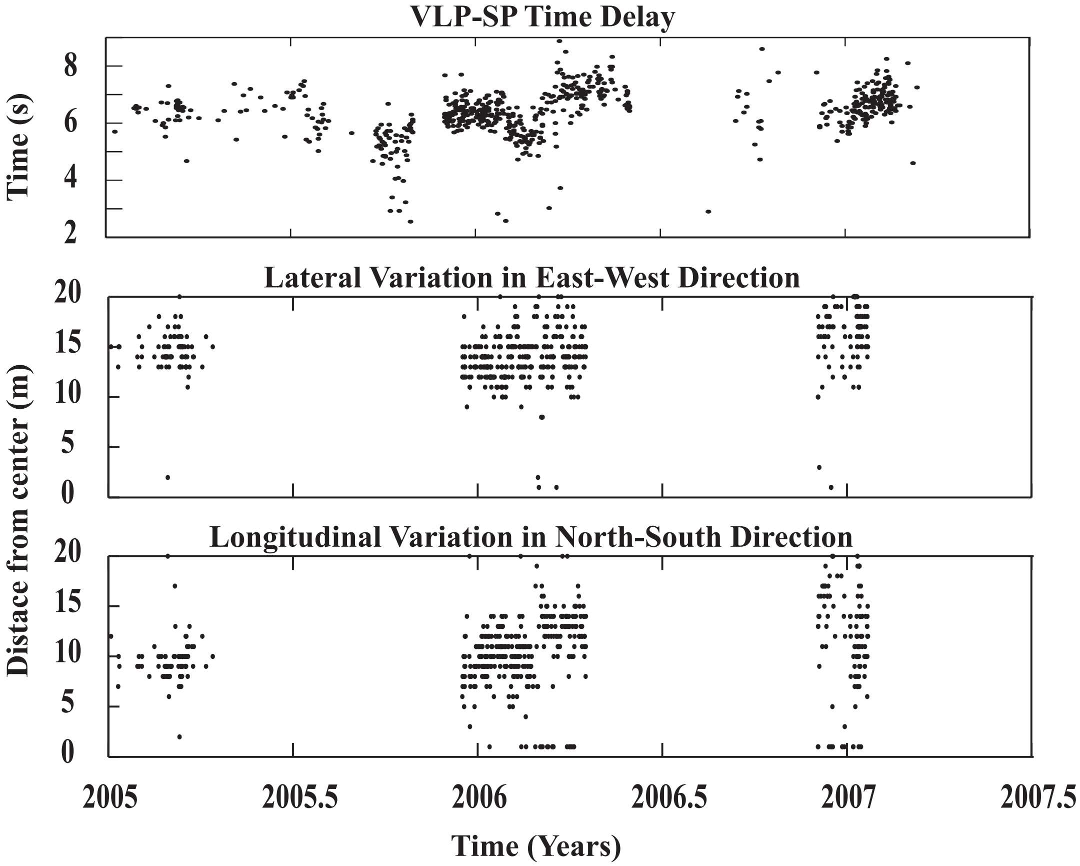

Figure 1.22: Top: VLP-SP delay as a function of time at representative station E1S. Bottom two plots: Infrasonically determined locations of the SP source on the surface of the lava lake. Note that all values represent the absolute value of the location as referenced to the center of the lava lake.

1.6.4 Lava Lake Morphology and Possible Conduit Changes due to Progressive Deflation/Inner Crater Collapse

We evaluated the available video and still observations (Figure 1.2) of the lava lake seeking evidence of VLP-SP delay correlated lava lake elevation, location, and/or size changes. Only sporadic video data and/or LIDAR measurements are available for periods of interest (i.e. late 2005 into early 2006) due to difficulties in making these measurements over long durations from the crater rim, including obstruction of the lava lake due to a condensation-shrouded inner crater. A potentially illustrative period with observations spans the end of 2005 through the end of 2006. The largest observed VLP-SP change occurs during the time period between the two series of images (top and bottom, Figure 1.23). Unfortunately, the un-cropped images reveal time-varying camera parameters during this time period, which obviated any detailed image analysis.

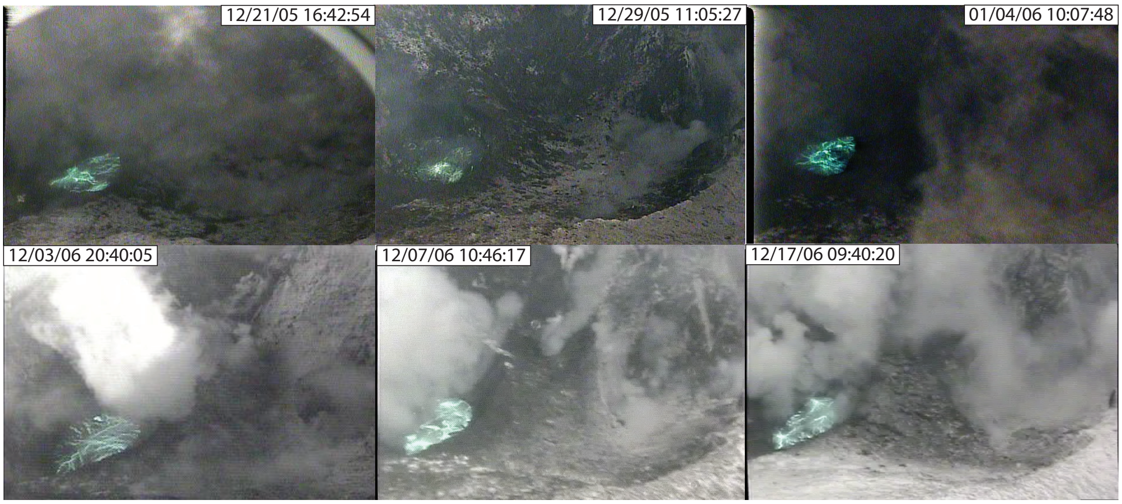

Figure 1.23: Representative lava lake images (false IR color) recorded at the VID site (Figure 1.2), showing general stability of the lava lake surface for two field seasons (also compare to pre-eruptive image of the lava lake from 2001 in Figure 1.1). Dates and times of each image are indicated the upper right-hand corner (top) and upper left-hand corner (bottom).

Airborne or terrestrial LIDAR surveys were performed on the Erebus crater during the field seasons of 2001, 2008, 2009, and 2010 [*L. Jones, oral commun.*, 2011; Figure 1.24]. Unfortunately there were no LIDAR surveys conducted during the 2005-2007 field seasons (the time period of greatest VLP-SP change) and the existing surveys were only performed once each season, and thus do not provide information on shorter time scale variations. An interesting feature of these surveys is that they show changes in the elevation and surface area of the lava lake over the past decade. Overall they indicate that the terminus of the magmatic system and crater floor have been generally subsiding since 2001, during which the lava lake dropped in elevation by over 20 m (an average rate of approximately 3 m/y) [*L. Jones, oral commun.*, 2011]. This change, which it should be emphasized was observed on a time scale of years and may be aliased in its sparse sampling, has not been observed on shorter time scales compable to the VLP-SP changes shown in Figure 1.11. It indicates, however, that the shallow uppermost conduit and lava lake system has undergone surface, and potentially underlying geometric, changes during the past decade. This contention is further supported by the ephermeral existence of a second lava lake at the Werner's Fumerole location a few hundred m from the principal lava [*Oppenheimer and Kyle*, 2008; see below].

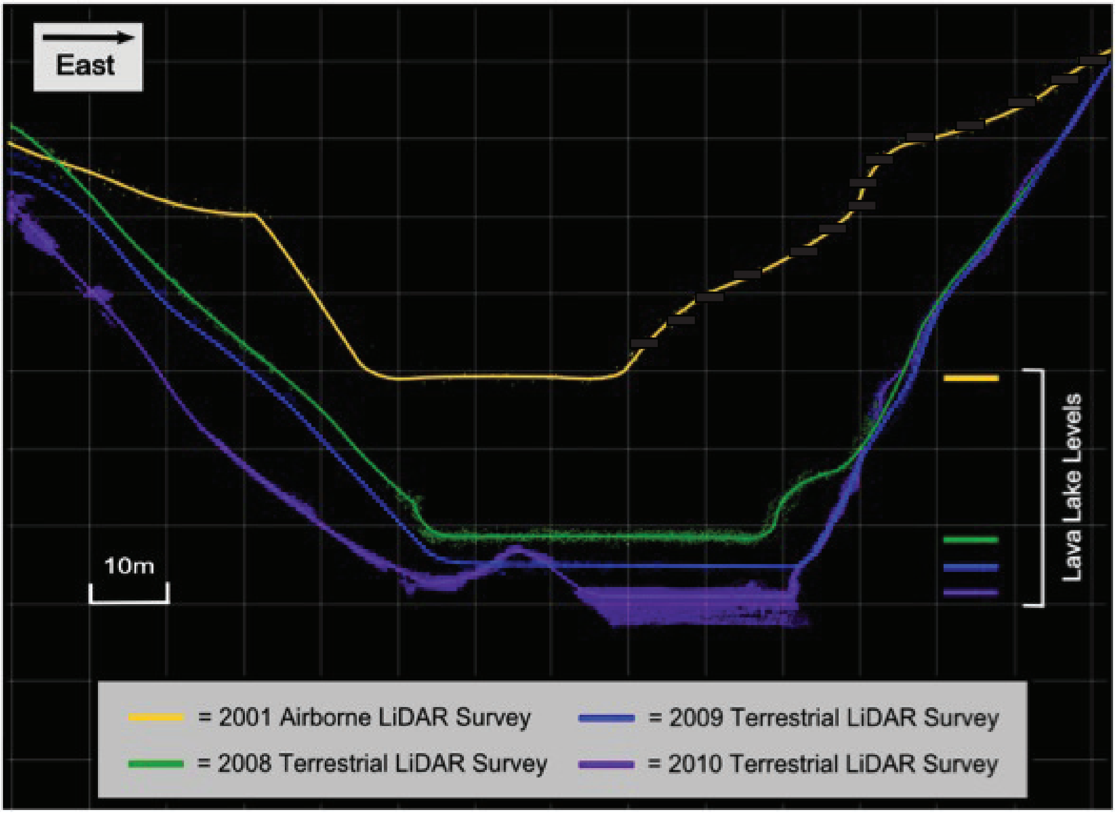

Figure 1.24: LIDAR profiles extracted from an airborne survey in 2001 and from terrestial surveys in 2008, 2009, and 2010. Note the general deflationary nature of the inner crater floor and lava lake surface (flat section of profile at bottom) across the study period. The eastern side of the airborne survey is represented by a dashed line because it is not fully registered with other profiles. The Inner Crater floor and lava lake surface elevation decrease exceeds 20 m.

1.7 Refinement of the Erebus Volcano Eruption Model and its VLP Triggering Mechanism

1.7.1 Review of Previously Proposed Eruption Model

Aster et al. [2003] elaborated on an eruption model for the Erebus Strombolian system that consisted of five phases. The first stage, which is not evident in the seismic record but is required for Strombolian eruptions, represents gas slug sequestration and growth (Figure 1.25: Stage 1). Knowledge of slug coalescence and sequestration has largely come from laboratory models [e.g., *Jaupart and Vergniolle*, 1988].

The second stage begins when the slug slips into the upper conduit system and ends near the top of the conduit when the slug ascends into the lava lake (Figure 1.25: Stage 2). During this phase, the rising slug displaces magma, which induces flow and produces pressure and traction forces on the conduit walls. Also, the slug is growing during this phase due to decompression and possibly ongoing coalescence [*Chouet et al.*, 2003; *James et al.*, 2006; *O'Brien and Bean*, 2008; *Gerst*, 2010]. This phase is at best marginally observed in the seismic data. This is supported by the short duration (< 5 s) of the pre-eruptive VLP at Erebus volcano and by results from laboratory experiments such as *James et al.* [2006].

The third stage begins when the slug nose ascends into the base of the lava lake, continues through the slug's rapid growth due to final decompression, and ends as the slug ruptures at the lava lake surface (Figure 1.25: Stage 3). This phase is seismically observed at the closest stations (< 700 m from the lava lake) in the polarity and amplitude-variable pre-eruption segment of the VLP signal. The final expansion of the lava lake system has also been well observed with radar [*Gerst*, 2010; *Gerst et al.*, 2012]. We believe that this signal variability evidences a

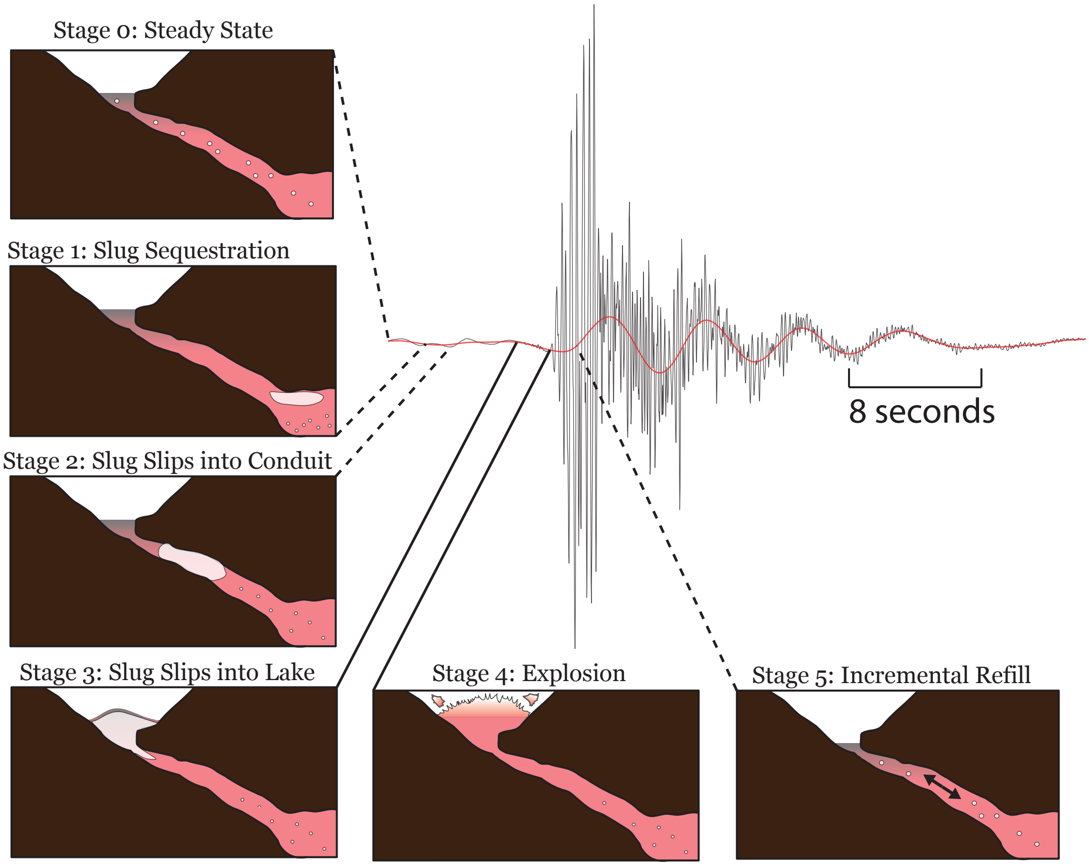

Figure 1.25: Schematic depiction of the Strombolian eruption mechanism at Erebus volcano, Antarctica with a representative vertical-component seismogram (E1S). The SP signal is shown in black and the VLP signal is shown in red. Linkage between stages and the seismogram are represented by either dashed or solid lines. The solid lines represent well constrained picks for the initiation of the stage, whereas dashed lines represent either stages not evident in the seismic record (Stages 0-2) or a stage when the start time cannot be constrained (Stage 5).

complicated process and that numerical and laboratory models hold the key to understanding this complexity. *James et al.* [2003] conducted laboratory experiments that investigated slug passage through a flare (significant increase in diameter) and showed that large amplitude pressure signals are generated. They also showed that during this passage, the individual slug may break up. This finding was further supported by *D'Auria and Martini* [2008], which attributed the break up in their numerical models to turbulence. Both studies observed a positive pressure pulse as the slug passed through the flare. Keeping these findings in mind, we propose that the pre-eruptive signal variability at Erebus volcano may be attributed to flow complexities induced by the following processes: 1) rapid decompression of the slug and its interaction with the lava lake's wall-rock, 2) turbulence generated when most of the slug passes through the constriction at the bottom of the lava lake, 3) break up of the slug due to turbulence, and 4) sinking of magma back into the conduit below the lava lake.

The fourth stage is the eruption, which we define as the rupturing of the magma shell above the slug and the venting of slug gases into the atmosphere (Figure 1.25: Stage 4). This stage is marked by the onset of the SP seismic signal, which is preceded by surface distention of the lava lake ($\sim$ 3 seconds before SP; Figure 1.1). *Gerst et al.* [2012] estimate slug overpressures to be in the range of $\sim$100-800 kPa and concluded that the slug's expansion just before rupture typically affects the entire lava lake surface (Radius $\approx$ 20 m). After shell burst, shell fragment bombs are thrown at distances of up to a kilometer [*Caldwell and Kyle*, 1994; *Kelly et al.*, 2008] and at velocities as high as 150 m/s. Most bomb fragments are confined to the inner and outer craters, but the largest events eject bombs out to $\sim$400 m from the lava lake. *Gerst* [2010] also estimated the erupted magma shell mass removed from the lava lake in larger recent explosions to range between 1,800 and 3,600 metric tons, with a corresponding volume of 900 - 1,800 m^3, assuming a bulk erupted magma density of 2,000 kg/m^3. Because the uppermost magma is highly vesicular (as observed in cooled bomb fragments), the actual volume removed from the lava lake is probably several times this value. Post-eruption, the lava lake is observed in video footage to be emptied to a depth of tens of meters, revealing a funnel-shaped uppermost geometry [e.g., *Gerst*, 2010; Figure 1.1].

The fifth stage is seismically represented by the post-eruptive VLP and represents the refilling and re-equilibration of the system. This stage begins some indeterminate time after stage four and concludes with lava lake reconstruction to its gravitational equilibrium. The source mechanism of the Erebus VLP has been explored by *Aster et al.* [2003, 2008a], which conclude that the extended VLP signal arises from the quasi-linear response of the summit region to the fluid dynamics of lava lake reconstruction. This conclusion was evidenced by the prolonged stability of the VLP signal, the approximate scaling between the VLP and SP amplitudes which indicates that the VLP is only slightly perturbed by eruptions, and the corresponding durations of the VLP and the refilling process. The VLP centroid source location was found to be several hundred m WNW of the lava lake at a depth of several hundred meters below the lake [*Aster et al.*, 2008a].

1.7.2 Delay Mediated by Post-eruptive VLP Initiation via Trapped Seismoacoustic Waves

We have demonstrated that the VLP-SP delay changes represent a broadband shift between the onset of the SP and post-eruptive VLP, and propose that the VLP-SP delay variation arises from an internal change. We further propose that this internal change affects the communication between unloading of the conduit (Figure 1.25: Stage 4) and a deeper pressure drop, which initiates the VLP response in the vicinity of the VLP centroid moment tensor [Figure 1.25: Stage 5; *Aster et al.*, 2008a]. This model is conceptually similar to the oscillatory response of a very high-hydraulic conductivity water well to head perturbations, such as is performed in a hydrologic slug test [e.g., *van der Kamp*, 1976], and is discussed by *Aster et al.* [2003].

Under the model that the VLP-SP delay represents a change in the communication time of gravitational disequilibrium to the VLP source region, we propose an extension to the eruption model to include another stage between the explosion and the post-eruptive refilling (Figure 1.26), which lasts up to a few seconds. Although it is difficult to determine precisely the duration of this stage, since the post-eruptive VLP likely represents the superposition of various forces and has no distinct onset, the variability in its overall timing is robustly determined to be $\pm$ 1 s (Figure 1.11). Calculations below are based on a minimum-length (straight and inclined) conduit and a representative location for the VLP centroid source from *Aster et al.* [2008] that is offset 200 m laterally and 400 m below the lake (a minimum lake surface-to-VLP source centroid conduit length of $l \approx 450$). We note that modeled delays will scale with l.

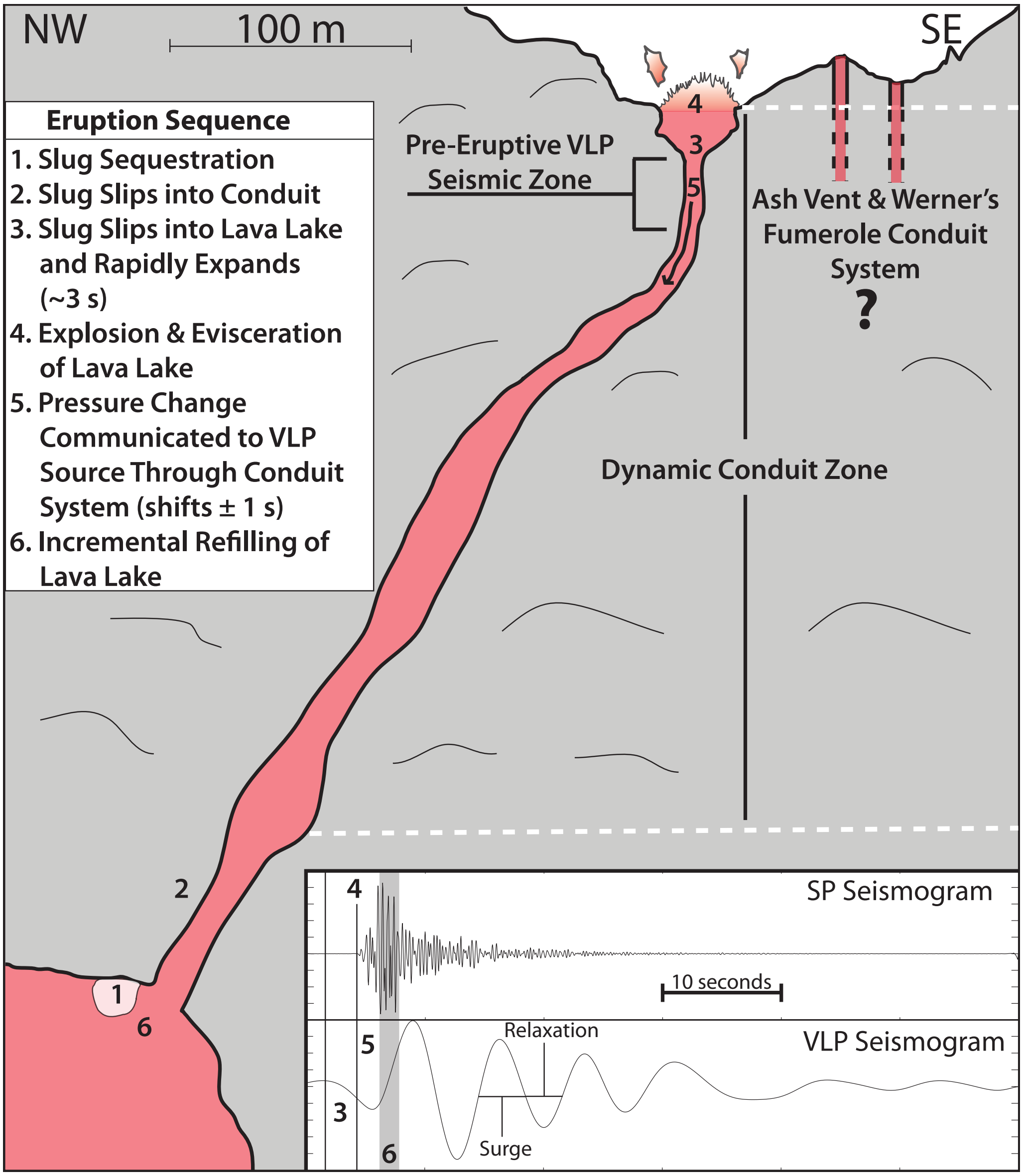

Figure 1.26: Conceptualization of the Erebus terminal conduit system. The fifth phase, which is introduced here, is an expansion on previously derived models for the eruptive sequence at Erebus Volcano (Figure 1.25) and is thought to be the process that induces variability in the VLP-SP delay. The conduit system under the sporadically active ash vent and Werner's Fumerole are not discussed here, but their presence supports the concept of geometric complexity in a dynamic conduit zone.

1.7.3 Post-eruptive VLP Initiation via Compressional or Stoneley Slow Waves

The simplest physical model for transmitting a pressure disturbance, as is created by removal of magma mass from the conduit tip in an eruption, to the VLP source is via a trapped seiosmoacoustic wave traveling through the magma-filled conduit at the P-wave velocity. First-order approximations of relevant compressional wave travel times can be drawn from *Dibble* [1994], who evaluated seismic velocity profiles in an Erebus phonolite magma column with varying water content and vesicularity. One-way travel times for each model were evaluated for a direct conduit of length $l = 450$ m between the surface and the VLP centroid and compared to see if an approximately ± 1 s change might be feasible via water content and/or vesicularity changes. The slowest *Dibble* [1994] model (1% water content and 75% surface vesicularity) had a calculated travel time of 1.95 s, while the fastest model (0.5 % water content, and 50% surface porosity) had a travel time of 0.84 seconds. This fairly large range of change thus is insufficient by a factor of ~ 2 to account for the observed variability in VLP-SP delays. Again, we note that these calculations use a minimum length of $l = 450$ m, and a more torturous (lengthy) conduit could proportionately improve agreement with the observations.

In a zone of high seismic density and elastic parameter contrast, such as a magmatic conduit embedded in a volcano, seismic energy will propagate as, and will become trapped in, dispersive boundary waves. A more realistic candidate for elastically transmitting the pressure disturbance from the surface to the VLP source region is thus via a Stoneley (boundary) slow wave. These wave types, like P-waves in highly vesicular magmas, can propagate at relatively low seismic wave velocities compared to the bulk consituents. *Korneev* [2007] explored this problem and derived an analytical solution for a thin fluid filled fracture, in which the fundamental mode phase velocity is given by

$$V_{f0} = \left(\frac{\omega h \mu}{\rho_f} (1 - \gamma^2) \right)^{1/3}$$

where $\omega = 2\pi f$, h is fracture thickness, μ is the shear modulus of the wall material, ρ_f is the fluid density, and γ is the wall material V_s/V_p ratio. This formula can be modified for a viscous system using a normalized skin factor

$$S = h\sqrt{\omega \rho_f / \nu}$$

to obtain the slow wave velocity

$$V_f = V_{f0} \left(\frac{\beta}{1 + \sqrt{\beta/3} + \beta} \right)^{1/3}$$

where $\beta = -\imath S^2/12$. The Korneev formulations can be shown to be assymtotic to those derived for slow boundary waves by *Ferrazzini and Aki* [1987].

We estimate the conduit thickness changes and dominant frequencies required for observed changes in the travel time of the pressure disturbance to the VLP centroid region (Figure 1.26). This model assumes that the post-eruptive VLP is initiated once the pressure disturbance travels from the surface of the lava lake to the VLP source for a distance l. A successful model must account that the travel time, to satisfy observed VLP-SP delay variations, can vary by approximately ±1 s (Figure 1.11) and therefore must permit only travel times somewhat greater than 1 s. Unfortunately, although the variation is well constrained, the absolute communication time is not because the VLP centroid signal is superimposed on the shallower-generated slug signal (Figure 1.25) and the VLP signal periods are long (>8 s) relative to the time shifts involved. Figure 1.27 illustrates the required velocity changes for increasing the lag by one second (decreasing the wave velocity) and decreasing the lag by one second (increasing the wave velocity). The calculations are truncated at velocities greater than 450 m/s for a straight conduit and at 900 m/s for a more tortuous (by a factor of two) conduit scenario because the associated travel times would be less than 1 s. This illustrates the relationship between effective length and model velocities in this evaluation. The shaded area in Figure 1.27 represents the inferred range of transitional velocities between the lag changes. Using these bounds and the Stoneley wave model described above, we can explore associated physical changes in an uppermost high-aspect cross-sectional ratio (crack-like) conduit that might be consistent with such velocity changes. We consider frequencies between $\sim$0.16 and $\sim$0.08 Hz to be consistent with the dominant seismic energy in the VLP signals, since they are likely comparable to the elastic communication of the unloading signal to the VLP source region.

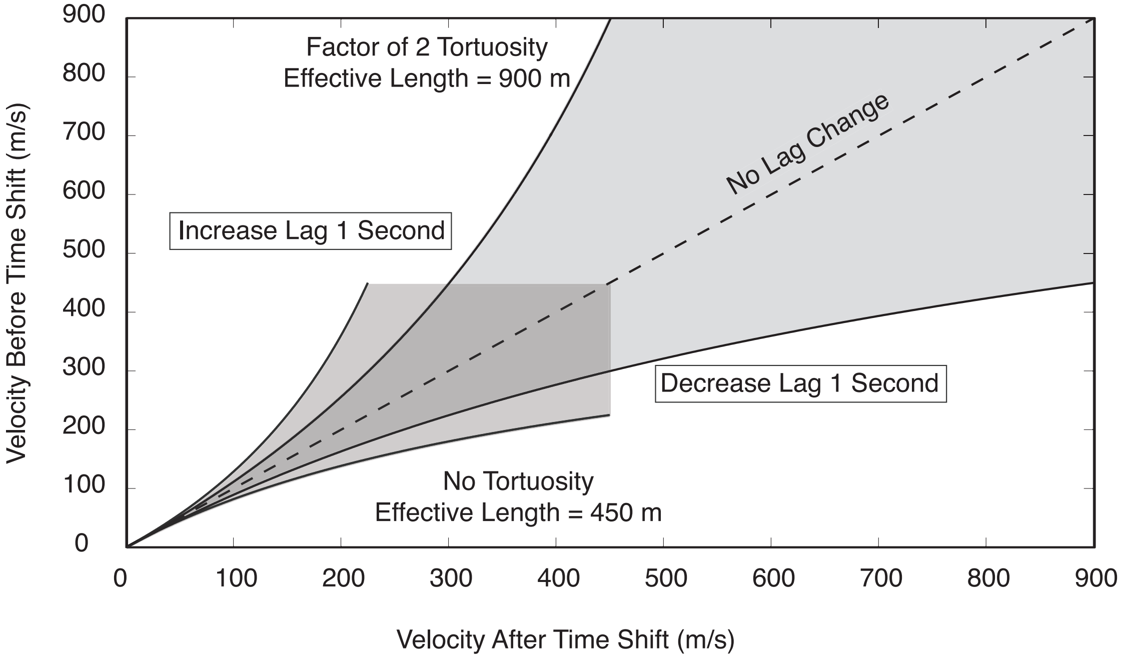

Figure 1.27: For conduit lengths of 450 m and 900 m and a minimum travel time of 1 s, changes in velocity required for a 1 s increase/decrease in VLP-SP lag time in the proposed conduit elastic communication model for temporal variations is presented. The shaded area represents the velocity variability associated with transitions between a ±1 s lag change. Note that here the conduit length is not only a function of the location of the VLP source, but includes lengthing due to conduit system tortuosity. A 900 m effective length represents a doubling of the estimated shortest distance between the surface of the lava lake and the estimated VLP centroid depth.

Calculations for the *Korneev* [2007] model used a fluid density of 2600 kg/m^3, a shear modulus of 3.9 GPa, a dynamic viscosity of 5000 Pa-s, a shear wave velocity of 1270 m/s, and a P-wave velocity of 2320 m/s [*Dibble et al.*, 1984; *Dibble*, 1994]. Results show that a 167 m/s phase velocity can be achieved for Stoneley waves with frequencies in the VLP band (at approximately 0.16, 0.12, and 0.08 Hz) for sub-lava lake dimension fracture thicknesses of approximately 7 , 9 , and 12 m (Figure 1.28). Near 0.16 Hz, a 1 s increase in travel time (a reduction in phase velocity to approximately 121 m/s), can be achieved by constricting the effective fracture width to approximately 4, 5, and 7 m, respectively. For a 1 s decrease in travel time, or a phase velocity of approximately 265 m/s, the effective fracture thicknesses would have to increase to 20, 26, and >35 m, respectively.

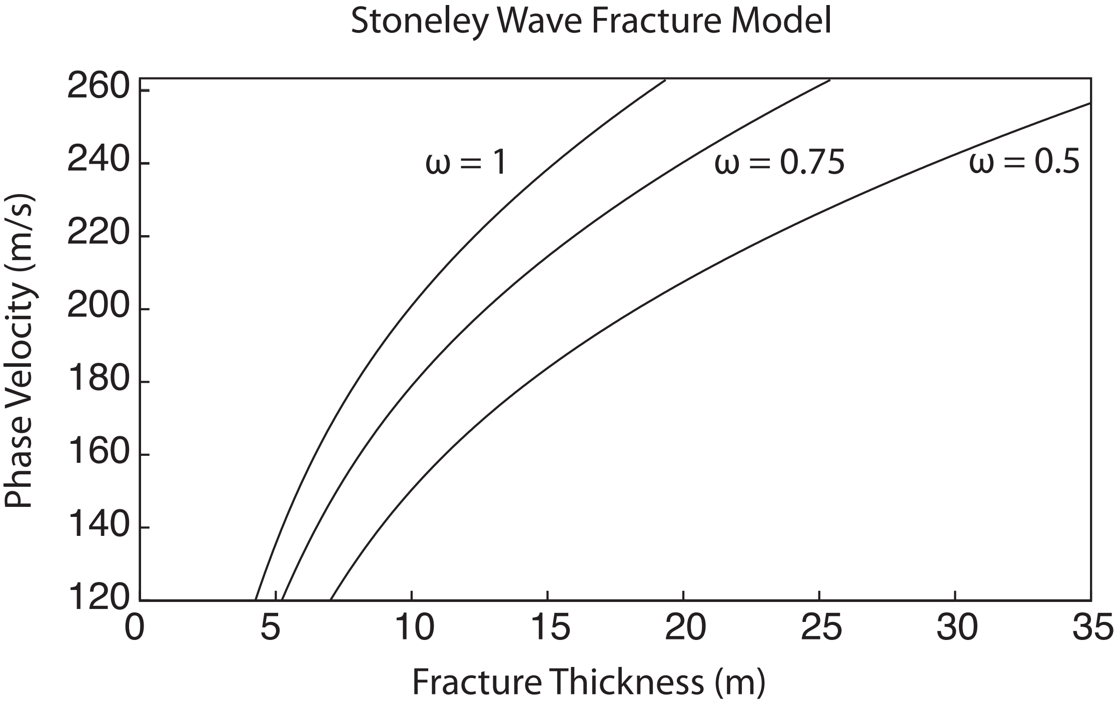

Figure 1.28: Dispersive Stoneley wave fracture model calculations for a system with Erebus geometry and physical properties (see text) from the formulation of *Korneev* [2008], where ω is radian frequency. A nominal phase velocity of approximately 167 m/s was calculated for the pressure disturbance communication for an initial effective conduit diameter of 7 to 12 m.

A more realistic scenario, rather than a changing width planar fracture, is that the geometry of the VLP source region to surface conduit system evolves via more widely distributed reorganization of connectivity with a more complex geometry. Given that the Stoneley waves have a sufficient wavelength and amplitude and that the division between individual fractures in the upper conduit system are of the same order as those wavelengths, then it is feasible that smaller changes in the thickness between the fractures could give rise to variable phase velocities of the necessary size and variability. In this view, a higher frequency Stoneley wave is propagated through a more complicated set of magma-filled fractures.

Koorneev [2007] also describes a Biot slow wave solution as the limiting case of a highly rigid conduit. Using the same parameters as above, this model resulted in much higher phase velocities at these low frequencies and required very small fracture thicknesses (<3 m), which seemed unlikely due to the open conduit conditions observed at Erebus volcano. Therefore, we conclude that the Biot wave model is a poor model in this type of volcanic setting, where a perpetually magma-filled conduit would be expected to elastically interact appreciably with low-rigidity wall material.

1.8 Mechanisms for Upper Conduit Variations

We propose that associated internal readjustments of the shallow conduit system create the modeled communicative delay variations between conduit tip lava lake eruptions and the initiation of magmatic flow and associated advective and pressurization forces in the VLP centroid region. Tomographic [*Zandomeneghi et al.*, 2011] and scattering inversion [*Chaput et al.*, 2012] results for the upper structure of Erebus volcano indicate that the uppermost conduit system of the volcano is indeed geometrically complex. Differences in H_2O/CO_2 ratios and HF content measured between the lava lake and a second ephemeral lava lake, Werner's Fumerole, further support a complicated multithreaded conduit system in the summit region [*Oppenheimer and Kyle*, 2008]. Closely spaced vents, suggestive of bifurcations and other complex uppermost conduit features, are common components of summit crater Strombolian systems [e.g., *Ripepe et al.*, 2007]. We thus propose that the noted long-term inner crater region deflation may be associated with internal changes in conduit system geometry occurring on week-to-month time scales that affect the upper conduit system. However, we recognize that this speculation is circumstantial; changes that effect VLP-SP delay and eruptive frequency could also occur within a magma filled conduit system due to assimilation, expansion, or partial, slow collapse of structural elements that would not necessarily couple to surface morphological changes.

Adjustments in the uppermost conduit system could also be driving the observed dramatic changes in eruptive frequency (Figure 1.4) by affecting slug formation and sequestration in the upper system. The strong variability of eruptive frequency for the Erebus lava lake system is contrary to its otherwise extraordinarily steady-state behavior, and Figure 1.20 indicates that changes in eruptive size distribution, and thus slug size, occur. Strong changes in degassing rate or gas content (including water) are thought to be unlikely due to the chemical stability and scale of the magmatic system [*Caldwell and Kyle*, 1994; *Kelly et al.*, 2008]. This suggests that eruptive frequency in this system is highly sensitive to changes in conduit geometry or other physical features of the conduit system [e.g., *Jaupart and Vergniolle*, 1988], such as those proposed here to explain the VLP-SP delay changes (as opposed to changes in the geochemical or vesicular properties of the magma).

1.9 Summary and Conclusions

We observe progressive temporal timing changes between eruption initiation (characterized by the SP origin time) and associated VLP seismic signals across a record of Strombolian eruption seismic observations spanning more than eight years (2003 - May 2011). These timing changes represent a variable and broadband delay of the oscillatory, stable, and minutes-long VLP signal, which is stimulated by gravitationally driven oscillatory recharge flow and viscoelastic response of the conduit system some hundreds of m below the lava lake, and the surface manifestation of the eruption caused by a slug burst. The reversible lag changes show approximately ±1 s of variation on time scales of up to several months. We examine correlations of these lag changes with phenomenological eruption observables such as eruption location within the lava lake, event size, and eruptive frequency. Within the limits of our observables, no clear association with these phenomena, other than a change in eruption size distribution during phase 1 of Figure 1.11, can be established.

We conclude that the variable delay reflects internal adjustments to the shallow conduit system that affect the elastodynamic communication time between the surface eruption and the magmatic system at VLP centroid depths, as mediated by elastic waves propagating through the uppermost conduit system. In contrast the deeper magmatic system geometry responsible for the extended VLP signal remains stable during this observation period. LIDAR imaging and other summit observations indicate that the lava lake system has been generally sinking into the inner crater since 2001, and we hypothesize that deflation-associated internal readjustments to conduit geometry are occurring within a shallow (above the VLP centroid depth) dynamic zone. Within this zone, changes that affect the VLP-SP delay could include inclination, lengthening/shortening, melting or freezing at the conduit walls and/or collapse or partial obstruction by geometrical readjustment. Such upper conduit changes might also influence the highly variable eruptive frequency of the volcano and the change in eruption size distribution, by influencing the near-summit conduit system's ability to assemble the characteristic large lake-spanning gas slugs observed in typical Erebus eruptions.

Acknowledgments

We thank UNAVCO and the IRIS PASSCAL Instrument Center at New Mexico Tech for facility support and field assistance on Mount Erebus. The facilities of the IRIS Consortium are supported by the National Science Foundation under Cooperative Agreement EAR-0552316, the NSF Office of Polar Programs and the DOE National Nuclear Security Administration. Donations of equipment from Extreme CCTV and VideoCommTechnologies were essential for video observations. We thank the many Raytheon Polar Services Company individuals and groups at McMurdo who made this field effort possible. This manuscript would not be possible with out the help and previous work provided by Brent Henderson. This research was supported by NSF Awards OPP-0229305, ANT-0538414, and ANT-0838817 and by New Mexico Tech Research and Economic Development.

References

Aki, K., and P. G. Richards (1980), *Quantitative Seismology*, Freeman, New York.

Aster, R., J. Lees, and J. Neuberg (2000), Broadband seismic and acoustic observations of volcanic seismicity (editorial), *J. Volcanol. Geotherm. Res., 101*, pp. vii-viii, doi:10.1016/S0377-0273(00)00154-2.

Aster, R., S. Mah, P. Kyle, W. McIntosh, N. Dunbar, J. Johnson, M. Ruiz, and S. McNamara (2003), Very long period oscillations of Mount Erebus Volcano, *J. Geophys. Res., 108* (B11), 2522, doi:10.1029/2002JB002101.

Aster, R., et al. (2004), Real-time data received from Mount Erebus Volcano, Antarctica, *Eos Trans. AGU, 85* (10), 97, doi:10.1029/2004EO100001.

Aster, R., D. Zandomeneghi, S. Mah, S. McNamara, D. B. Henderson, H. Knox, and K. Jones (2008a), Moment tensor inversion of very long period seismic signals from Strombolian eruptions of Erebus Volcano, *J. Volcanol. Geotherm. Res., 177* (3), pp. 635-647, doi:10.1016/j.jvolgeores.2008.08.013.

Aster, R., D. McNamara, and P. Bromirski (2008b), Multi-decadal climate-induced variability in microseisms, *Seism. Res. Lett., 79*, doi: 10.1785/gssrl.79.2.194.

Aster, R., B. Borchers, and C. Thurber (2012), *Parameter Estimation and Inverse Problems, Second Edition*, Elsevier Academic Press, 360 pp.

Bouche, E., S. Vergniolle, T. Staudacher, A. Nercessian, J. C. Delmont, M. Frogneux, F. Cartault, and A. Le Pichon (2010), The role of large bubbles detected from acoustic measurements on the dynamics of Erta 'Ale lava lake (Ethiopia), *Earth and Planetary Science Lett., 295* (1-2), pp. 37-48, doi: 10.1016/j.epsl.2010.03.020.

Caldwell, D., and P. R. Kyle (1994), Mineralogy and geochemistry of ejecta erupted from Mount Erebus, Antarctica between 1972 and 1986, in *Volcanological and Environmental Studies of Mount Erebus, Antarctica, Antarct. Res. Ser.*, vol. 66, edited by P. Kyle, pp. 147-162, AGU, Washington, D. C.

Chaput, J., R. Aster, and P. Kyle (2010), Noise tomography and Green's function estimates on Erebus Volcano, Antarctica, *Seism. Res. Lett., 81* (2).

Chaput, J., R. Aster, D. Zandomeneghi, H. Knox, and P. Kyle (2012), Imaging of Erebus volcano using body wave seismic interferometry of Strombolian eruption coda, *Geophys. Res. Lett.*, in press.

Chouet, B., P. Dawson, T. Ohminato, M. Martini, G. Saccorotti, F. Giudicepietro, G. De Luca, G. Milana, and R. Scarpa (2003), Source mechanisms of explosions at Stromboli Volcano, Italy, determined from moment-tensor inversions of very-long-period data, *J. Geophys. Res., 108* (B1), 2019, doi:10.1029/2002JB001919.

D'Auria, L., and M. Martini (2009), Slug flow: Modeling in a conduit and associated elastic radiation, in *Encyclopedia of Complexity and Systems Science*, edited by R. A. Meyers, pp. 81538168, Springer, New York.

De Lauro, E., S. De Martino, M. Falanga, and M. Palo (2009), Modelling the macroscopic behavior of Strombolian explosions at Erebus volcano, *Physics of the Earth and Planetary Interiors, 176*,pp. 174-186, doi: 10.1016/j.pepi.2009.05.003.

Dibble R., J. Kienle, P. Kyle, and K. Shibuya (1984), Geophysical studies of Erebus Volcano, Antarctica, from 1974 December to 1982 January, *N.Z.J. Geol. Geophys.*, 27, pp. 425-455.

Dibble, R. (1994), Velocity modeling in the erupting magma column of Mount Erebus, Antarctica, in *Volcanological and Environmental Studies of Mount Erebus, Antarctica, Antarct. Res. Ser.*, vol. 66, edited by P. Kyle, pp. 17-33, AGU, Washington, D. C.

Dibble, R.R., P. R. Kyle, and C. A. Rowe (2008), Video and seismic observations of Strombolian eruptions at Erebus Volcano, Antarctica, *J. Volcanol. Geotherm. Res. 177* (3), pp. 619-634, doi: 10.1016/j.jvolgeores.2008.07.020.

Ferrazzini, V., and K. Aki (1987), Slow waves trapped in a fluid-filled infinite crack: Implications for volcanic tremor, *Journal of Geophysical Research, 92* (B9), pp. 9215-9223, doi:10.1029/JB092iB09p09215.

Garces, M. (2000), Theory of acoustic propagation in a multi-phase stratified liquid flowing within an elastic-walled conduit of varying cross-sectional area, *J. Volcanol. Geotherm. Res., 101* (1-2), pp. 1-17, doi:10.1016/S0377-0273(00)00155-4.

Gerst, A. (2010), The First Second of a Strombolian Volcanic Eruption, Dissertation (Doctorate in Natural Sciences), Institute of Geophysics, University of Hamburg, Germany.

Gerst, A., M. Hort, R.C. Aster, J.B. Johnson, and P.R. Kyle (2012), The First Second of a Strombolian Volcanic Eruption, in review, *J. Geophys. Res.*.

Giggenbach, W., P. Kyle, and G. Lyon (1973), Present volcanic activity on Mt. Erebus, Ross Island, Antarctica, *Geology, 1*, pp. 135-136.

Henderson, D.B. (2007), Analysis of seismic similarity in Strombolian eruptions from Mount Erebus, Antarctica, M.S. Thesis, New Mexico Institute of Mining and Technology, Socorro, New Mexico.

James, M., S. Lane, B. Chouet, and J. Gilbert (2004), Pressure changes associated with the ascent and bursting of gas slugs in liquid-filled vertical and inclined conduits, *J. Volcanol. Geotherm. Res., 129* (1-3), pp. 61-82, doi:10.1016/S0377-0273(03)00232-4.

James, M., S. Lane, and B. Chouet (2006), Gas slug ascent through changes in conduit diameter: laboratory insights into a volcano-seismic source process in low-viscosity magmas, *J. Geophs. Res. 111*, B05201, doi:10.1029/2005JB003718.

Jaupart, C. and S. Vergniolle (1988), Laboratory models of Hawaiian and Strombolian eruptions, *Nature 331* (7), pp. 58-60, doi:10.1038/331058a0.

Johnson, J. B., R. C. Aster, and P. R. Kyle (2004), Volcanic eruptions observed with infrasound, *Geophys. Res. Lett. 31*, L14604, doi:10.1029/2004GL020020.

Johnson, J.B., and R. C. Aster (2005), Relative partitioning of acoustic and seismic energy during Strombolian eruptions, *J. Volcanol. Geotherm. Res., 148*, pp. 334-354, doi:10.1016/j.jvolgeores.2005.05.002.

Johnson, J. B., R. C. Aster, K. R. Jones, P. R. Kyle, and W. C. McIntosh (2008), Acoustic source characterization of impulsive Strombolian eruptions from the Mount Erebus lava lake, *J. Volcanol. Geotherm. Res. 177* (3), pp. 673-686, doi:10.1016/j.jvolgeores.2008.06.028.

Johnson, J. B. and K. R. Jones (2010), Mapping complex vent eruptive activity at Santiaguito, Guatemala using network infrasound semblance, *J. Volcanol. Geotherm. Res., 199* (1-2), pp.15-24, doi:10.1016/j.jvolgeores.2010.08.006.

Johnson, J. B., J. M. Lees, and N. Varley (2010), Characterizing complex eruptive activity at Santiaguito Volcano, Guatemala using infrasound semblance in networked arrays, *J. Volc. Geotherm. Res., 199* (1-2), pp. 1-14, doi:10.1016/j.jvolgeores.2010.08.005.

Jones, K. R., J. B. Johnson, R. C. Aster, P. R. Kyle, and W. C. McIntosh (2008), Infrasonic tracking of large bubble bursts and ash venting at Erebus Volcano, Antarctica, *J. Volcanol. Geotherm. Res. 177* (3), pp. 661-672, doi:10.1016/j.jvolgeores.2008.02.001.

Julian, B. (1994), Volcanic tremor: Nonlinear excitation by fluid flow, *J. Geophys. Res. 99* (B6), pp. 11,859-11,877, doi:10.1029/93JB03129.

Kaminuma, K. (1994), The Seismic Activity of Mount Erebus in 1981-1990, in *Volcanological and Environmental Studies of Mount Erebus, Antarctica, Antarct. Res. Ser.*, vol. 66, edited by P. Kyle, pp. 35-50, AGU, Washington, D. C.

Kelly, P. J., P. R. Kyle, N. W. Dunbar, and K. W. W. Sims (2008), Geochemistry and mineralogy of the phonolite lava lake, Erebus Volcano, Antarctica: 1972-2004 and comparison with older lavas, *J. Volcanol. Geotherm. Res. 177* (3), pp. 589-605, doi:10.1016/j.jvolgeores.2007.11.025.

Korneev, V. A. (2008), Slow waves in fractures filled with viscous fluid: *Geophysics, Vol. 73*, No 1, pp. 1-7.

Korneev, V. A. (2010), Low-frequency fluid waves in fractures and pipes: *Geophysics, Vol. 75*, No 6, pp. 97-107.

Kyle, P. R., R. R. Dibble, W. F. Giggenbach, and J. Keys (1982), Volcanic activity associated with anorthoclase phonolite lava lake, Mount Erebus, Antarctica, in *Antarctic Geoscience*, edited by C. Craddock, pp. 734-745, University of Wisconsin Press, Madison.

Lyons, J. J., and G. P. Waite (2011), Dynamics of explosive volcanism at Fuego Volcano imaged with very long period seismicity, *J. Geophys. Res., 116*, B09303, doi:10.1029/2011JB008521.

O'Brien, G. S., and C. J. Bean (2008), Seismicity on volcanoes generated by gas slug ascent, *Geophys. Res. Lett., 35*, L16308, doi:10.1029/2008GL035001.

Nishimura, T., H. Nakamichi, S. Tanaka, M. Sato, T. Kobayashi, S. Ueki, H. Hamaguchi, M. Ohtake, and H. Sato (2000), Source process of very long period seismic events associated with the 1998 activity of Iwate Volcano, northeastern Japan, *J. Geophys. Res., 105* (B8), pp. 19,135-19,147, doi:10.1029/2000JB900155.

Parfitt, E.A. (2004), A discussion of the mechanisms of explosive basaltic eruptions, *J. Volcanol. Geotherm. Res. 134* (1-2), pp. 77-107, doi:10.1016/j.jvolgeores.2004.01.002.

Ripepe, M., Marchetti, E., Ulivieri, G. (2007), Infrasonic monitoring at Stromboli volcano during the 2003 effusive eruption: Insights on the explosive and degassing process of an open conduit system, *J. Geophys. Res. 112* B09207, doi:10.1029/2006JB004613.

Rowe, C. (1988), Seismic velocity structure and seismicity on Mount Erebus Volcano, Ross Island, Antarctica, M.S. thesis, University of Alaska, Fairbanks.

Rowe, C. A., R. C. Aster, P. R. Kyle, J. W. Schlue, and R. R. Dibble (1998), Broadband recording of Strombolian explosions and associated very-long-period signals on Mount Erebus Volcano, Ross Island, Antarctica, *Geophys. Res. Lett. 25* (13), pp. 2297-2300, doi:10.1029/98GL01622.

Rowe, C. A., R. C. Aster, P. R. Kyle, R. R. Dibble, and J. W. Schlue (2000), Seismic and acoustic observations at Mount Erebus Volcano, Ross Island, Antarctica, 1994 -1998, *J. Volcanol. Geotherm. Res. 101* (1-2), pp. 105-128, doi:10.1016/S0377-0273(00)00170-0.

Shearer, P. (1994), Global seismic event detection using a matched filter on long-period seismograms, *J. Geophys. Res., 99* (B7), pp. 13,713-13,725, doi:10.1029/94JB00498.

Van der Kamp, G. (1976), Determining aquifer transmissivity by means of well response: The underdamped case, *Water Resour. Res., 12*, pp. 71-77, doi:10.1029/WR012i001p00071.

Wright, R. and E. Pilger (2008), Satellite observations reveal little inter-annual variability in the radiant flux from the Mount Erebus lava lake, *J. Volcanol. Geotherm. Res. 177* (3), pp. 687-694, doi:10.1016/j.jvolgeores.2008.03.005.

Zandomeneghi, D., R. Aster, A. Barclay, J. Chaput, and P. Kyle (2011), Tomographic high-resolution 3D imaging of the shallow magmatic system of Erebus Volcano, Antarctica, *Eos Trans. AGU*, Fall Meet. Suppl.

CHAPTER 2

SHALLOW ICEQUAKES IN A COLD GLACIAL ENVIRONMENT ASSOCIATED WITH SEASONAL TEMPERATURE VARIATIONS AT EREBUS VOLCANO, ANTARCTICA

Abstract

We examine non-eruptive seismic events recorded at Erebus volcano to assess their general frequency, size, seasonality, geographic distribution, and mechanisms. In this study, we utilize both long-running and temporary dense deployments of seismographs spanning seven years (2003-2009). A subset of well-observed icequakes recorded by the long-running Mount Erebus Volcano Observatory (MEVO) in consort with two dense temporary networks deployed during 2007 through 2008 was further analyzed. The MEVO network consists of six broadband and up to nine short period stations with accompanying environmental data streams. The dense arrays consisted of 24 broadband stations arranged in two concentric rings around the volcano and 99 short period stations deployed near the summit of the volcano and along the Mount Terror-Mount Erebus east-west axis of Ross Island. During each of the seven years of this study, we detected a large number of large noneruptive event swarms (up to many hundreds of distinct impulsive events per day) that show a highly seasonal pattern of occurrence. We find that ∼43% of the events occur between March and May and ∼30% occur between October and December in this high-elevation (above 2000 m), cold (∼-10°C to ∼-60°C annually), and dry Antarctic glacial environment. These are both periods when rapidly changing ambient air temperatures arise due to the high latitude disappearance/appearance, respectively, of the sun at the far southerly (∼78°S latitude) of the volcano. While events within the crater can be attributed to rockfalls and vent activity, we conclude that the vast majority of non-eruptive events elsewhere on the volcano are due to brittle fracturing of the cold and shallow firn/ice regime driven by air temperature thermal variations that induce contractional or expansional strains.

2.1 Introduction

The discrimination of glacial versus volcanic events on active and dormant glaciated volcanoes is an important problem in volcanology. Due to highly heterogeneous structure, seismograms at volcanoes are typically very strongly influenced by path or site effects. Because of strong path effects, diverse sources, especially when observed by band-limited (such as short period) instruments, can produce markedly similar seismograms. Event similarity, precise location, glacialogical interpretation, seasonality, or other attributes may thus be necessary to address the critical question as to whether an event swarm on a volcano is volcanic, tectonic, or glaciological in origin [e.g., *West et al.*, 2010; *Allstadt et al.*, 2011]. In addition, non-volcanic seismic events, if well recorded and located, offer the possibility of usefully enhancing studies of the internal structure of the volcano. Here, we specifically examine a relatively well-monitored seismogenic glacial system that is controlled by a very cold and dry climate with slow flow rates and extremely limited or zero surface or subglacial melt.

In recent years, significant strides have been made in observing and understanding the dynamic underpinnings of cryospheric seismology. Many of these studies have focused on key processes involving basal tractions and basal stick-slip behavior, as observed in both polar and temperate glacial systems [e.g., *Wolf and Davies*, 1986; *Anandakrishnan and Bentley* 1993; *Anandakrishnan et al* 1998; *Binschadler et al.*, 2003; *Anandakrishnan and Winberry* 2004; *Wiens et al.*, 2008; *Walter*, 2009]. New types of seismic sources associated with calving [*Ekstrom et al.*, 2006; *Tsai and Ekstrom*, 2007; *O'Neel et al.*, 2007; *Tsai et al.*, 2008], water transport [e.g., *Walter*, 2009], iceberg basal and lateral stick slip [*MacAyeal et al.*, 2008; *Martin et al.*, 2010], and ice shelf rifting [e.g., *Bassis et al.*, 2007] highlight the ubiquity of cryospheric seismic sources. Fundamentally, sources of seismic signals include calving or other collapse, accelerated strain along internal or bed shear faults or shear zones, or are localized to associated cracks within ice, and hydraulic transients within glacial water channels [*Qamar*, 1988]. Hybrid events attributed to several forcing mechanisms have also been observed, for example in tidewater systems [*West et al.*, 2010]. A number of studies have examined the key process of basal lubrication and the role of water in glacial seismicity. The amount and pressure of basal water may be driven by seasonal temperature variations at the surface of the glacier or ice cap when melt is present. Furthermore, seasonal patterns in surface water influx have been shown to play an important role for earthquakes near glaciers; this was the case for seasonal events observed at Mt. Ogden [e.g., *Wolf et al.*, 1997].

Few studies to date have investigated the seismicity of very cold glaciers. The extremely cold and dry climate on Erebus volcano is representative of small to medium sized perpetually subfreezing alpine regimes. In this environment, basal lubrication is unlikely, the role of liquid water is negligible or non-existent, and glacial strain rates are low. The fastest glacial flow on the volcano has been attributed to the near-tidewater regions of Erebus Glacier and its Glacial Tongue [e.g., *Squire et al.*, 1994], where tidewater velocities are approximately 150 m/year. Glacier velocities at the high (above 2000 m) elevations relevant to this study are not presently well constrained, but are certainly much slower than in the lower Erebus Glacier system.

Since much of Erebus volcano is covered in snow rather than ice, it is important to understand how snow and ice differ mechanically and whether seismic energy has been observed from fracturing snow. Concerning the mechanical properties of snow versus ice, great efforts have been undertaken for snow in alpine regions [*Petrovic*, 2003; *Schweizer et al.*, 2003], but little research has been performed on Antarctic snow, which is appreciably different than alpine snow. The studies conducted in alpine regions illustrate that snow/firn is typically regarded as a cellular form of ice, with much lower levels of fracture toughness and strength but that little is known about the material's mechanical properties [i.e. *Petrovic*, 2003] . Other work has shown that warming of snowpack causes a significant decrease in hardness, an increase in toughness, and a slight decrease in strength of weak layer interfaces in snow slabs; all of these effects decrease the stability of the slab[*Schweizer et al.*, 2003].

Although these findings are important for understanding how snow fractures and what types of changes create instabilities, it is important to look into the seismic record for evidence of fracturing snow in the absence of avalanches. This distinction is of the utmost importance for this study since avalanches have not been observed at Erebus volcano and are though to be an unlikely phenomena. *Lawrence and Bradley* [1977] observed a variety of signal types associated with snow instability; one of which was determined to represent internal fracturing of snow. This conclusion was based on the events' calculated origins, the lack of detections in the absence of snow cover, and the lack of snow displacements. These signals were noted as being impulsive, short in duration, and of very low amplitudes [*Lawrence and Williams*, 1976].

Here, we quantitatively analyze the non-crater-region seismicity of Erebus volcano for event rate, onset, duration, and coda development characteristics, and assess implications for source mechanisms on yearly, monthly, and daily scales. The goal is to provide a first study of non-eruptive event phenomenology across an extended period of time, including event temporal variability, geographic distribution, source mechanism and size. To construct a new catalog of events, all available MEVO continuous seismic data were organized into an Antelope Database [e.g., *Pesaresi*, 2011]. This database spans completion of the permanent broadband network in 2003 through the beginning of 2010 (10-15 operational stations), as well as data recorded from the extensive broadband (24 stations) and short period (99 stations) IRIS PASSCAL deployments of 2007-2008 and 2008, respectively (Figure 2.1).

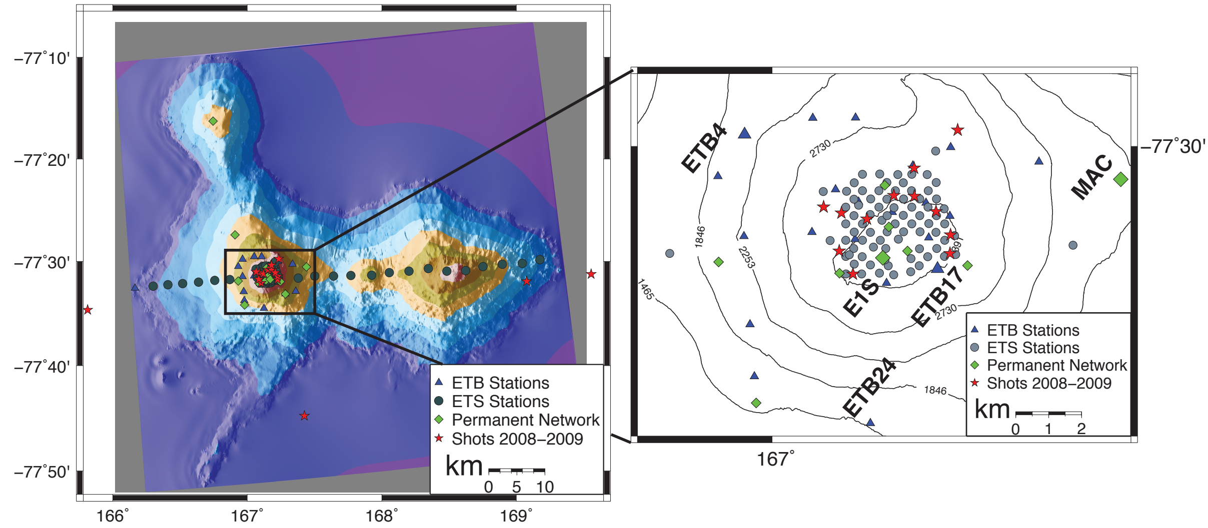

Figure 2.1: (Left) Map of Ross Island, Antarctica and the general distribution of stations for the three deployments utilized in this study. (Right) Dense deployment implemented for 3D tomographic imaging efforts. The station naming conventions are as follows: ETB stations are broadband (Guralp 40T 30 s seismometers) stations deployed in 2007-2008 and the ETS stations are the 99 short period (Serce; L-28-3D 4.5 Hz) stations deployed in 2008. Shot locations employed during the tomographic experiment are also illustrated in both figures.

2.2 Antelope Database Processing

A Short Term Average/Long Term Average (STA/LTA) detector was designed and optimized to maximize detection of general impulsive seismicity in the seismic records. The best determined STA/LTA parameters, based on a study of limited time periods, was a short-term average time window length of 10 s and a long-term average time window length of 80 s, with a triggering threshold of 5. All the data were band-pass filtered with a four-pole causal Butterworth filter between 1.0 and 8.0 Hz to isolate the short-period signal band and reject the prominent microseism signal at longer periods. Once STA/LTA detections were determined for each station, a travel time grid was developed that covered the majority of Ross Island to a depth of 12 km below the summit ($\sim$8 km below sea level). The grid nodes were spaced at approximately 300m in both the N-S and E-W directions.

We evaluated the accuracy of the STA/LTA picks in Antelope by visually reviewing several of the events occurring during the dense deployments. The results from this analysis showed that in general the program was making good picks (Figure 2.2). Poorer quality picks were observed, however, when signals were particularly emergent (Figure 2.3), weak, or otherwise complicated by multiply occurring events (Figure 2.4).

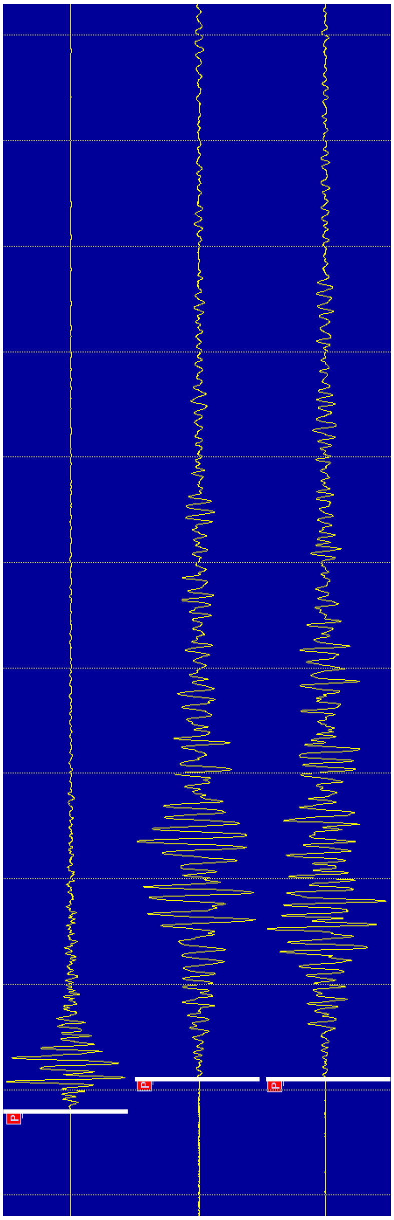

Figure 2.2: Accurate pick from the STA/LTA Antelope Processing.

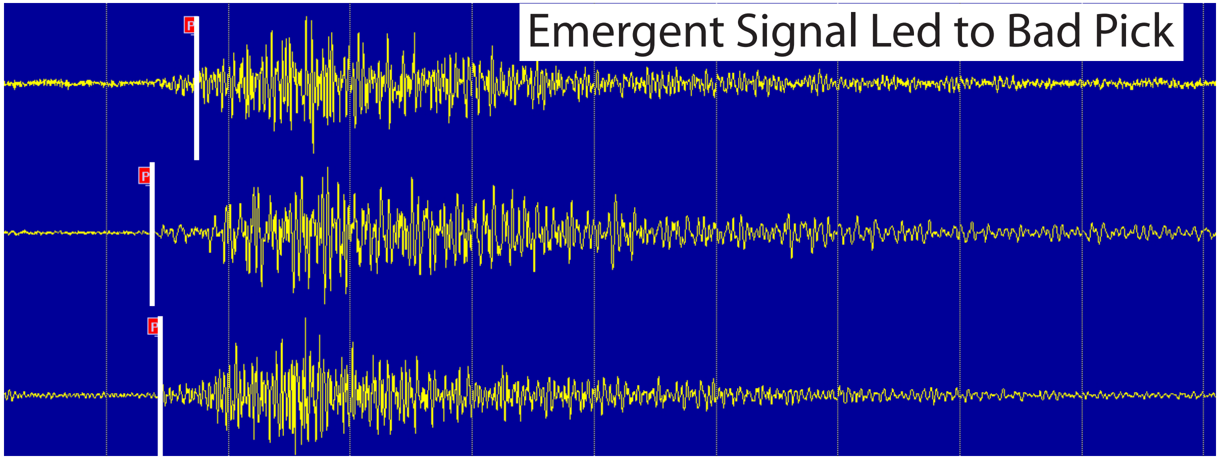

Figure 2.3: STA/LTA bad pick due to the particularly emergent character of the event recorded at this station.

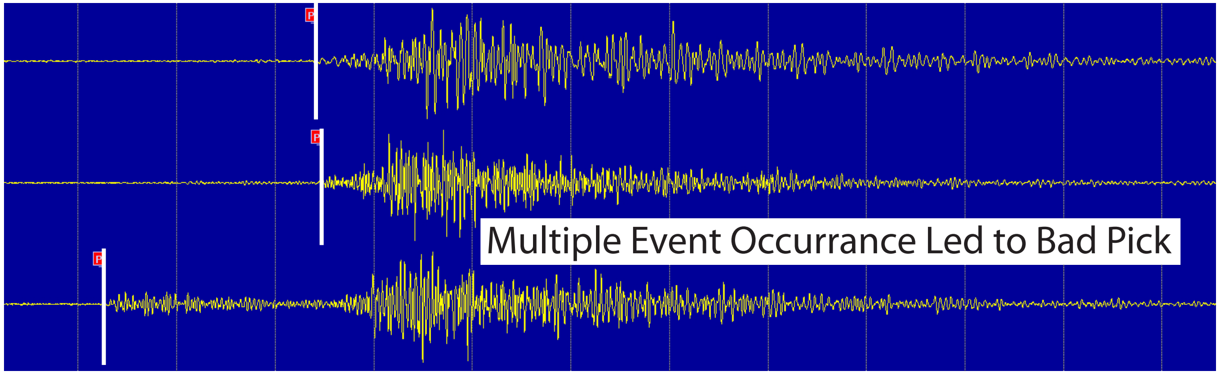

Figure 2.4: STA/LTA bad pick due to the occurrence of multiple events at or near this station.

We next designed and implemented a trigger associator to identify causally linked network detections for which locations could be determined. Association of detections into an event required a minimum of four travel time-consistent stations. For periods when the large temporary networks were deployed, two event catalogs were created: 1) those identified by at least four permanent network stations (to facilitate consistency with other time periods) and 2) those identified by a minimum of any four stations in the larger network.

Given an event association defined by consistent triggers at four or more stations, initial (P-wave) arrivals were processed to estimate event locations using a simple velocity model for Erebus volcano. A range of uniform velocities (3.9 to 4.3 km/s) were chosen and tested based on the estimates of *Dibble et al.*, [1994] and *Maraj* [2011]. This procedure produced a catalog of initial event locations that was sufficient to determine the general geographic distribution (especially azimuthally with respect to the crater) of detected events.

We estimate the errors associated with these locations and assess the best velocity model by estimating locations and times for 12 constrained active source shallow detonations conducted during the 2008-2009 field season (Figure 2.1; Table 2.1; *Zandomeneghi et al.*, 2011). In this comparative study, we determine that shot location residuals were never greater than 171 m, elevation residuals were no greater than 50 m, and origin time errors were no larger than approximately 0.32 s. These residuals are considered to be minimum errors associated with events that occur outside of the dense deployment of ETS stations.

Next, we identified eruptions in the event catalog by scanning the continuous broadband records (MEVO stations) with a multichannel (seismic/infrasound) matched filter [*Knox et al.*, 2011] that was empirically tuned as an eruption discriminant. This effort resulted in the identification of 2,837 eruptions from the

Table 2.1: Velocity Models and Associated Errors Calculated From 12 Known Shots

Velocity Model	Velocity (km/s)	Mean Absolute Location Residual (m)	Mean Absolute Elevation Residual (m)	Mean Absolute Timing Error (s)
Erebus3	4.2 km/s	137.2	10.5	0.313
Erebus4	4.1 km/s	133	20.2	0.291
Erebus5	4.0 km/s	170.9	46.7	0.256
Erebus6	3.9 km/s	136.7	49.7	0.250

catalog, leaving 84,317 non-eruptive events recorded on the three networks between January 1, 2003 and December 31, 2009. Using only the permanent network stations, the final catalog with the matched filter detected eruptions removed included 69,407 non-eruptive events. Approximately 75% of all detected and associated events in the catalog occur outside of the crater. The geographic distribution of these events trended toward Cape Adare and the Transantarctic Mountains. Although this trend could correspond to ice related seismicity, it likely represents a bias introduced by the station configuration and the relatively simple velocity model.

2.3 Non-Eruptive Seismicity of Mount Erebus

Characteristic non-eruptive events show similar frequency content to eruptive events from the lava lake and to seismic shots, with dominant frequencies between 1-10 Hz. Impulsive or semi-impulsive onsets are visible only at the closest stations (less than $\sim$1 km), and initial arrivals rapidly become emergent at greater distances. Larger events show rapid development of a seismic codas with durations of up to tens of s (Figure 2.5). At close distances, events show frequency content of up to 20 Hz, but these highest frequencies are lost after only a few hundreds of meters of propagation. The largest events that occurred during the temporary network deployments were evident across the entire network (∼10 km diameter, Figure 2.6). The events commonly occur in swarms of up to several hundred events per day (Figure 2.7).

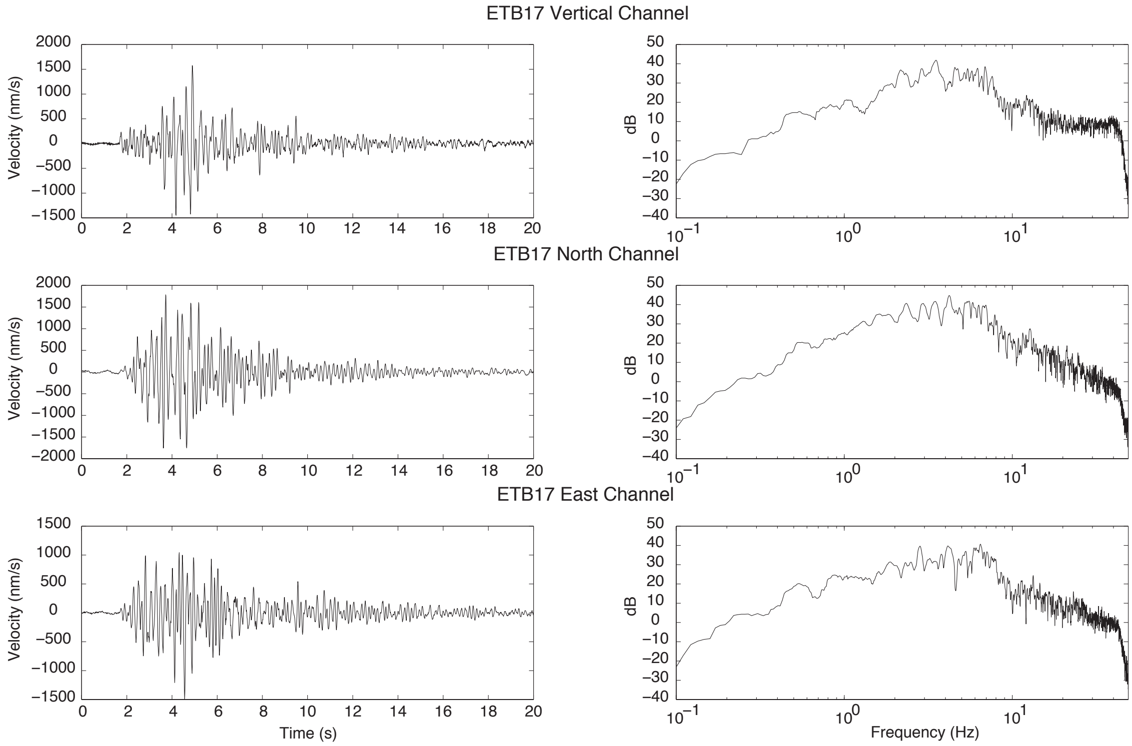

Figure 2.5: (Left) Typical non-eruptive event velocity seismograms recorded at a nearby (∼1 km from source) station, ETB 17, located on the edge of the upper plateau (Figure 2.1); note the impulsive onset, the short duration, coda envelope development, and lack of obvious S phases. This signal was recorded with a sampling rate of 100 Hz has been filtered above 1 Hz to remove the strong oceanic microseism (this same event is shown in Figure 2.6). (Right) Amplitude spectra for the seismograms at left, showing dominant frequencies are between 1 and 10 Hz.

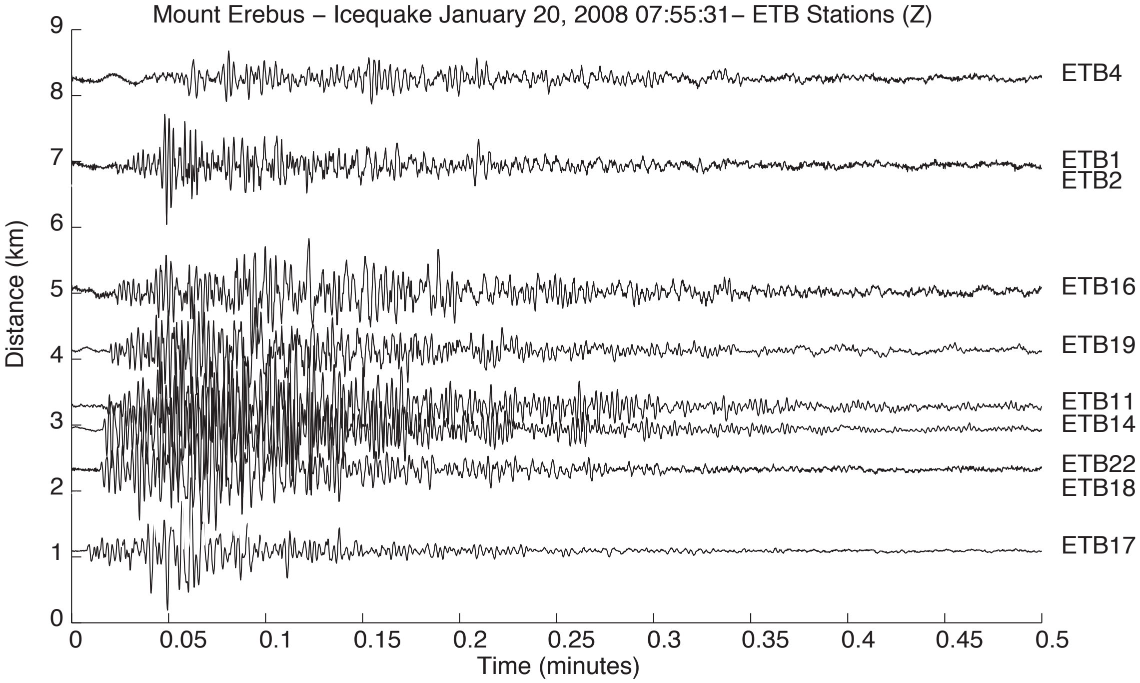

Figure 2.6: Amplitude-normalized velocity seismograms of the same event as Figure 2.5 recorded across the ETB network (Figure 2.1). End section stations ETB17 and ETB4 are on opposite sides of Erebus Volcano and are located approximately 7 km apart. Note the development of a strong coda, and that the first arrival rapidly changes from impulsive to highly emergent within a few km due to the highly scattering medium of the volcano.

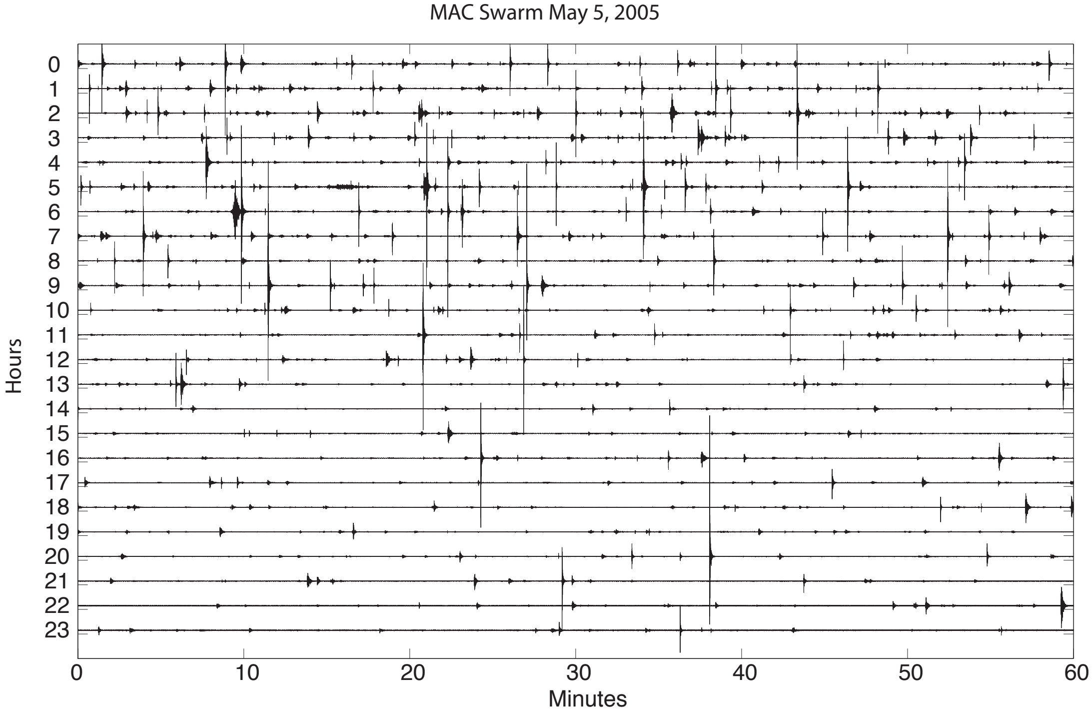

Figure 2.7: Vertical velocity seismograms from a typical event swarm, recorded on May 5, 2005, by short-period station MAC (Figure 2.1). Typical event detection rates are tens of events per hour and hundreds of events per day.

The seismograms of Figure 2.6 demonstrate the high degree of short-period seismic scattering characteristic of many volcanoes, where the free scattering path for body waves can be up to three orders of magnitude smaller than that of typical crust [*Wegler*, 2004]. The rapid attenuation of higher frequency energy also indicates that the events are shallow and/or that the intrinsic Q of the medium is low. These strong propagation effects dominate short-period seismic signals after approximately 1 km of propagation. Figure 2.8 shows time series and spectra for a shot, a Strombolian eruption, and an icequake recorded at various distances (up to $\sim$5.3 km). Note that all three signals become similar in the time and frequency domains after only a few km of propagation through the highly heterogeneous volcano. Again, the effects of seismic attenuation are also visible at higher frequencies.

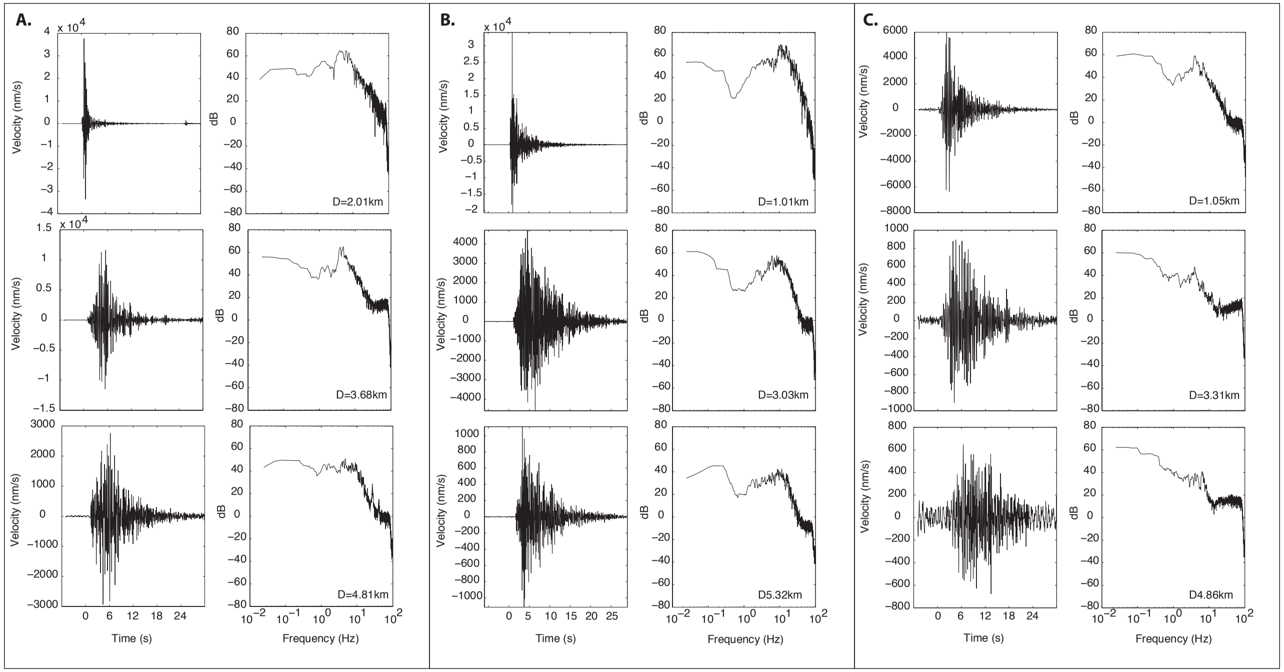

Figure 2.8: Time series and amplitude spectra from: A) an event on December 22, 2008; B) an active source shot detonated at Cones on December 21, 2008; C) a small Strombolian lava lake eruption on December 7, 2008. The three signal sets are shown for recording distances out to approximately 5 km, illustrating the development of the coda and rapid attenuation of higher frequencies. All time series were recorded at 200 samples/s. The signals shown to the left in each panel have been filtered between 1 and 10 Hz so that the strong oceanic microseism component (which frequently obscures weaker signals) is removed. The associated spectra are unfiltered and show the two distinct frequency bands (microseism and source associated frequencies). The amplitudes have not been corrected for site responses (e.g., snow versus rock), which have been noted to create significant short-period amplitude effects. Note generally that the three signals are all of similar duration, contain approximately the same frequencies, have similar time-domain envelopes, and exhibit strong high frequency attenuation.

2.4 Results

2.4.1 Geographic Distribution of Non-Eruptive Seismic Signals

We assess the location of Erebus and Ross island non-eruptive seismic events by examining the geographic distribution of events that were associated using 50 or more stations during the 2008 temporary network deployment. This threshold was chosen because it maximizes the tradeoff between reasonable locations and a significant number of events/locations. We identified 277 events between 12/09/2008 and 12/26/2008. Removing known eruptions, shots (12), and poorly constrained locations ($>\sim$5 km from the outer ETB ring) produced a final catalog of approximately 217 well-located events (Figure 2.9).

Figure 2.9 displays three primary location populations: within or near the crater ($\sim$50%), a small number (10) to the north along Fang Glacier, and on the steep and most heavily glaciated southern slopes of the volcano ($\sim$50%). During the deployment of the ETB stations, photographs were taken showing the surface and near surface conditions of the southern area (Figure 2.10). The steep south side of the mountain is generally covered in several meters of snow/firn topped by up to 2 m of cold dry snow that is typically sintered into wind slab.

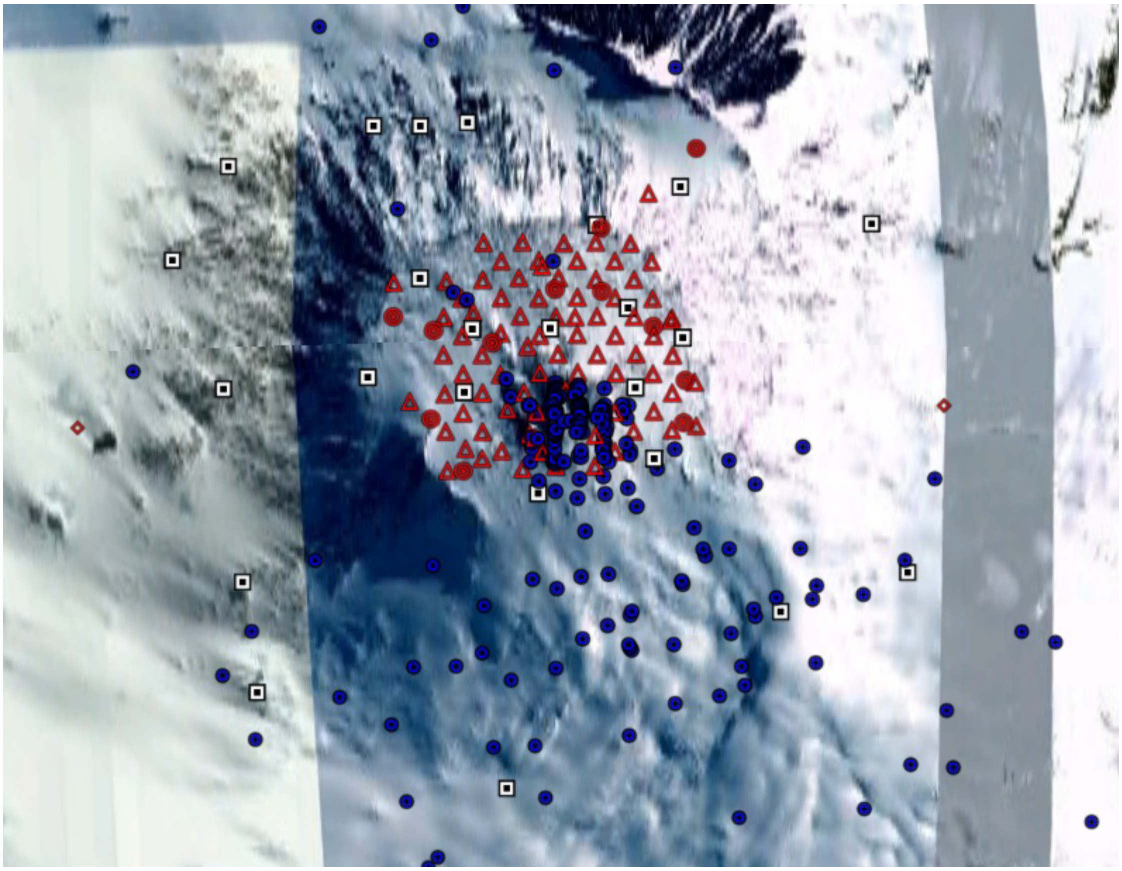

Figure 2.9: Locations of 217 relatively well-located seismic events detected between 12/09/2008 and 12/26/2008 at 50 or more stations. White squares indicate the location of the ETB stations (CMG 40T 30 s sensors), red triangles indicate the location of the ETS 3D stations (L-28 3-D 4.5 Hz sensors), red diamonds indicate the location of the ETS 2D stations (L-28 3-D 4.5 Hz sensors), red circles indicate the location of the shots detonated for tomographic imaging efforts, and blue circles indicate seismic event locations. Known lava lake eruptions, discriminated using matched filter techniques, and shots were removed from the catalog. Events located more than approximately 5 km from the ETB ring of stations were also removed because their locations are poorly constrained by the limited aperture of the station deployment.

Figure 2.10: (Left) ETB24 station (Figure 2.1; Figure 2.9; elevation 1568 m). Note typically extensive wind-slab snow coverage of the south side of the volcano and its glaciers. (Right) ETB13 site photo; note the blocky structure of the snow typical of surface conditions.

The subset of approximately 30 events located inside the crater was visually reviewed to see if the events had distinct characteristics separating them from the presumed icequakes. The goal was to determine the source mechanism, which could include (but is not limited to) rock fall, burst in the lava lake not of Strombolian type, and ice fall. The result of this investigation showed that while the events were generally smaller in amplitude and more emergent than icequakes, their envelopes and durations were similar to icequakes. Also no distinct infrasound signal was observed in association with these events. Therefore, the mechanisms for these events remain undetermined.

2.4.2 Size and Scaling Statistics of Events

We estimated the size and scaling statistics of the non-crater region events, by selecting 167 events from the catalog that met the following criteria: 1) the events were located using 50 or more stations, 2) they were not associated with active source shots or matched filter detected eruptions, and 3) they occurred outside of the crater (-77.5246 to -77.5360°S and 167.1268 to 167.1948°E).

Seismograms from the above population were examined in the short period band for the ETB network (CMG 40Ts) encompassing 30 s before to 60 s after each respective origin time. Initial analysis of the events illustrated strong site effects at some stations. In particular, when eruptions were analyzed across the network, it was seen that two stations at similar distances did not record similar amplitudes and that the "loud" stations were always the same. This illustrated the necessity for site corrections across the ETB network.

The site correction factors were computed by analyzing the median normalized maximum amplitude of 31 well-recorded Strombolian eruptions on each of the 23 ETB stations and then calculating the coefficients necessary to migrate the amplitudes to fit a 1/r curve (Figure 2.11). Amplitude decays for a 1/r curve were analyzed against decays for $1/\sqrt{r}$ in order to find the least squares minimum residual. Each of the 31 eruptions, as well as the median amplitudes, displayed an approximately 50% better fit to the 1/r decay compared to the $1/\sqrt{r}$ decay. This suggests that Strombolian eruptions excite the majority of energy into body waves. The median maximum amplitude was used so that the correction factor would be less sensitive to outliers.

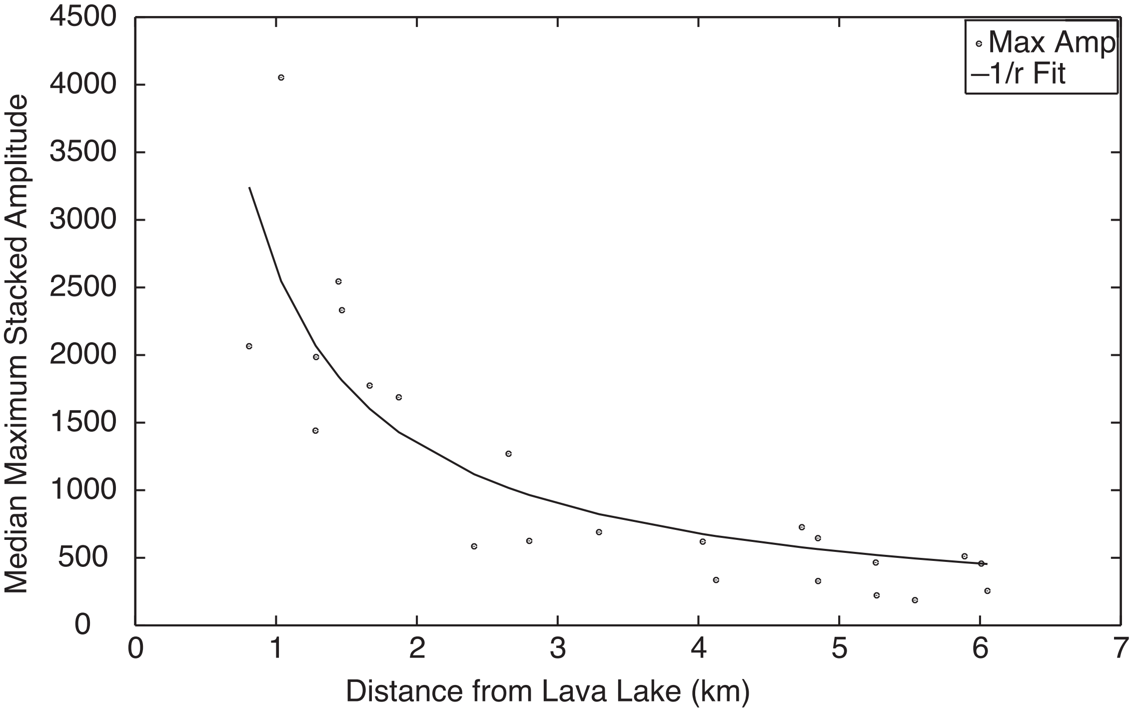

Figure 2.11: Site correction factor plot showing the normalized median maximum amplitude (black dots). The 1/r decay trends is also noted on the plot. The stations used here consist of the 23 ETB stations configured with CMG40T sensors.

Site correction factors were then individually applied to each of the stations for the 167 non-eruptive events by multiplying the sum (i.e. time integration) of the squared velocity amplitude by each station's coefficient. *Kanamori et al* [1993] performed similar methodology to estimate the energy radiated from small earthquakes recorded at short distances. Event-Station pseudoenergy estimates were then calculated by multiplying the summed squared velocity amplitude of each of the three components and multiplying by r^2, where r represents the distance from the location to the station (see Equation (2.1)). Because we are interested in relative energy, we examine this pseudo-energy proxy under the assumption that the relevant seismic velocity and density parameters necessary to convert to energy [e.g., *Kanamori et al.*, 1993], are constant across the network.

These pseudo energies, on a station-event basis, are shown as a histogram in Figure 2.12. We note that event sizes estimated using this metric show a power law distribution that is similar to volcanic and tectonic earthquake distributions. A *b*-value of approximately 2.2 was estimated by calculating a corresponding pseudo-magnitude using the formulas of *Choy and Boatwright* [1995] (Figure 2.12). This calculation did not incorporate the smallest pseudo energy values in the distribution, as the departure from power law behavior there indicates catalog incompleteness. Furthermore, the pseudo magnitudes have been normalized to the smallest magnitude (i.e. the smallest event has a pseudo magnitude of 1).

$$E_{pseudo} \sim r^2 C_r \int \sum v^2 dt \tag{2.1}$$

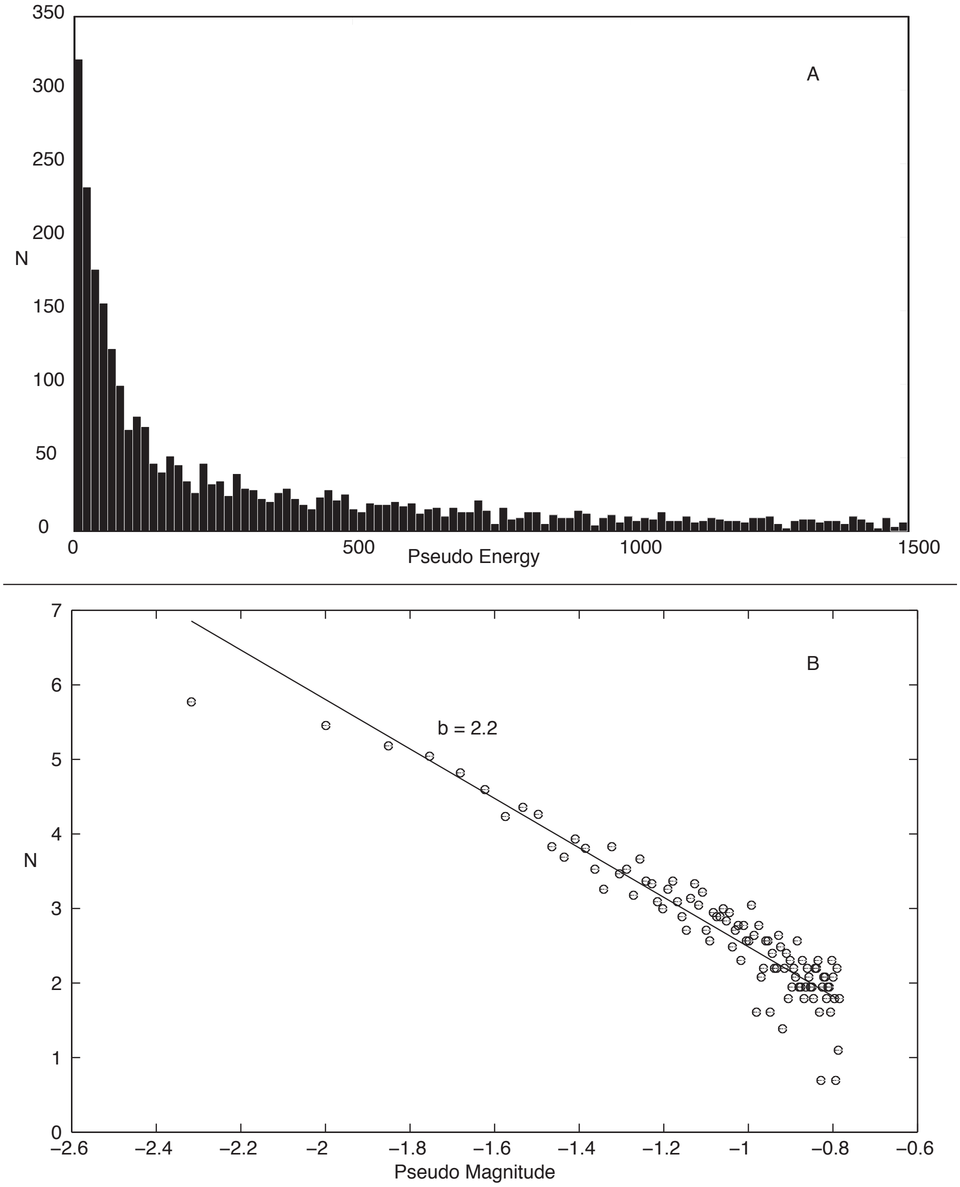

Figure 2.12: A) Station-Event pseudo energy estimates for 167 well located (recorded on 50 or more station) non-eruptive events occurring outside of the crater. The estimates are calculated from the three component data recorded on the 23 ETB sites. Note the similar distribution to earthquake energies in that smaller events are prevalent over larger events. B) B-value approximation using pseudo energy magnitude. Note that the lowest event energy was not used in the fit, since it is believed that the smallest events are not represented in the catalog.

Using the pseudo energy estimates shown in Figure 2.12, we can take our analysis one step further by estimating fault size and slip for the largest event. The approximation for shallow events from *Kanamori* [1983], allows for the conversion from energy to seismic moment (See Equation 2.2). Then we can simply plug in a rigidity for ice and solve Equation 2.3.

$$E = M_o / 2 \cdot 10^{-4} \tag{2.2}$$

$$M_o = \mu D A \tag{2.3}$$

where μ is the rigidity of ice, D is the dislocation, and A is the area.

The calculation using a rigidity of 3.5 GN/m for ice [*Wiens et al.*, 2008] and an energy estimate of 1500 J, which represents the largest of the events in Figure 2.12, produces a dislocation-area product of 0.0086 m^3. Assuming a dislocation of 1 mm, we can then estimate that the largest event was generated by a fault plane 8 m by 1.6 m slipping 1 mm. As suspected from the pseudo magnitude calculations, these are indeed very small events.

2.4.3 Seasonality and Time-of-Day Statistics

As mentioned above, we created two event catalogs: one with only events sufficiently recorded on the reference permanent network and a second with all events detected/associated, regardless of network changes. The densification and increased coverage provided by the temporary networks resulted in a much higher rate of event detection (Figure 2.13); the approximately 15,000-event difference between the two catalogs is due to the increased station coverage provided by the inclusion of 124 stations.

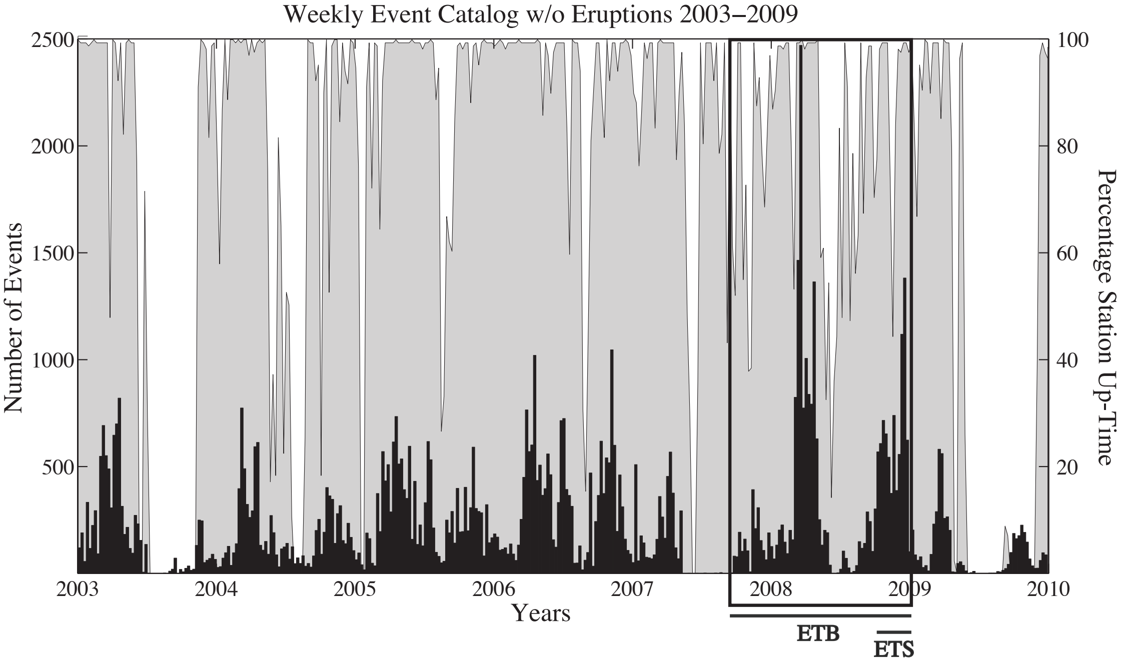

Figure 2.13: Weekly event frequency detected by 4 or more stations, and using all available stations. The vertical axis at left illustrates the number of events, and the axis at right (along with the gray background) illustrates the matched filter uptime (3 or more seismic/infrasound stations operational), which is representative of network uptime. When few or no events are recorded (i.e. many Antarctic Winters) too few stations are operational for an event association to be performed. The markedly increased rate of event detection/association during the ETB and ETS deployments (boxed region) is due to dramatically increased station coverage (Figure 2.1).

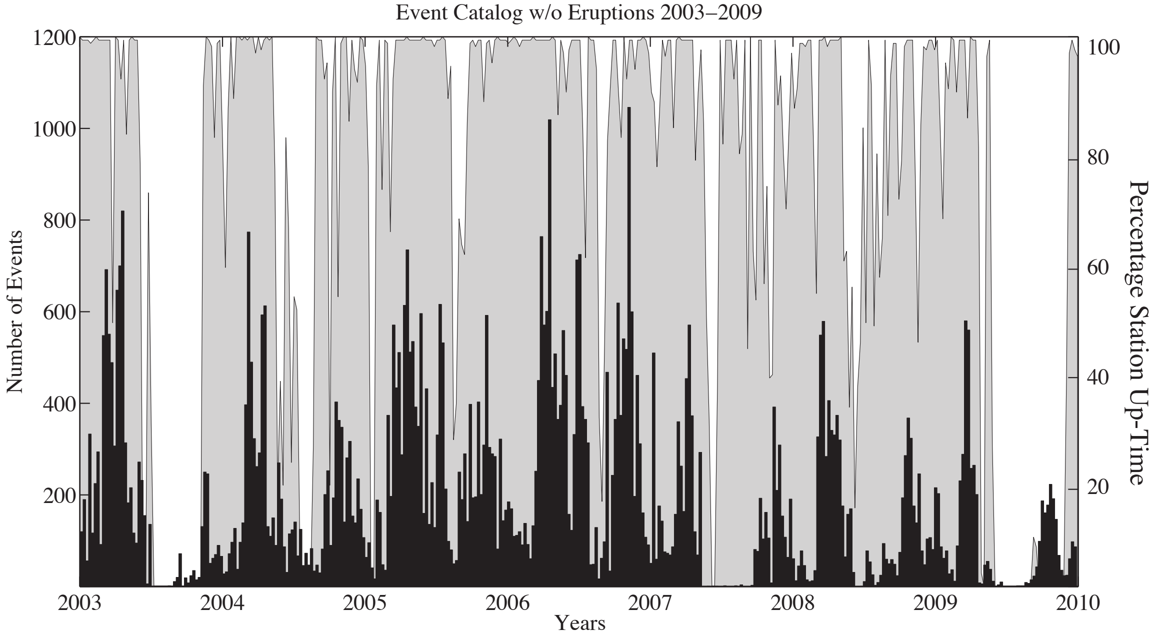

Figure 2.14: Event frequency for 69,407 events, 2003-2009, as recorded by the permanent network. This removes the bias in detection due to the temporary networks visible in Figure 2.13. The left and right vertical axes, as well as the background shading are the same as described in Figure 2.13. Note the apparent austral spring and austral fall pulses of activity.

Examining event frequency as recorded by the permanent network, with eruptions removed, we note significant correlations between event frequency and time of year (Figure 2.14), especially increased activity in the austral spring and fall. Furthermore, austral fall pulses appear to be larger than austral spring pulses.

Figure 2.14 suggests two increases in event rate each year, with the austral fall pulses, on average, being larger than the spring ones. Binning the events by month, (Figure 2.15) further demonstrates this trend, with approximately 45% of the events occurring during fall (March-May) and approximately 30% during spring (October-December). This asymmetry may not be related to natural phe-

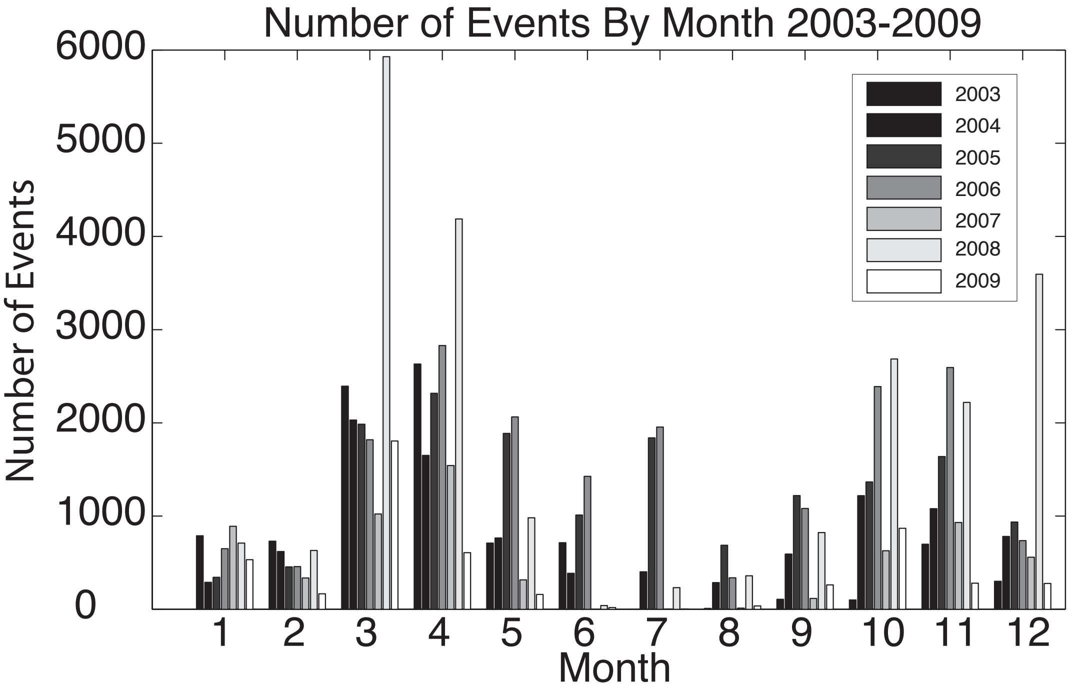

Figure 2.15: Montly event frequency for the 84,317 events shown in Figure 2.13. Approximately 45% of the events occur during March and May, and approximately 30% occur in October and December.

nomena, however, since seismic stations are less likely to be operational in the Austral winter and spring due to lack of solar charging.

To investigate further the possibility that the bi-yearly peaks in event frequency are associated with network uptime, we examine STA/LTA detections rather than the associations for a nearly 100% reliable short-period station, MAC (Figure 2.1, Figure 2.7, Figure 2.16). These results illustrate that the apparent mid-winter lull in events is, at least, significantly biased by station uptime, and that the more robust trend is for events rates to increase strongly in colder months, with a peak near the winter solstice.

Realizing that the STA/LTA detections could be made on electrical or other noise, we further investigate seasonal trends by closely examining the raw data

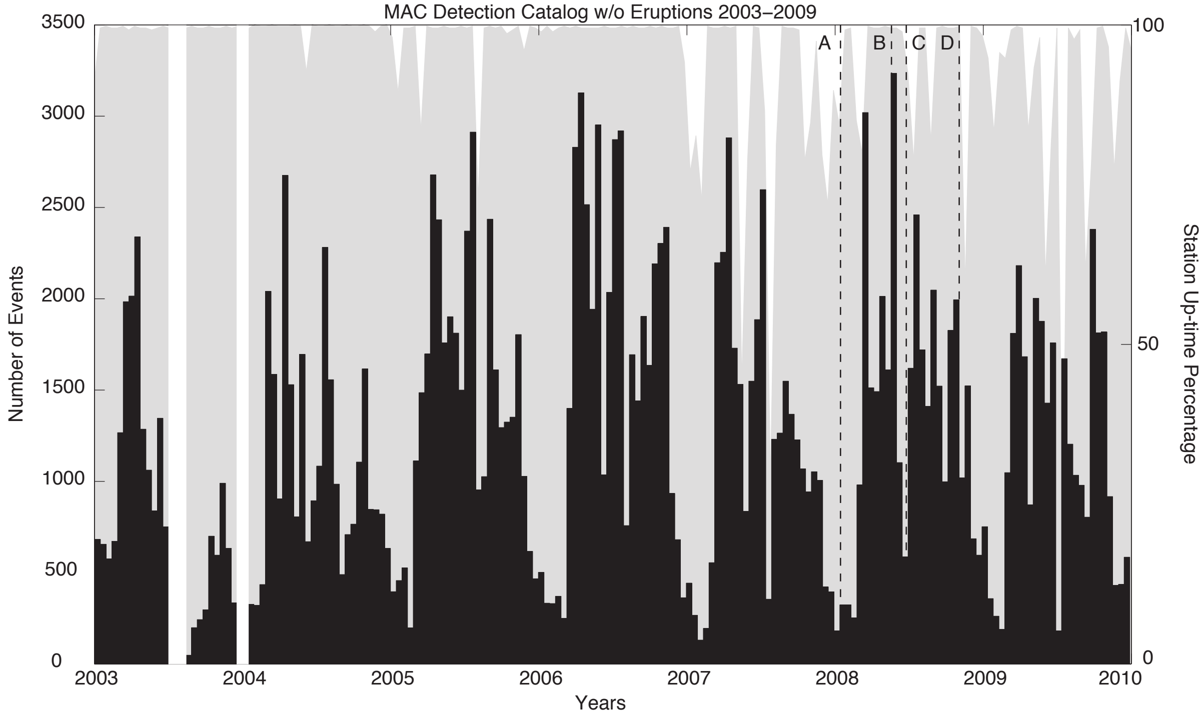

Figure 2.16: Seismic detections at station MAC binned on a bi-weekly basis. The left axis represents the number of events recorded, while the right axis and associated gray background show the station uptime. Note that the fall and spring seasonality, apparent in the event frequency plots (Figures 2.13 and 2.14), is much less apparent here. The four time periods labeled A-D refer to Figures 2.17A-D.

for several time periods in the year. Here, we show representative normalized 1-month pseudo-helicorder plots of seismic activity for January, May, June, and November of 2008 (Figure 2.17). These were chosen because they correspond to notable relative peaks or troughs in detection frequency (Figure 2.16).

For January 2008 (Figure 2.17A), 13 matched filter detected eruptions are present (larger events), leaving 645 detections possibly associated with non-eruptive seismic sources. Further examination shows little station down time except for on January 5th and January 9th (represented by a flat line) and a brief period of possible telemetry noise near the beginning of day 6. Lastly, we can see that tens of small impulsive events are occurring per day.

May 2008 (Figure 2.17B) shows 9 matched filter detected eruptions (majority at the beginning of the month) and 5,238 non-eruptive detections. Further examination shows very little station down time (several hours) and significant event swarms occur during the last half of the month.

June 2008 (Figure 2.17C) shows no Strombolian eruptions, tens of events per day, approximately 10% station down time ($\sim$3 days), and 1,520 non-eruptive detections. This plot shows several time periods with a notably increased level of background noise. This is characteristic of enhanced wind-generated short-period seismic noise from Antarctic winter storms. Increased background noise will somewhat reduce the STA/LTA detection efficiency.

November 2008 (Figure 2.17D) shows 43 Strombolian eruptions, tens of events per day, and 2,718 non-eruptive detections. Interesting, November 2008 shows significant station down time ($\sim$6 days). This is consistently seen during this month from year to year and is likely associated with intermittent late spring power system recharge.

A

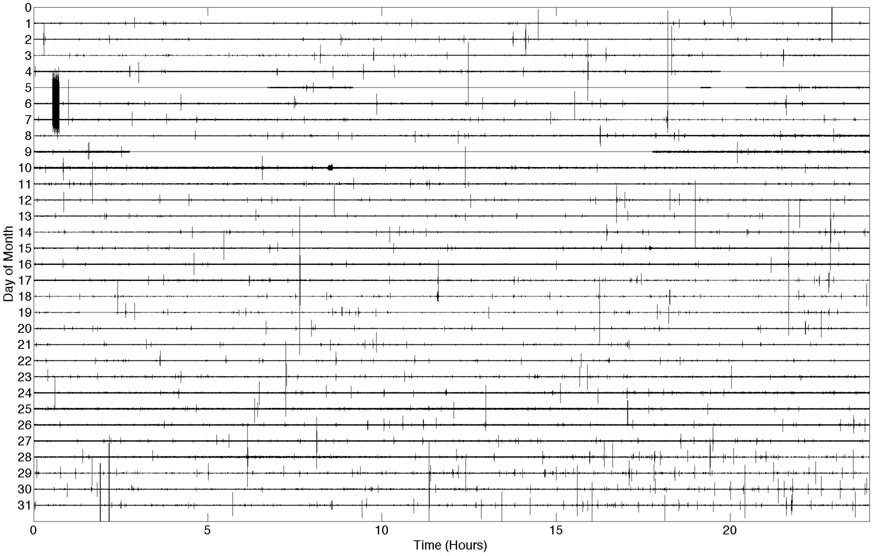
January 2008 MAC Traces
Day of Month
0
1
2
3
4
5
6
7
8
9
10
11
12
13
14
15
16
17
18
19
20
21
22
23
24
25
26
27
28
29
30
31
Time (Hours)
0
5
10
15
20

B

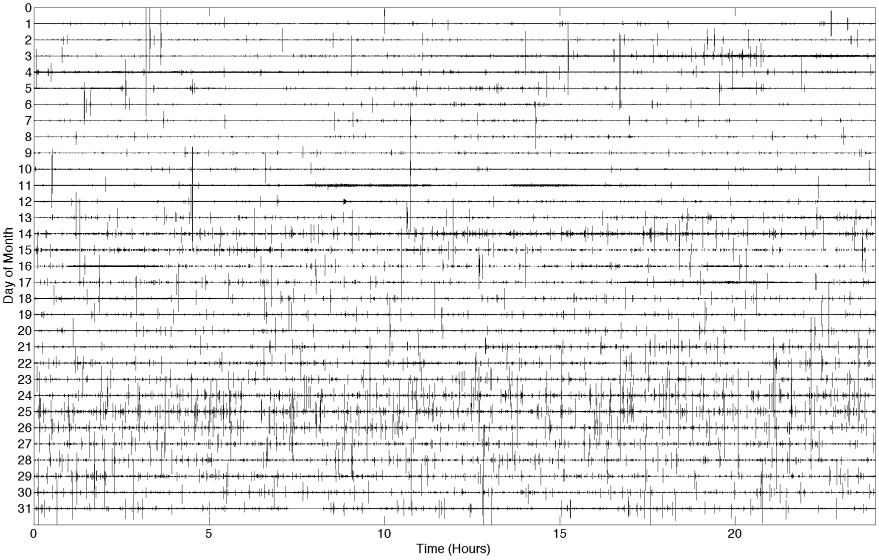
May 2008 MAC Traces
Day of Month
0
1
2
3
4
5
6
7
8
9
10
11
12
13
14
15
16
17
18
19
20
21
22
23
24
25
26
27
28
29
30
31
Time (Hours)
0
5
10
15
20

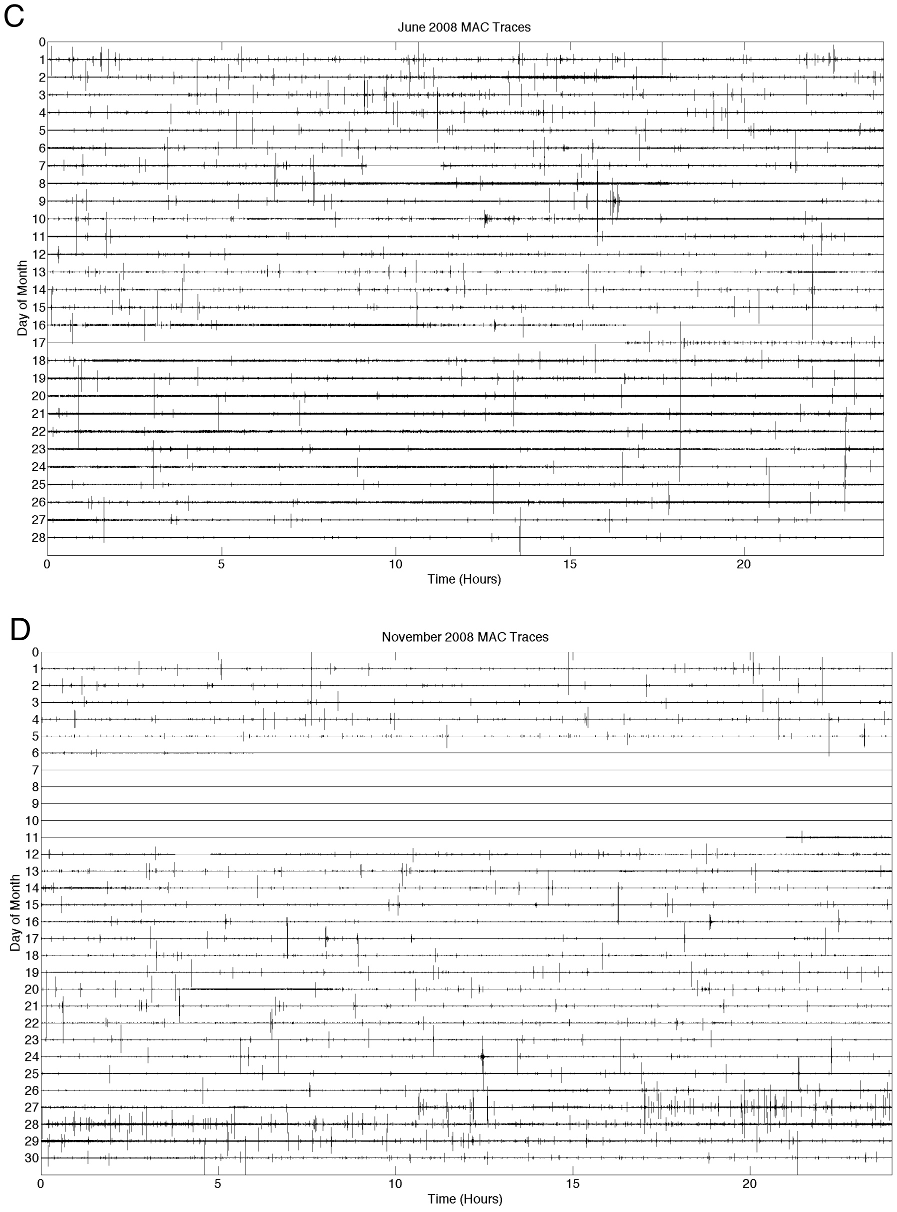

Figure 2.17: A) Pseudo-Helicorder from January 2008 showing tens of events per day, little station down time, 13 large Strombolian eruptions, and a total of 645 non-eruptive detections. The large event at the beginning of January 6th is associated with noise. B) Pseudo-Helicorder from May 2008 showing up to hundreds of events per day, very little station down time, 9 large Strombolian eruptions, and a total of 5,238 non-eruptive detections. C) Pseudo-Helicorder from June showing tens of events per day, higher background noise, minimal station down time, and a total of 1,520 non-eruptive detections. D) Pseudo-Helicorder from November showing tens of events per day, 43 large Strombolian eruptions, significant station down time, and a total of 2,718 non-eruptive detections.

The analysis at MAC is susceptible to two principal types of bias: station down time and background noise level. The first bias can be overcome by assuming relatively constant event occurrence rates and prorating the total detection frequency for each of these months. This produces adjusted event counts of: January (∼690), May (∼5,280), June (∼1,760), and November (∼3,390). The second source of bias is not as easily assessed or correctable because background noise is highly variable and its effect on STA/LTA detection will be nonlinear. Some of the lower event/detection count periods during the Antarctic winter are undoubtedly attributed to this effect, which we do not investigate here.

The strong correlation between time of year and event rate suggest a linkage with annual weather, particularly temperature, and/or insolation. Temperatures at high elevations on Erebus Volcano have been monitored since 2001 by environmental and (vault-installed) tiltmeter temperature sensors at some permanent network sites [*Aster et al.*, 2004]. Temperatures across this study period, recorded by the tiltmeter at E1S (Figure 2.1; 3700 m), range between approximately -10 and -40° Celsius with a mean absolute temperature change of approximately 6°C per month (Figure 2.18). Ambient temperature can be estimated by comparing records between the tiltmeter temperature sensor and ambient temperature data. This comparison shows that the ambient temperature is approximately 12°C colder than the outside temperature and ranges between approximately -22 and -52°C on the upper volcano.

Next we examined the relationship between event frequency and time of day for September and March, which are the months when the volcano transitions between perpetual darkness and daylight and insolation variability is at its maximum. These months also lie at the midpoint of rapid seasonal temperature

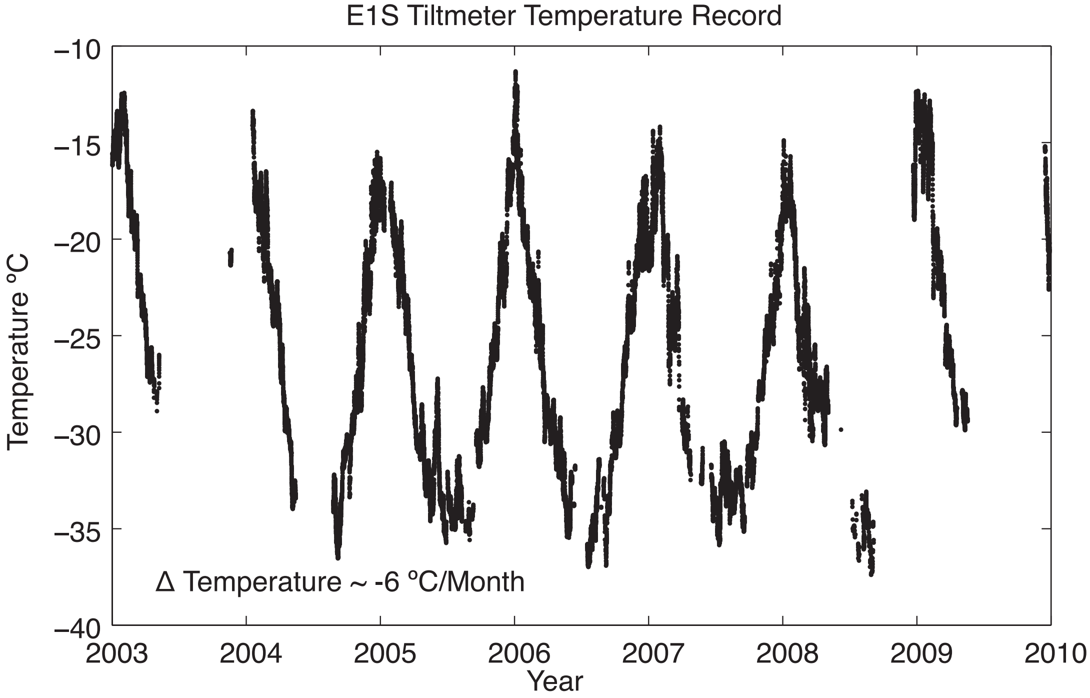

Figure 2.18: Temperature recorded by the tiltmeter temperature sensor since 2003 at station E1S. Typical temperature slopes during fall and spring are approximately 6°C/month. Note that the tiltmeter is insulated and that the true ambient temperature is colder by approximately 12°C.

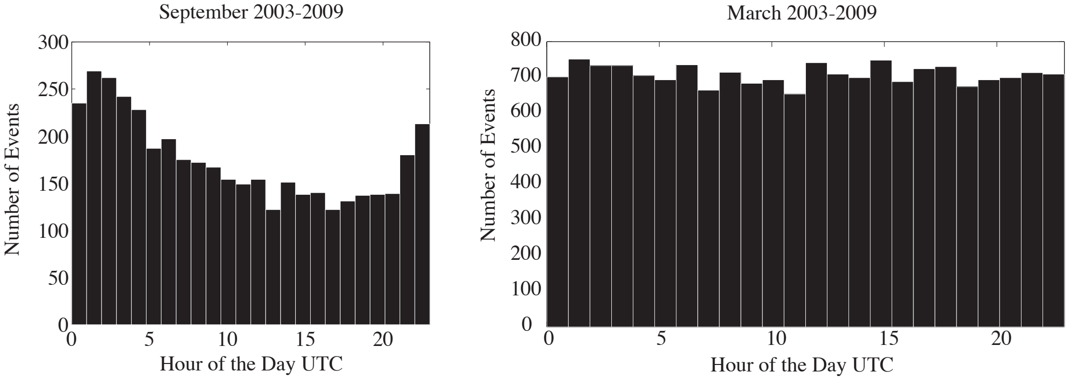

Figure 2.19: Event frequency versus UTC hour for the events (2003-2009) depicted in Figure 2.13, specifically for September and March. For September there is an event frequency peak during the hours near midnight UTC, which corresponds to the sun's most northerly position and local solar noon. No such hourly trend is observed for March.

variation on the upper volcano (Figure 14) and represent the shoulders of the annual trends noted in Figure 2.16.

The sun at the latitude of Ross Island first rises in late August and is above the horizon 24 hours a day by late October through late February, with the volcano returning to 24 hour darkness by late April. We found a correlation between event frequency and time of day in September, but no such effect for March (Figure 2.19). Specifically we note for September that almost twice as many events are occurring during the hours near midnight, compared to noon, UTC. The departure from uniform rate was tested and a p-value for this distribution (relative to a uniform distribution) was found to be is less than one part in 10,000. We note, however, that around 00:00 UTC the sun is in its most northern position and the stations are being optimally powered. Thus, sporadic uptime during the reappearance of the sun could explain this trend.

Examination of station up time during September is thus crucial for ruling out an operational time and association bias. Figure 2.20 illustrates the number of hour-long files recorded during a given hour in the September months and the years that the station was operational (titles). By this metric, if a station is operational for 2 years during the September months, then the number of files needed for 100% up time would be 60 (2 years = 60 September days). Review of Figure 2.20 shows the same general shape for many stations as the event frequency plot in Figure 2.19, showing that there is indeed a strong station operational time bias during the month of September for all years.

The essentially uniform distribution of events with time of day in March, compared with September, is reflected in a corresponding lack of station biasing. Unfortunately, the apparent increased frequency in March compared to September is difficult to quantify because of the operational time bias. To better quantify this, we return to Figure 2.16 and present the number of detections per month for station MAC in Table 2.2.

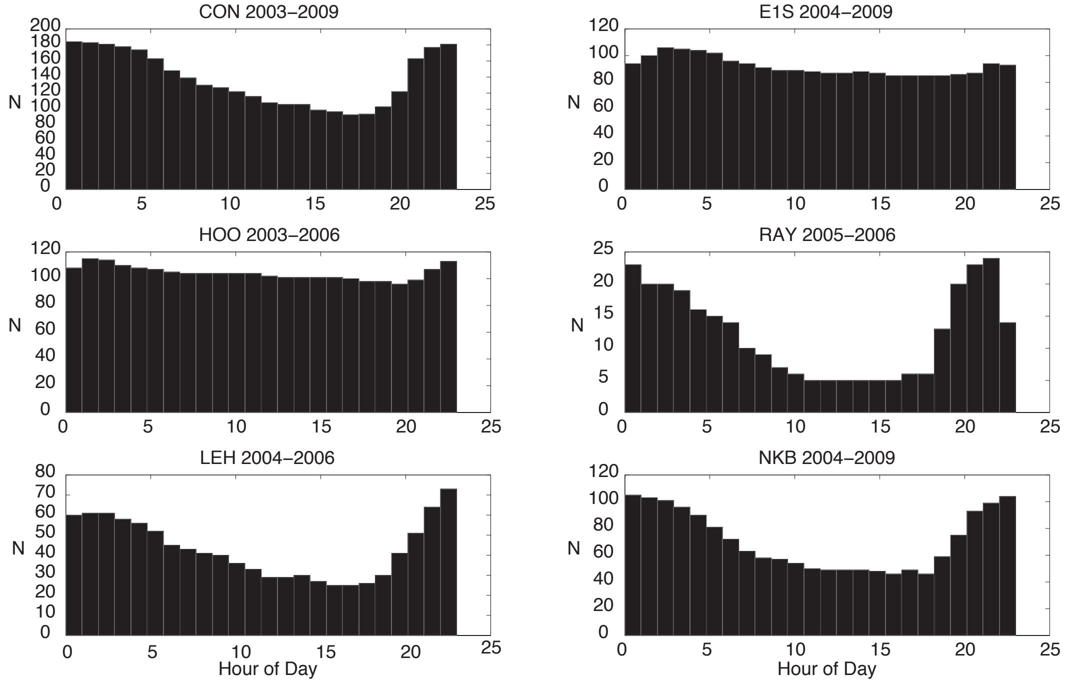

Figure 2.20: September broadband station operational times for the years available during this study. The left axis represents the number of hour-long files recorded during a given hour. Plot titles illustrate the years during which the station was operational during the month of September. For instance NKB was operational for 6 years and you would therefore expect N=180 for complete operational time. All stations, with the exception of RAY (which was destroyed in 2007 by an eruption), were generally operational throughout this study's time frame (2003-2009). For the month of September, most of the stations, however, show significantly fewer operational hours surrounding 12 UTC. This indicates that the event frequency trend in Figure 2.19 is very likely an operational network bias.

Table 2.2: MAC Detection Statistics 2003-2009

Season	Month	No. Detections	Monthly %	Seasonal %
Summer	December	3144	5.7%	13.6%
	January	2514	4.6%	
	February	1817	3.3%	
Fall	March	7818	14.2%	41.6%
	April	9545	17.4%	
	May	5543	10.1%	
Winter	June	3110	5.7%	15.1%
	July	3762	6.8%	
	August	1458	2.7%	
Spring	September	3077	5.6%	29.6%
	October	6790	12.3%	
	November	6423	11.7%	

2.5 Discussion

The results from Table 2.2, along with Figure 2.16, show that a significant number of events occur during the colder months. The lull during the winter may or may not be significant, but is certainly exacerbated by a decrease in midwinter power to the seismic stations and increased seismic noise. We show, however, that increased event rates are associated with colder temperatures and with seasonal periods of rapid mean temperature change (Figure 2.18). This suggests a cold and temperature transient-driven triggering mechanism for many of the detected events. The summer months represent both the greatest average station uptime and generally lower noise levels, so the seasonal decrease in events is notable.

Given the events' geographic locations, their strong attenuation characteristics, and demonstrated seasonality, we suggest that most of the events in our catalogs are icequakes generated in very shallow parts of the Erebus glacial system. To assess the physical plausibility of temperature forcing on the glacial system, we estimated the depth range over which such a process would occur. Assuming a thermal diffusivity (κ) of 39 m^2/y [*Hanson et al.*, 1987] for ice and an angular frequency (ω) equal to 2π, the thermal skin depth for an annual period is calculated to be approximately 3.5 m (See Equation (2.4). Thus, if temperature forcing is indeed responsible, these events occur at very shallow depths. Given observed snow and ice conditions on the Fang glacier and the southern part of the volcano (Figure 2.10), this depth would encompass a range of materials from wind-slab snow to exposed glacial ice, referred to as blue ice. The possible event lull during midwinter, is intriguing in this context because it implies that the process is driven by both low temperatures (that would increase brittle behavior) and by thermal cycling, which would induce the necessary time and depth-dependent strains. A model of thermal cycling-induced seismicity further suggests that the associated failure scenario is one of abrupt mode-1 crack formation or closure in firn or ice.

$$d_\omega = \sqrt{\frac{2\kappa}{\omega}} \tag{2.4}$$

2.6 Conclusions

Event locations, high-frequency content and rapid attenuation, and pronounced seasonality all suggest that these non-eruptive events are associated with shallow sources in the higher elevation portions of the Erebus glacial system, rather than arising from glacial-ocean interactions [*Wolf and Davies*, 1986; *Qamar*, 1988; *O'Neel et al.*, 2007] or basal sliding. We suggest that we are largely observing mode 1 opening or closing events, occurring at depths of up to several meters [*Neave and Savage* 1970, *Walter* 2009]. The general geographic association of some events to heavily crevassed regions (Figure 2.9) on the south side of the volcano, supports a shallow crevassing mechanism.

We have quantified a strong annual periodicity of seismicity that is coincident with colder temperatures in that approximately 86% of these events occur during the Antarctic fall, winter, and spring. This percentage would likely be higher if stations were operational the entire time period and if background noise was not higher in the winter months. A less-well resolved lull in seismicity around mid-winter is intriguing, and suggests that cold temperatures and seasonal thermal cycling are both drivers for enhancing event occurrence. Conversely, a well-resolved decrease in events during the well-monitored summer months suggests that summer temperatures are sufficiently warm to suppress this seismogenic process, and explains why this effect has not been noted previously on other, warmer volcanoes. It is difficult to estimate at what temperature the transition between ductile and brittle behavior occurs due to the varying elevations and locations of these events, since these factors control the local ambient temperatures. We can, however, state that near the summit of Erebus volcano, the transition likely occurs between -32°C and -37°C (ambient air temperature) since these temperatures are observed just before and after the summer months. More extensive temperature monitoring on the summit and the southern slope would be necessary to confirm the details of this transition temperature.

Acknowledgments

We thank UNAVCO and the IRIS PASSCAL Instrument Center at New Mexico Tech for facility support and field assistance on Mount Erebus. Portable seismic instruments were provided by the Incorporated Research Institutions for

Seismology (IRIS) through the PASSCAL Instrument Center at New Mexico Tech. Data collected will be available through the IRIS Data Management Center. The facilities of the IRIS Consortium are supported by the National Science Foundation under Cooperative Agreement EAR-0552316, the NSF Office of Polar Programs and the DOE National Nuclear Security Administration. We thank the many Raytheon Polar Services Company individuals and groups at McMurdo who made this field effort possible. This research was supported by NSF Awards OPP-9814291, OPP-0116577, OPP-0229305, and ANT-0538414 and by New Mexico Tech Research and Economic Development.

References

Allstadt, K., W. A. Thelen, S. D. Malone, J. E. Vidale, S. A. DeAngelis, and S. C. Moran. Shallow repeating seismic events under an alpine glacier at Mount Washington, manuscript in preparation, 2012.

Anandakrishnan, S., D. Blankenship, R. Alley, and P. Stoffa (1998), Influence of subglacial geology on the position of a West Antarctic ice stream from seismic observations, *Nature, 394*, pp. 62-65, doi:10.1038/27889.

Anandakrishnan, S. and J. P. Winberry (2004), Antarctic subglacial sedimentary layer thickness from receiver function analysis, *Global and Planetary Change, 42* (1-4), pp. 167-176, doi:10.1016/j.gloplacha.2003.10.005.

Anandakrishnan, S., and C. R. Bentley (1993), Microearthquakes beneath ice streams B and C, West Antarctica: observations and implications, *J. Glaciology, 39* (133), pp. 455-462.

Aster, R., S. Mah, P. Kyle, W. McIntosh, N. Dunbar, J. Johnson, M. Ruiz, and S. McNamara (2003), Very long period oscillations of Mount Erebus Volcano, *J. Geophys. Res., 108* (B11), 2522, doi:10.1029/2002JB002101.

Aster, R., et al. (2004), Real-time data received from Mount Erebus Volcano, Antarctica, *Eos Trans. AGU, 85* (10), 97, doi:10.1029/2004EO100001.

Aster, R., D. Zandomeneghi, S. Mah, S. McNamara, D. B. Henderson, H. Knox, and K. Jones (2008), Moment tensor inversion of very long period seismic signals from Strombolian eruptions of Erebus Volcano, *J. Volcanol. Geotherm. Res., 177* (3), pp. 635-647, doi:10.1016/j.jvolgeores.2008.08.013.

Bassis, J., H. Fricker, R. Coleman, Y. Bock, J. Behrens, D. Darnell, M. Okal, and B. Minster (2007), Seismicity and deformation associated with ice-shelf rift propagation, *J. Glaciology, 53* (183), pp. 523-536.

Bindschadler, R. A., M. A. King, R. B. Alley, S. Anandakrishnan, and L. Padman (2003), Tidally controlled stick-slip discharge of a West Antarctic Ice Stream, *Science 301*, pp. 1087-1089, doi:10.1126/science.1087231.

Caldwell, D., and P. R. Kyle (1994), Mineralogy and geochemistry of ejecta erupted from Mount Erebus, Antarctica between 1972 and 1986, in *Volcanological and Environmental Studies of Mount Erebus, Antarctica, Antarct. Res. Ser.*, vol. 66, edited by P. Kyle, pp. 147-162, AGU, Washington, D. C.

Chaput, J., R. Aster, and P. Kyle (2010), Noise tomography and Green's function estimates on Erebus Volcano, Antarctica, *Seism. Res. Lett., 81* (2).

Choy, G. L., and J. L. Boatwright (1995), Global patterns of radiated seismic energy and apparent stress, *J. Geophys. Res., 100* (B9), pp. 18,205-18,228, doi:10.1029/95JB01969.

Ekstrom, G., M. Nettles, and G. Abers (2003), Glacial Earthquakes, *Science 302*, pp. 622-624, doi:10.1126/science.1088057.

Ekstrom, G., M. Nettles, V. Tsai (2006), Seasonality and Increasing Frequency of Greenland Glacial Earthquakes, *Science 311*, pp. 1756-1758, doi:10.1126/science.1122112.

Gerst, A. (2010), The First Second of a Strombolian Volcanic Eruption, Dissertation (Doctorate in Natural Sciences), Institute of Geophysics, University of Hamburg, Germany.

Giggenbach, W., P. Kyle, and G. Lyon (1973), Present volcanic activity on Mt. Erebus, Ross Island, Antarctica, *Geology, 1*, pp. 135-136.

Hanson, B., and R. E. Dickinson (1987), A transient temperature solution for borehole model testing, *J. Glaciology, 33* (114), pp. 140-148.

Johnson, J. B., R. C. Aster, K. R. Jones, P. R. Kyle, and W. C. McIntosh (2008), Acoustic source characterization of impulsive Strombolian eruptions from the Mount Erebus lava lake, *J. Volcanol. Geotherm. Res. 177* (3), pp. 673-686, doi:10.1016/j.jvolgeores.2008.06.028.

Kaminuma, K. (1994), The Seismic Activity of Mount Erebus in 1981-1990, in *Volcanological and Environmental Studies of Mount Erebus, Antarctica, Antarct. Res. Ser.*, vol. 66, edited by P. Kyle, pp. 35-50, AGU, Washington, D. C.

Kanamori, H., J. Mori, E. Hauksson, T. H. Heaton, L. K. Hutton, and L. Jones (1993), Determination of earthquake energy release and ML using TERRAscope, *Bull. Seism. Soc. Am., 83* (2), pp. 330-346.

Knox, H., J. Chaput, R. Aster, P. Kyle, and L. Jones, Mulityear timing variations between short period and very long period Strombolian eruption seismograms: evidence for upper conduit geometry changes at Erebus Volcano, Antarctica, manuscript in preparation, 2012.

Kyle, P. R., R. R. Dibble, W. F. Giggenbach, and J. Keys (1982), Volcanic activity associated with anorthoclase phonolite lava lake, Mount Erebus, Antarctica, in *Antarctic Geoscience*, edited by C. Craddock, pp. 734-745, University of Wisconsin Press, Madison.

MacAyeal, D. R., E. Okal, R. Aster, and J. Bassis (2008), Seismic and hydroacoustic tremor generated by colliding icebergs, *J. Geophys. Res., 113*, F03011, doi:10.1029/2008JF001005.

Maraj, S. (2011), Controlled Source Seismic Investigation of the Crustal Structure Beneath Erebus Volcano and Ross Island, Antarctica, M.S. Thesis, New Mexico Institute of Mining and Technology, Socorro, New Mexico.

Martin, S., R. Drucker, R. Aster, F. Davey, E. Okal, T. Scambos, and D. MacAyeal (2010), Kinematic and seismic analysis of giant tabular iceberg breakup at Cape Adare, Antarctica, *J. Geophys. Res., 115*, B06311, doi:10.1029/2009JB006700.

Neave, K., and J. Savage (1970), Icequakes on the Athabasca Glacier, em J. Geophys. Res., 75 (8), pp. 1351-1362, doi:10.1029/JB075i008p01351.

O'Neel, S., H. P. Marshall, D. E. McNamara, and W. T. Pfeffer (2007), Seismic detection and analysis of icequakes at Columbia Glacier, Alaska, *J. Geophys. Res., 112*, F03S23, doi:10.1029/2006JF000595.

Pesaresi, D. (2011), The EGU2010 SM1.3 Seismic Centers Data Acquisition session: an introduction to Antelope, EarthWorm and SeisComP, and their use around the World, *Annals of Geophysics, 54*, (1), pp. 1-7, doi:10.4401/ag-4972.

Petrovic, J. (2003), Mechanical Properties of Ice and Snow, *Journal of Materials Science, 38* (1), pp. 1-6, doi:10.1023/A:1021134128038.

Qamar, A. (1988), Calving icebergs: A source of low-frequency seismic signals from Columbia Glacier, Alaska, *J. Geophys. Res., 93* (B6), pp. 6615-6623, doi:10.1029/JB093iB06p06615.

Rowe, C. A., R. C. Aster, P. R. Kyle, J. W. Schlue, and R. R. Dibble (1998), Broadband recording of Strombolian explosions and associated very-long-period signals on Mount Erebus Volcano, Ross Island, Antarctica, *Geophys. Res. Lett. 25* (13), pp. 2297-2300, doi:10.1029/98GL01622.

Rowe, C. A., R. C. Aster, P. R. Kyle, R. R. Dibble, and J. W. Schlue (2000), Seismic and acoustic observations at Mount Erebus Volcano, Ross Island, Antarctica, 1994 -1998, *J. Volcanol. Geotherm. Res. 101* (1-2), pp. 105-128, doi:10.1016/S0377-0273(00)00170-0.

Ruiz, M. (2003), Analysis of Tremor Activity at Mt. Erebus Volcano, Antarctica, M.S. Thesis, New Mexico Institute of Mining and Technology, Socorro, New Mexico.

Schweizer, J., J. Bruce Jamieson, and M. Schneebeli (2003), Snow avalanche formation, *Rev. Geophys., 41* (4), 1016, doi:10.1029/2002RG000123.

Shearer, P. (1994), Global seismic event detection using a matched filter on long-period seismograms, *J. Geophys. Res., 99* (B7), pp. 13,713-13,725, doi:10.1029/94JB00498.

Squire, V., W. Robinson, M. Meylan, and T. Haskell (1994), Observations of flexural waves on the Erebus Glacier Tongue, McMurdo Sound, Antarctica, and nearby sea ice, *J. Glaciology, 40* (135), pp. 377-385.

St. Lawrence, W., and T. Williams (1976), Seismic Signals Associated with Avalanches, *J. Glaciology, 17* (77), pp. 521-526.

St. Lawrence, W., and C. Bradley (1977), Spontaneous Fracture Initiation in Mountain Snow-Packs, *J. Glaciology, 19* (81), pp. 411-417.

Tsai, V.C. and G. Ekstrom (2007), Analysis of Glacial Earthquakes, *J. Geophys. Res., 112*, F03S22, doi:10.1029/2006JF000596.

Tsai, V.C.; J. Rice, and M. Fahnestock (2008), Possible mechanisms for glacial earthquakes, *J. Geophys. Res., 113*, F03014, doi:10.1029/2007JF000944.

Walter, F. (2009), Seismic Activity on Gornergletscher During Gornersee Outburst Floods, Dissertation, ETH ZURICH.

Weaver, C. S., and S. D. Malone (1979), Seismic evidence for discrete glacier motion at the rock-ice interface, *J. Glaciology, 23*, pp. 171-184.

Wegler, U. (2004), Diffusion of seismic waves in a thick layer: Theory and application to Vesuvius Volcano, *J. Geophys. Res., 109*, B07303, doi:10.1029/2004JB003048.

Wiens, D. A., S. Anandakrishnan, J. P. Wineberry, and M. A. King (2008), Simultaneous teleseismic and geodetic observations of the stickslip motion of an Antarctic ice stream, *Nature, 453* (7196), pp. 770-774, doi:10.1038/nature06990.

West, M., C. Larsen, M. Truffer, S. O'Neel, and L. LeBlanc (2010), Glacier Microseismicity, *Geology, 38* (4), pp. 319-322, doi:10.1130/G30606.1.

Wolf, L. W., and J. N. Davies (1986), Glacier-generated earthquakes from Prince William Sound, Alaska, *Bull. Seism. Soc. Am., 76* (2), pp. 367-379.

Wolf, L., C. Rowe, R. Horner (1997), Periodic Seismicity near Mt. Ogden on the Alaska-British Columbia Border: A Case for Hydrologically Triggered Earthquakes, *Bull. Seism. Soc. Am., 87* (6), pp. 1473-1483.

Zandomeneghi, D., R. Aster, A. Barclay, J. Chaput, and P. Kyle (2011), Tomographic high-resolution 3D imaging of the shallow magmatic system of Erebus Volcano, Antarctica, *Eos Trans. AGU*, Fall Meet. Suppl.

APPENDIX A

CONSTRUCTION OF THE MATCHED FILTER FOR EREBUS VOLCANO, ANTARCTICA

The following outlines the details and procedures necessary to recreate the eruption database used in this study. This database represents the largest Strombolian eruption dataset compiled to date for Erebus volcano. This text will also cover how to create the Strombolian Eruption Frequency plot with Matched Filter uptime and make future recommendations for this processing.

A.1 Introduction

It is important to note that the Matched filter went through three revisions, resulting in three eruption databases. This work used the most recent one: /fs/erework/eruption_database_newest. The other two reside in /fs/eredata/Erebus/ and are named Eruptions_database and Eruptions_database_new. The two primary differences between each of these databases are: 1) the number of stations used in the template and detection process and 2) the sensitivity or weights given to the stations during the detection process. All cut matched filter detections are cut so that 2 minutes of data precedes the pick and 9 minutes of data is kept after the pick.

The first database (Eruptions_database) contains 2,245 matched filter detections from 2003 through mid-May 2009 and is considered to be lacking a number of eruptions due to the limited number of stations used. Specifically this trial did not include all of the available infrasound data. The second database (Eruptions_database_new) incorporated all of the available infrasound data and then preferentially weighted the infrasound data for detections. When this database was reviewed manually it was confirmed that this procedure led to many false detections due to infrasound dropouts and data-spikes. The database contains 5,585 matched filter detections between 2003 and end of December 2009. Finally an optimal tradeoff was found through small test sets and manual review of continuous data. The third database contains 2,987 reviewed eruptions spanning from 2003 through September 2011. Note that 2,859 of these reviewed eruptions were recorded during the time period scanned for the first database.

A.2 Creating the "Boomer" Template

The first step in the eruption database construction was to build an eruption template representing a stack of eruptions recorded across the broadband seismic and infrasound networks. This unique template by design would take advantage of waveform similarity and constant source location (i.e. move-out). This task initially required reviewing the continuous data recorded by the MEVO network and hand picking a number of eruptions. In the final version of the template, however, the following 20 eruptions from the first database (Eruptions_database) were chosen for the "Boomer" template:

These events represent the typical "Boomer" characteristics in that they are high signal to noise events (i.e loud) and that they were well recorded across the 6 broadband stations and 3 infrasound sensors. Note that one important characteristic of the database can be seen in the above list; the difference between all

```
/fs/eredata/Erebus/Eruptions_database/20060101030000_1
/fs/eredata/Erebus/Eruptions_database/20060101170000_1
/fs/eredata/Erebus/Eruptions_database/20060101200000_1
/fs/eredata/Erebus/Eruptions_database/20060101230000_1
/fs/eredata/Erebus/Eruptions_database/20060101230000_1
/fs/eredata/Erebus/Eruptions_database/20060102130000_1
/fs/eredata/Erebus/Eruptions_database/20060103070000_1
/fs/eredata/Erebus/Eruptions_database/20060103160000_1
/fs/eredata/Erebus/Eruptions_database/20060103210000_1
/fs/eredata/Erebus/Eruptions_database/20060104060000_1
/fs/eredata/Erebus/Eruptions_database/20060104100000_1
/fs/eredata/Erebus/Eruptions_database/20060104150000_1
/fs/eredata/Erebus/Eruptions_database/20060105070000_1
/fs/eredata/Erebus/Eruptions_database/20060105150000_1
/fs/eredata/Erebus/Eruptions_database/20060105160000_1
/fs/eredata/Erebus/Eruptions_database/20060105200000_1
/fs/eredata/Erebus/Eruptions_database/20060106160000_1
/fs/eredata/Erebus/Eruptions_database/20060106160000_2
/fs/eredata/Erebus/Eruptions_database/20060106220000_1
/fs/eredata/Erebus/Eruptions_database/20060107050000_1
```

of the other days and January 6, 2006 is that two events occurred during hour 16. These files are represented by 20060106160000_1 and 20060106160000_2. This is further represented by the detection times for these events shown in Table A.1. Note that in Table A.1 the first four columns represent the start of the file scanned, not the pick time. The pick time is represented in the last column as the number of seconds after the start of the file.

Once the events were chosen for the "Boomer" template, their vertical components were loaded into matlab as sac files, detrended, bandpass filtered between 2 and 6 Hz using a two pole Butterworth filter, and unit normalized. Next the relative time lags were calculated for each station with reference to E1S.BHZ.ER, all traces were shifted to account for moveout, and then stacked on a per station basis. These stacks were then windowed to 5 seconds before the pick and 40 seconds after the pick and saved into the boomer1.mat file that re-

Table A.1: Matched Filter Detection Times for the Boomer Template

Year	Day of Year	Hour	Minute	Second	Pick (seconds from start)
2006	1	5	59	54	1.977676e+03
2006	1	16	59	43	2.813369e+03
2006	1	19	59	56	9.935013e+02
2006	1	22	59	52	2.753716e+03
2006	2	6	59	53	1.107089e+03
2006	2	12	59	54	4.626708e+02
2006	3	6	59	41	9.682850e+02
2006	3	15	0	0	7.215169e+02
2006	3	20	59	37	1.587738e+03
2006	4	5	59	59	2.535795e+03
2006	4	9	59	58	4.786847e+02
2006	4	14	59	54	4.374908e+02
2006	5	6	59	57	8.659500e+02
2006	5	14	59	52	6.147487e+02
2006	5	15	59	40	6.378274e+02
2006	5	19	59	37	1.145988e+03
2006	6	15	59	50	4.398089e+02
2006	6	15	59	50	1.293929e+03
2006	6	21	59	42	2.385445e+03
2006	7	4	59	53	7.586142e+02

sides in /fs/erework/matlab. A script named boomer_lag.m performs this entire process. Figure A.1 illustrates the stacked, unit normalized, bandpass filtered, and lag adjusted template used for the detection process.

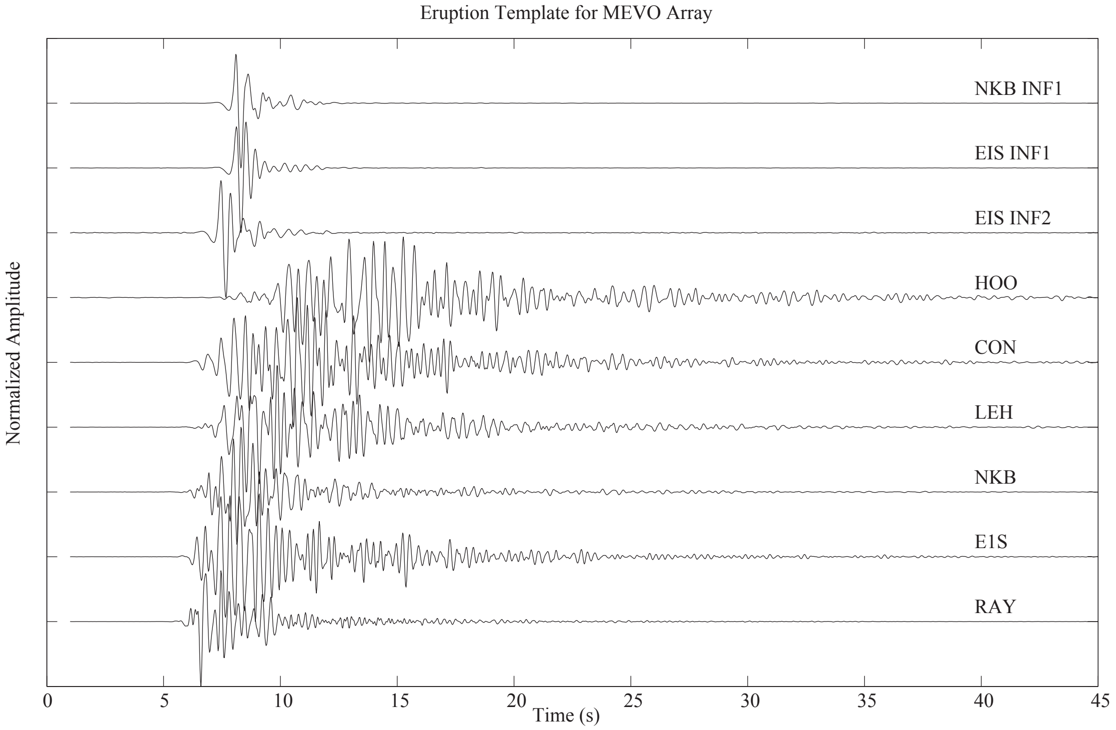

Figure A.1: Matched Filter Template used for scanning continuous data for event detection from 2003 through 2011. INF denotes an infrasound sensor. All of these seismic signals have been self-scaled and zero-phase filtered between 1 and 8 Hz to optimize SP band signal-to-noise.

A.3 Transferring and Prepping the Continuous Data

The continuous data, depending on the year, exists in a variety of formats (SAC or AH), compression (zipped or unzipped), and endianness (big or little). This creates a variety of problems for the matched filter detection process and thus requires careful attention. The first two inconsistencies can be accounted for during the transfer process of the continuous data, which is necessary because of network and server restrictions. A shell script called Trans_Match_Filt2.sh (/fs/erework/matlab) accounts for the file format and compression issues by allowing the user the opportunity to implement the ah2sac and bunzip2 commands at the bottom of the script. The user can decide whether or not to utilize these commands by reviewing the desired continuous data in the archive (/fs/eredata/Erebus/Erebus_YY/Archive). Note here that the "YY" in the path should be replaced with the last two digits of the year in question. Review of the continuous data is performed easily by reviewing the file names (.zip vs. .ER) and then utilizing the PQL package created by PASSCAL and checking the header information for format. The last inconsistency (endianness) is accounted for in the actual matched filter detection script, by testing both the load_sac and load_sac_I functions. A simple test for determining if the correct load function was used is to check the header information and confirm that "resp0" is equal to -12345.

A.4 Scanning the Transferred Continuous Data

Once the continuous data is transferred and appropriately converted to unzipped sac files, a list of directories must be created for input into the match filter detection code. Note that the user must check the nobackup directory to ensure that only the files to be scanned are present or the below command must be altered such that only the desired files are listed. Since the Trans_Match_Filt2.sh script transfers the data into the /fs/erework/nobackup directory, generation of this list can be achieved by using a version of the following command:

```
ls d /fs/erework/nobackup/2* >> /fs/erework/matlab/my_textfile.txt.
```

Now that the appropriate list of files to be scanned has been created, the user must edit the input for the matched filter code. Specifically, the user must change the following sections of the match_filter_2010_on.m file:

```
!cat my_textfile.txt | wc -l > countt2.txt;
!cp my_textfile.txt LISTS2.txt
!cat my_textfile.txt | wc -l > lecS2.num;

[aa] = textread('/fs/erework/matlab/my_textfile.txt','%s');
```

These two sections are marked by commented headers stating “Change this one“ and represent the two locations that designate the reading of the list previously created.

The next item that the user must address is the generation of the new pick file, which will record the detections in the same format as those seen in Table A.1. The new pick file is designated in the following command, which is also designated with commented headers stating “Change this one”:

```
fid14 = fopen('picks_my_textfile.txt','a');
```

Note that the list (my_textfile.txt) and the picks file (picks_my_textfile) can be of any format. It is, however, recommended that the two lists share the same base name (i.e. 2009.txt and picks_2009.txt). This will ensure that lists can be tied to each other and progressive scanning can be easily documented.

Once the match_filter_2010_on.m file is edited, then the user can simply run the code. The user should note that the matlab command window will show the progress of the program by displaying the file currently being processed and the total number of files to be processed (i.e. 1 of 1000). Once the program has finished without error, the picks file designated by the user will be created and the events can be cut and saved into the newest eruptions database (/fs/erework/eruption_database_newest).

A.5 Cutting the Events

Once the detections have been made and appropriately written to the picks file, the user can use the Pick_all function to cut the events. The Pick_all function resides in the /fs/erework/matlab directory as an m file. This process is achieved by simply entering the following command into the matlab command window:

```
Pick_all(‘‘picks_my_textfile.txt‘‘)
```

Once this function completes its process, the user can view the newly cut eruption(s) in the /fs/erework/eruption_database_newest directory.

A.6 Making the Eruption Frequency Plots with Matched Filter Uptime

Now that the user has generated either a new or updated database, it is insightful to create an eruption frequency plot with the matched filter uptime. In the script discussed here the eruption frequency is displayed as a histogram on an approximately weekly basis. The matched filter uptime is strictly defined as times when at least 3 stations from the nine (2003-2007) or eight (2007-present) stations scanned are recording. This designation is important since it is one of the requirements for matched filter detections. In the instance that the matched filter is not able to meet this requirement, an eruption may occur that goes undetected.

The first step in this process is to generate a list of the directory names in the eruptions database. This can be achieved by running the following command:

```
ls -d /fs/erework/eruption_database_newest/2* >&
 /fs/erework/matlab/Eruption_Frequency.txt
```

The user should make sure to remove or rename the old Eruption_Frequency.txt file before running this command.

The second step in this process is to run a shell script named Time_plot.sh, which is located in the /fs/erework/matlab directory. This script scans the continuous archive from 2003 forward for each station used in the detection process and creates a list of when the files exist (i.e. HK_E1S_upfile.txt). This list is comprised of the year, month, day, hour, and station name for each station. The plotting script discussed below uses the nine lists created by the script.

Once these two sets of text files are created, the user can run the script used to make this plot. The script is located in the /fs/erework/matlab directory and is named Eruption_Freq1.m. An important note about this process is that matlab is presently unable to export the resulting figure. Therefore, the user must generate the eruption frequency histogram and the matched filter plots separately. This can be achieved by running the program, clearing the figures, and then running the "hist" and "jbfill" commands separately. Instructions for running the "jbfill" command are given in the beginning comments of the script.

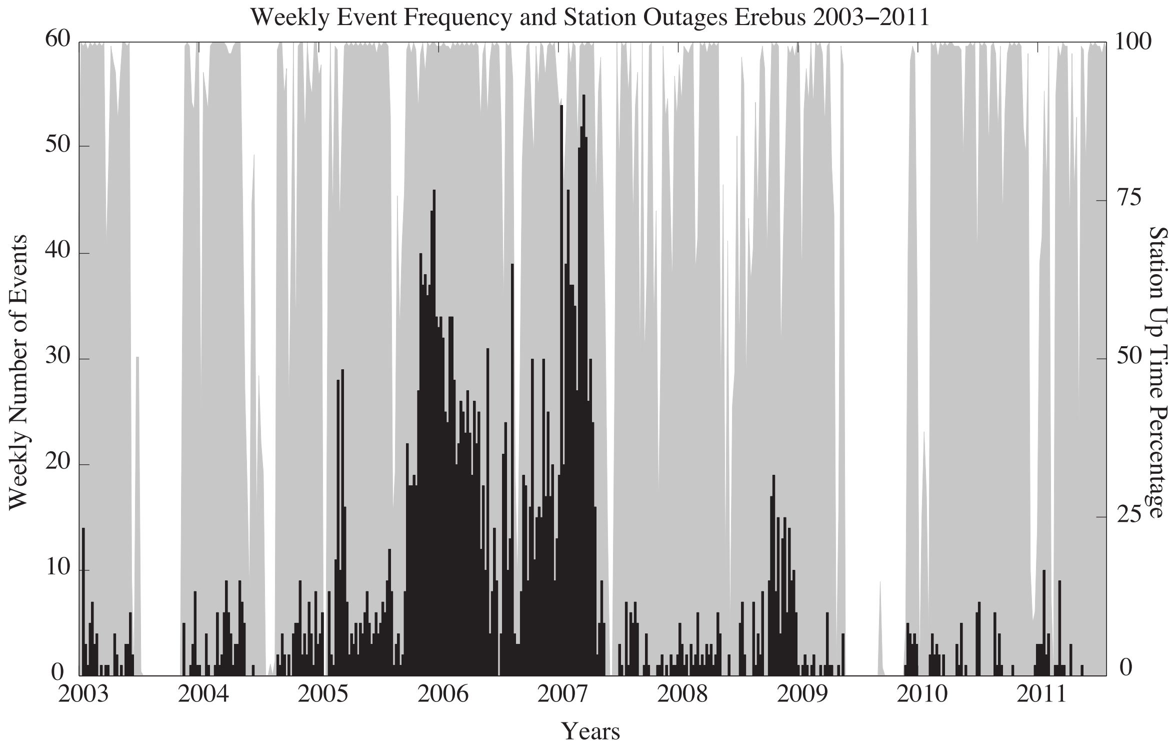

Figure A.2: Histogram of weekly numbers of the 2879 eruptions detected using the matched filter as described in the text. Gray shaded time intervals indicate periods when more than 3 or more stations were continuously operational, with uptime percentage on a weekly basis noted on scale at left. Network gaps characteristically correspond with austral winter periods when non solar power supplies were insufficient to maintain operation.

Once the two plots are exported from matlab as .eps files, they can be opened in Adobe Illustrator. The first step in this process is to shade the matched filter uptime by utilizing the live paint tool. Once this is accomplished, the shading can be overlaid on the histogram plot. The resulting image is displayed in Figure A.2 .

A.7 Recommendations for Future Work

The easiest way to process the continuous record presently is to run the matched filter on a month-to-month or yearly basis, since this minimizes the problems encountered with transferring and converting the data. Unfortunately, this does not allow for review of real time results and updated plots for the website. A minimal amount of work would be required to rectify this and create updated plots on a daily basis.

This work would include creating a wrapper script that would query the clock on a given computer and run the scripts discussed here. Presumably the wrapper script would not call on the shell scripts, but would rather incorporate many of the commands found there. Furthermore, it would require that all of the matlab scripts be edited so that they are functions with inputs.

Since MACZ has been shown to be a very reliable station, it is recommended that the matched filter be augmented to use this short period station for detections. Some consideration will have to be made since a detection on MACZ will not contain the VLP information that the broadband sensors record. In the absence of a VLP, the seismogram recorded from a large icequake and a lava lake eruption can be highly similar, especially if recorded at larger distances. Also, since MACZ is much further from the crater than the other stations utilized, some testing will need to be conducted to see if correlation and move out criteria is sufficient. The easiest way to test this is to use some events already detected and test the accuracy based on station constellations. These efforts will likely have great rewards since this station is powered much of the time.

APPENDIX B

ANTELOPE DATABASE DETAILS

During the course of submitting the data from the ETB and ETS temporary deployments, it was decided that a comprehensive Antelope Database should be constructed for all available MEVO data through the end of 2009. This effort eventually allowed for the analysis required for the second chapter of this dissertation. This process began with the creation of the individual Antelope databases for the ETB and ETS deployments. These databases and their dataless seed volumes were submitted to the IRIS DMC under the ZW and Y4 network codes respectively. The MEVO network code is ER.

Once the data and accompanying metadata was found to be accurate, the continuous data was converted to miniseed and added to the database. Note that many of the serial numbers for the MEVO stations were not available and therefore, were faked into the system. This does not make the Antelope database or its subsequent processing invalid. It does, however, prevent the generation of the dataless seed volume from this particular Antelope Database. The Antelope Database was generally processed in these steps: 1) Construction of the STA/LTA detector (dbdetect.pf), 2) Execution of detection process on a yearly basis unless scan was broken (see comment below), 3) Construction of travel time grid (ttgrid.pf), 4) Execution of association process (dbgrassoc.pf and other necessary parameter files). These files represent the largest event database computed for Erebus Volcano to date.

At present, two copies of the Antelope Database exist. One is located on a portable 1 TB hard drive named “Hunter“. The other copy, which is the original and is presently in good working order, is located on Churrasco’s hard drive in the NMT mac lab (/Volumes/Macintosh HD 2/scratch/hunter) . Note that the copy of Antelope has been altered on Churrasco to include the Erebus seismic velocity model so that more accurate processing could be accomplished. The database consists of a variety of files describing everything from network codes to associated events. Those files with no extension contain information that ties the detections and the associations back to the unaltered original Antelope Database, which is comprised of files with “Erebus“ followed by and extension (i.e. Erebus.wfdisc). Those files that contain a two digit number and an extension (i.e. Erebus_01.arrival) are files generated through some type of processing whether it be detections or associations. In this subset of files, there are files with the word “Fix“ in them. These files designate that the entire year was unable to be continuously processed. When the event detection sequence was broken, the detection scans were started on the hour immediately following the break. For instance, if the scan stopped on 2008:311:03:00:00, then the next scan was started on 2008:311:04:00:00. If this was the first break, then the first set of detections would be designated as Erebus_08.detections and the second set would be designated as Erebus_08_Fix1.detections or something similar. Also, in this subset of files there are files with “PN“ in them; these files only contain the MEVO permanent network stations in their detection/association scans.

As a final note, once the Antelope Database was constructed and the Matched Filter was executed for the time periods covering the temporary deployments (ETB and ETS), the eruptions were cut from the Antelope Database in SAC format for all available stations and all available channels. In total there are 243 eruptions that were flagged during the temporary deployments. These files are also stored on Churrasco's hard drive in the NMT mac lab under /Volumes/Macintosh HD 2/scratch/hunter.

APPENDIX C

MEVO STATION METADATA

During the process of this dissertation, the MEVO Station Metadata was compiled and corrected as needed. The values listed in the three tables/figures below are believed to be the most accurate available. Many of these values were used in the processing of the data mentioned in the two chapters above. Other forms of these documents exist within the MEVO group. These are merely included here for completeness purposes and future referencing.

NETWORK	STATION	CHANNELS	LATITUDE	LONGITUDE	ELEVATION	START TIME	END TIME	INSTRUMENT	AZIMUTH	DIP	SAMPLE RATE	UNITS
ER	NKB	BHZ	-77.521976	167.147465	3626.95	1/1/02	12/31/2599	Guralp CMG-40T Seismometer	0	-90	40	M
		BH1	-77.521976	167.147465	3626.95	1/1/02	12/31/2599	Guralp CMG-40T Seismometer	142	0	40	M
		BH2	-77.521976	167.147465	3626.95	1/1/02	12/31/2599	Guralp CMG-40T Seismometer	232	0	40	M
		IS1	-77.521989	167.147403	3627.01	12/1/06	12/31/2599	Honeywell Pressure Transducer	NA	NA	40	Counts
		IS2	-77.526073	167.155853	3774.12	1/1/06	12/31/2599	Honeywell Pressure Transducer	NA	NA	40	Counts
		IS1	-77.521989	167.147403	3627.01	1/1/03	11/31/2006	Electric Condenser	NA	NA	40	Counts
ER	E1S	BHZ	-77.530420	167.139711	3711.87	12/1/01	12/31/2599	Guralp CMG-40T Seismometer	0	-90	40	M
		BH1	-77.530420	167.139711	3711.87	12/1/01	12/31/2599	Guralp CMG-40T Seismometer	56	0	40	M
		BH2	-77.530420	167.139711	3711.87	12/1/01	12/31/2599	Guralp CMG-40T Seismometer	146	0	40	M
		IS1	-77.530455	167.139837	3712.78	1/1/03	12/31/2599	Electric Condenser	NA	NA	40	Counts
		IS2	-77.530000	167.150000	3731.88	12/14/06	12/31/2599	Honeywell Pressure Transducer	NA	NA	40	Counts
		IS3	-77.530456	167.139847	3658.71	1/1/06	12/31/2599	Honeywell Pressure Transducer	NA	NA	40	Counts
		IS2	-77.530339	167.150903	3769.53	1/1/03	12/13/2006	Electric Condenser	NA	NA	40	Counts
ER	CON	BHZ	-77.534643	167.084940	3455.62	1/1/02	12/31/2599	Guralp CMG-40T Seismometer	0	-90	40	M
		BH1	-77.534643	167.084940	3455.62	1/1/02	12/31/2599	Guralp CMG-40T Seismometer	66	0	40	M
		BH2	-77.534643	167.084940	3455.62	1/1/02	12/31/2599	Guralp CMG-40T Seismometer	156	0	40	M
ER	LEH	BHZ	-77.510599	167.142086	3400.80	1/1/02	12/31/2599	Guralp CMG-40T Seismometer	0	-90	40	M
		BH1	-77.510599	167.142086	3400.80	1/1/02	12/31/2599	Guralp CMG-40T Seismometer	163	0	40	M
		BH2	-77.510599	167.142086	3400.80	1/1/02	12/31/2599	Guralp CMG-40T Seismometer	253	0	40	M
ER	HOO	BHZ	-77.531603	166.932620	2069.06	1/1/02	12/31/2599	Guralp CMG-40T Seismometer	0	-90	40	M
		BH1	-77.531603	166.932620	2070.06	1/1/02	12/31/2599	Guralp CMG-40T Seismometer	85	0	40	M
		BH2	-77.531603	166.932620	2071.06	1/1/02	12/31/2599	Guralp CMG-40T Seismometer	175	0	40	M
ER	RAY	BHZ	-77.528559	167.170830	3766.51	1/1/04	3/7/2007	Guralp CMG-40T Seismometer	0	-90	40	M
		BH1	-77.528559	167.170830	3766.51	1/1/04	3/7/2007	Guralp CMG-40T Seismometer	323	0	40	M
		BH2	-77.528559	167.170830	3766.51	1/1/04	3/7/2007	Guralp CMG-40T Seismometer	53	0	40	M
		IS1	-77.528559	167.170830	3766.51	12/14/06	12/31/2599	Honeywell Pressure Transducer	NA	NA	40	Counts
		IS2	-77.528571	167.170849	3765.74	1/1/05	12/31/2599	Honeywell Pressure Transducer	NA	NA	40	Counts
		IS1	-77.528559	167.170830	3766.51	1/1/03	12/13/2006	Electric Condenser	NA	NA	40	Counts
ER	SIS	EHZ	-77.570000	166.980000	1737.00	1/1/01	12/31/2002	L4C	0	-90	40	M
		EHN	-77.570000	166.980000	1737.00	1/1/01	12/31/2002	L4C	0	0	40	M
		EHE	-77.570000	166.980000	1737.00	1/1/01	12/31/2002	L4C	90	0	40	M
ER	ICE	EHZ	-77.552280	167.282850	2370.12	11/1/06	12/31/2599	L4C	0	-90	40	M/S
ER	BOM	EHZ	-77.508949	167.440181	1959.57	11/20/81	12/31/2599	L4C	0	-90	40	M/S
ER	SIS	EHZ	-77.570000	166.980000	1737.00	12/1/06	12/31/2599	L4C	0	-90	40	M/S
ER	BRD	EHZ	-77.271500	166.745640	1801.98	12/1/83	12/31/2599	L4C	0	-90	40	M/S
ER	ABB	EHZ	-77.456879	166.908938	1734.27	12/19/80	12/31/2599	L4C	0	-90	40	M/S
ER	HOO	EHZ	-77.531603	166.932620	2069.06	12/19/80	12/31/2001	L4C	0	-90	40	M/S
ER	MAC	EHZ	-77.532529	167.246628	3277.84	12/1/89	12/31/2599	L4C	0	-90	40	M/S
ER	HEL	EHZ	-77.505252	167.177541	3299.90	11/30/94	12/31/2005	L4C	0	-90	40	M/S
ER	CON	EHZ	-77.460000	166.910000	3401.39	11/1/84	12/31/2006	L4C	0	-90	40	M/S

Figure C.1: Metadata for MEVO Stations

MRI Seismic Channels					
Station	S/N	Gd (uv/c)	Gs (m/s/V) (1 Hz)	G ((um/s)/c)	1/G (c/(um/s))
E1S V	D0912	3.485	3.13E-04	1.09E-03	918.221
R (1)		3.504	3.13E-04	1.10E-03	913.242
T (2)		3.514	3.13E-04	1.10E-03	910.643
NKB V	D0913	3.522	3.13E-04	1.10E-03	908.575
R		3.522	3.13E-04	1.10E-03	908.575
T		3.513	3.13E-04	1.10E-03	910.902
CON V	T4D63/D0891	1.274	6.29E-04	8.02E-04	1247.253
R (1)		1.271	6.26E-04	7.95E-04	1257.278
T (2)		1.266	6.29E-04	7.96E-04	1255.924
LEH V	T41061/D0791	1.271	6.28E-04	7.98E-04	1253.344
R (1)		1.278	6.22E-04	7.95E-04	1258.216
T (2)		1.285	6.24E-04	8.02E-04	1246.693
HOO V	T4D35/D0883	1.273	6.28E-04	7.99E-04	1251.375
R (1)		1.264	6.20E-04	7.84E-04	1275.316
T (2)		1.261	6.23E-04	7.86E-04	1272.006

Figure C.2: Conversion Factors for Operational MEVO Broadband Stations

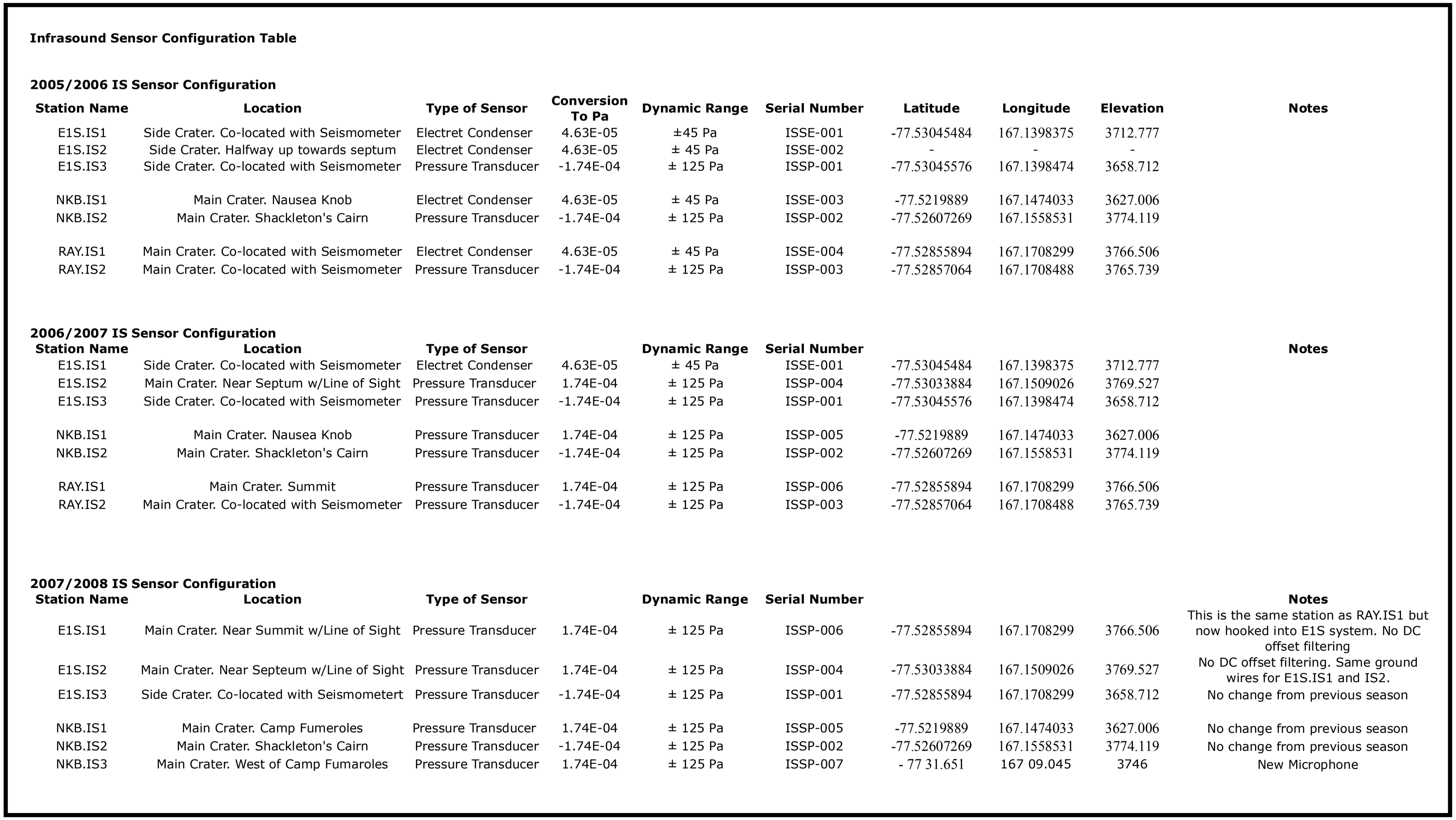

Infrasound Sensor Configuration Table

2005/2006 IS Sensor Configuration

Station Name	Location	Type of Sensor	Conversion To Pa	Dynamic Range	Serial Number	Latitude	Longitude	Elevation	Notes
E1S.IS1	Side Crater. Co-located with Seismometer	Electret Condenser	4.63E-05	±45 Pa	ISSE-001	-77.53045484	167.1398375	3712.777	
E1S.IS2	Side Crater. Halfway up towards septum	Electret Condenser	4.63E-05	± 45 Pa	ISSE-002	-	-	-	
E1S.IS3	Side Crater. Co-located with Seismometer	Pressure Transducer	-1.74E-04	± 125 Pa	ISSP-001	-77.53045576	167.1398474	3658.712	
NKB.IS1	Main Crater. Nausea Knob	Electret Condenser	4.63E-05	± 45 Pa	ISSE-003	-77.5219889	167.1474033	3627.006	
NKB.IS2	Main Crater. Shackleton's Cairn	Pressure Transducer	-1.74E-04	± 125 Pa	ISSP-002	-77.52607269	167.1558531	3774.119	
RAY.IS1	Main Crater. Co-located with Seismometer	Electret Condenser	4.63E-05	± 45 Pa	ISSE-004	-77.52855894	167.1708299	3766.506	
RAY.IS2	Main Crater. Co-located with Seismometer	Pressure Transducer	-1.74E-04	± 125 Pa	ISSP-003	-77.52857064	167.1708488	3765.739	

2006/2007 IS Sensor Configuration

Station Name	Location	Type of Sensor		Dynamic Range	Serial Number				Notes
E1S.IS1	Side Crater. Co-located with Seismometer	Electret Condenser	4.63E-05	± 45 Pa	ISSE-001	-77.53045484	167.1398375	3712.777	
E1S.IS2	Main Crater. Near Septum w/Line of Sight	Pressure Transducer	1.74E-04	± 125 Pa	ISSP-004	-77.53033884	167.1509026	3769.527	
E1S.IS3	Side Crater. Co-located with Seismometer	Pressure Transducer	-1.74E-04	± 125 Pa	ISSP-001	-77.53045576	167.1398474	3658.712	
NKB.IS1	Main Crater. Nausea Knob	Pressure Transducer	1.74E-04	± 125 Pa	ISSP-005	-77.5219889	167.1474033	3627.006	
NKB.IS2	Main Crater. Shackleton's Cairn	Pressure Transducer	-1.74E-04	± 125 Pa	ISSP-002	-77.52607269	167.1558531	3774.119	
RAY.IS1	Main Crater. Summit	Pressure Transducer	1.74E-04	± 125 Pa	ISSP-006	-77.52855894	167.1708299	3766.506	
RAY.IS2	Main Crater. Co-located with Seismometer	Pressure Transducer	-1.74E-04	± 125 Pa	ISSP-003	-77.52857064	167.1708488	3765.739	

2007/2008 IS Sensor Configuration

Station Name	Location	Type of Sensor		Dynamic Range	Serial Number				Notes
E1S.IS1	Main Crater. Near Summit w/Line of Sight	Pressure Transducer	1.74E-04	± 125 Pa	ISSP-006	-77.52855894	167.1708299	3766.506	This is the same station as RAY.IS1 but now hooked into E1S system. No DC offset filtering
E1S.IS2	Main Crater. Near Septeum w/Line of Sight	Pressure Transducer	1.74E-04	± 125 Pa	ISSP-004	-77.53033884	167.1509026	3769.527	No DC offset filtering. Same ground wires for E1S.IS1 and IS2.
E1S.IS3	Side Crater. Co-located with Seismometert	Pressure Transducer	-1.74E-04	± 125 Pa	ISSP-001	-77.52855894	167.1708299	3658.712	No change from previous season
NKB.IS1	Main Crater. Camp Fumeroles	Pressure Transducer	1.74E-04	± 125 Pa	ISSP-005	-77.5219889	167.1474033	3627.006	No change from previous season
NKB.IS2	Main Crater. Shackleton's Cairn	Pressure Transducer	-1.74E-04	± 125 Pa	ISSP-002	-77.52607269	167.1558531	3774.119	No change from previous season
NKB.IS3	Main Crater. West of Camp Fumaroles	Pressure Transducer	1.74E-04	± 125 Pa	ISSP-007	- 77 31.651	167 09.045	3746	New Microphone

Figure C.3: Metadata for MEVO Infrasound 2005-2008. Courtesy of Kyle Jones.

APPENDIX D

MEVO STATION UP TIME

One of the important developments of this dissertation was to evaluate the network for station up time. This resulted in the evaluation of each of the broadband station's individual performances, as well as three of the long running infrasound sensors. The following figures show the general trends of station's being operational during the austral summer months, with a few years where the station was operation through the austral winter. The code used to evaluate these performances checks the continuous record (catalogd at NMT) for the existence of a file. It does not guarantee that the data within the file is useful. Regardless it does provide a first order approximation of operational time for each station. Note that the similar figures, except for the one using only MAC, shown in the first two chapters require that three stations are operational. This is the requirement for the matched filter detection process. The shaded areas represent the operational times, whereas the blank times represent station down time.

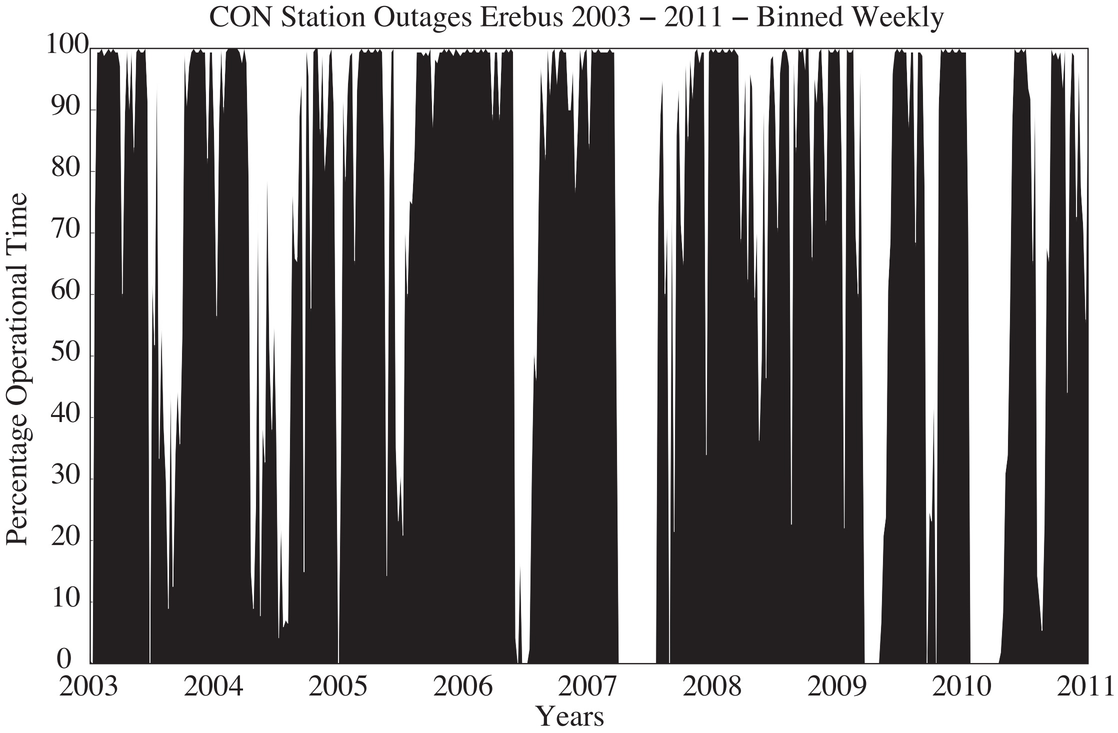

Figure D.1: CON Seismic Station Up Times

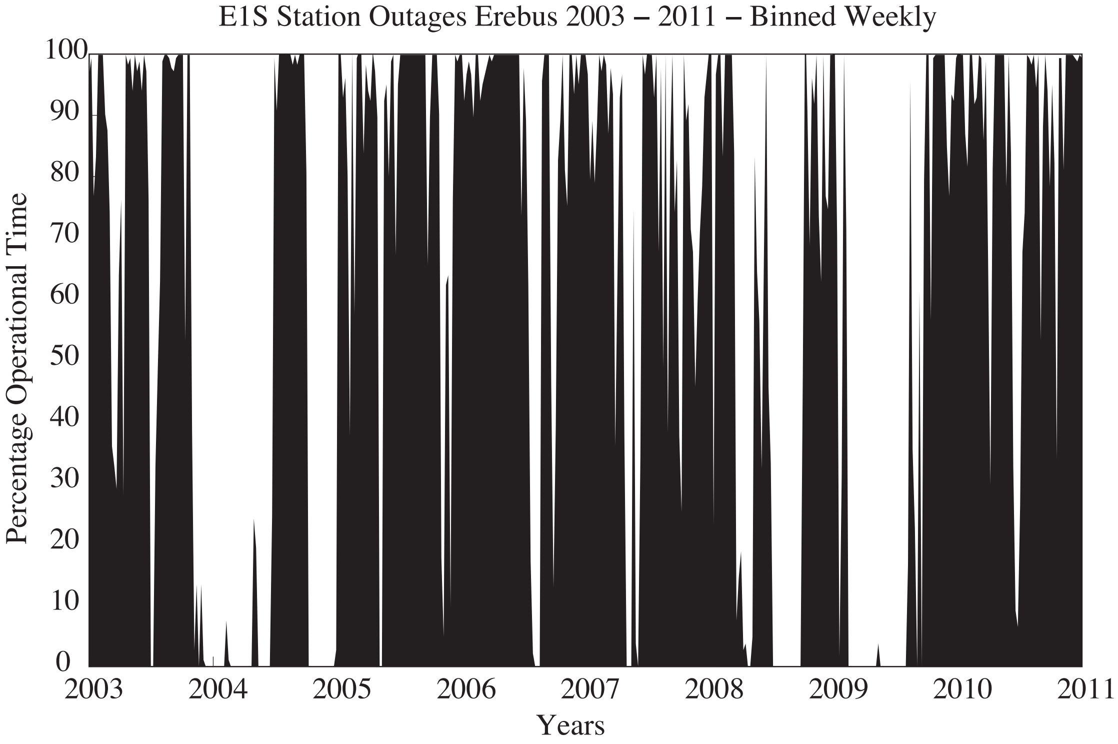

Figure D.2: E1S Seismic Station Up Times

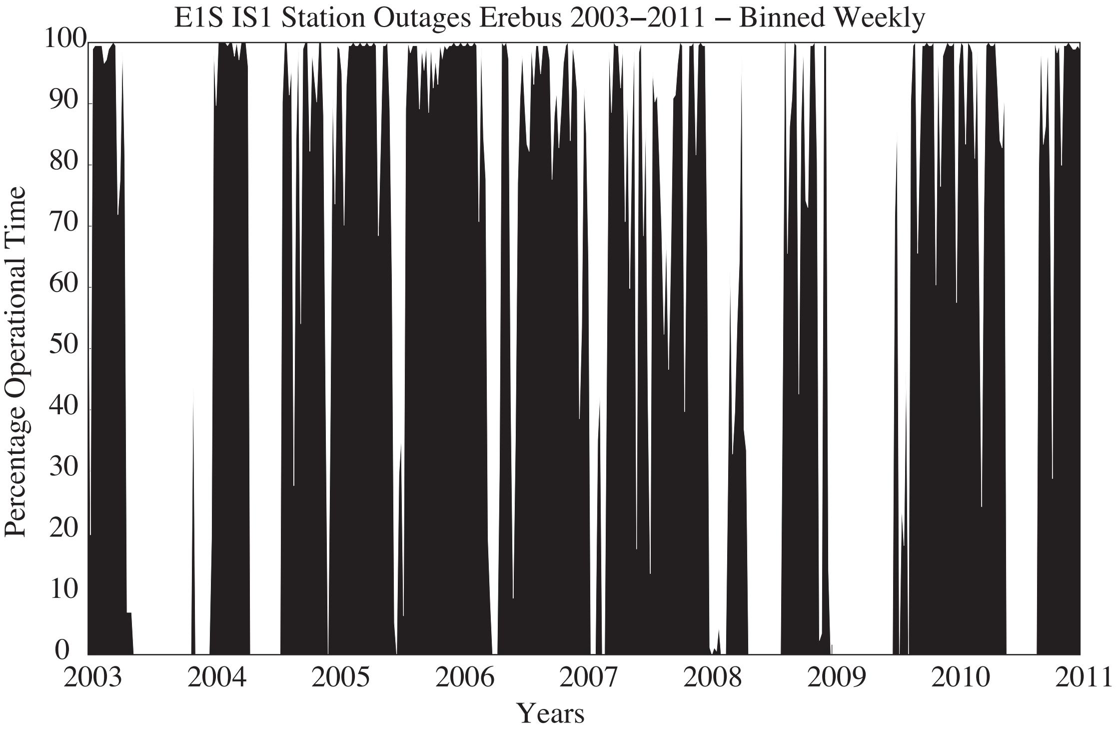

Figure D.3: E1S Infrasound Channel 1 Station Up Times

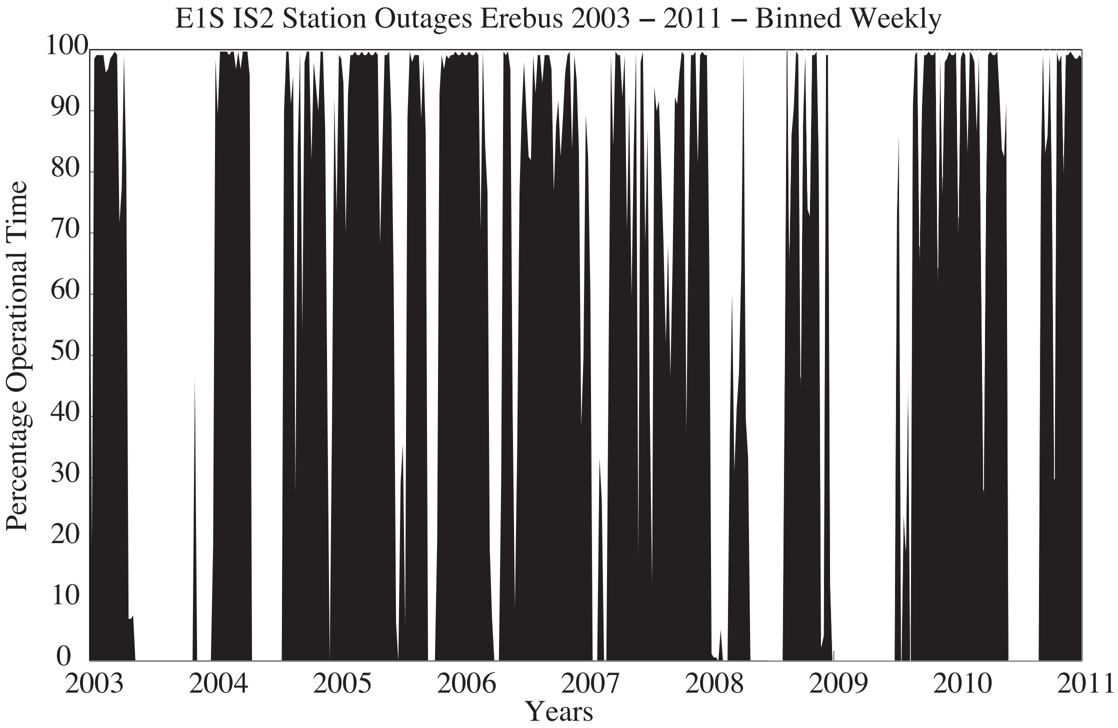

Figure D.4: E1S Infrasound Channel 2 Station Up Times

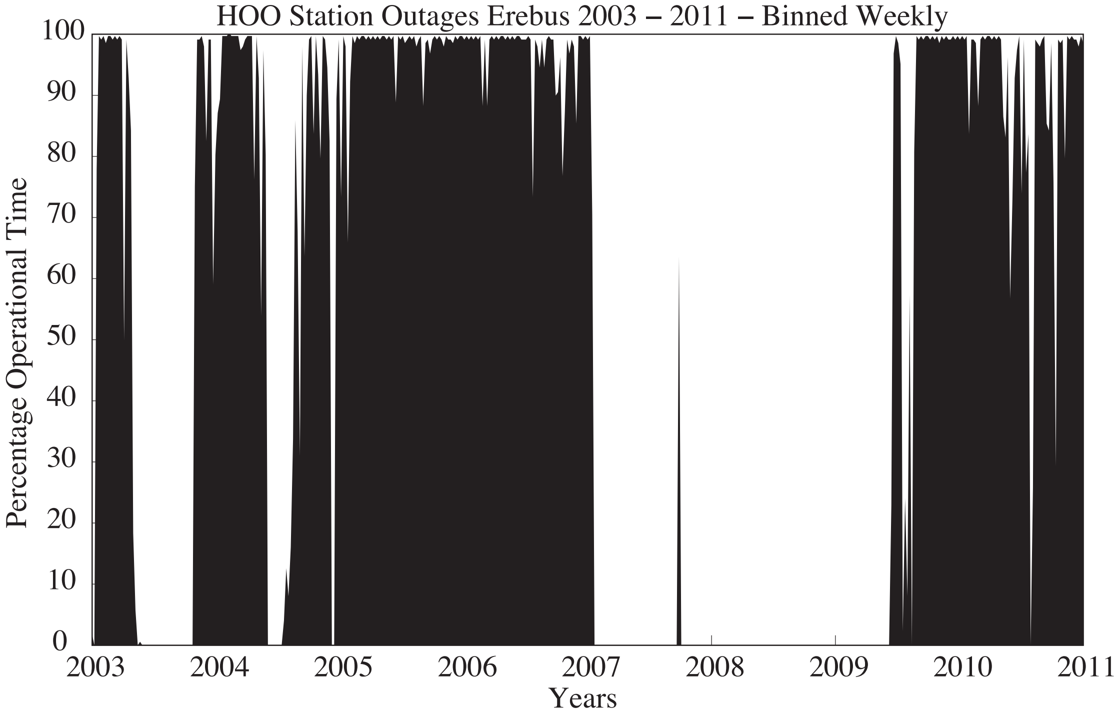

Figure D.5: HOO Seismic Station Up Times

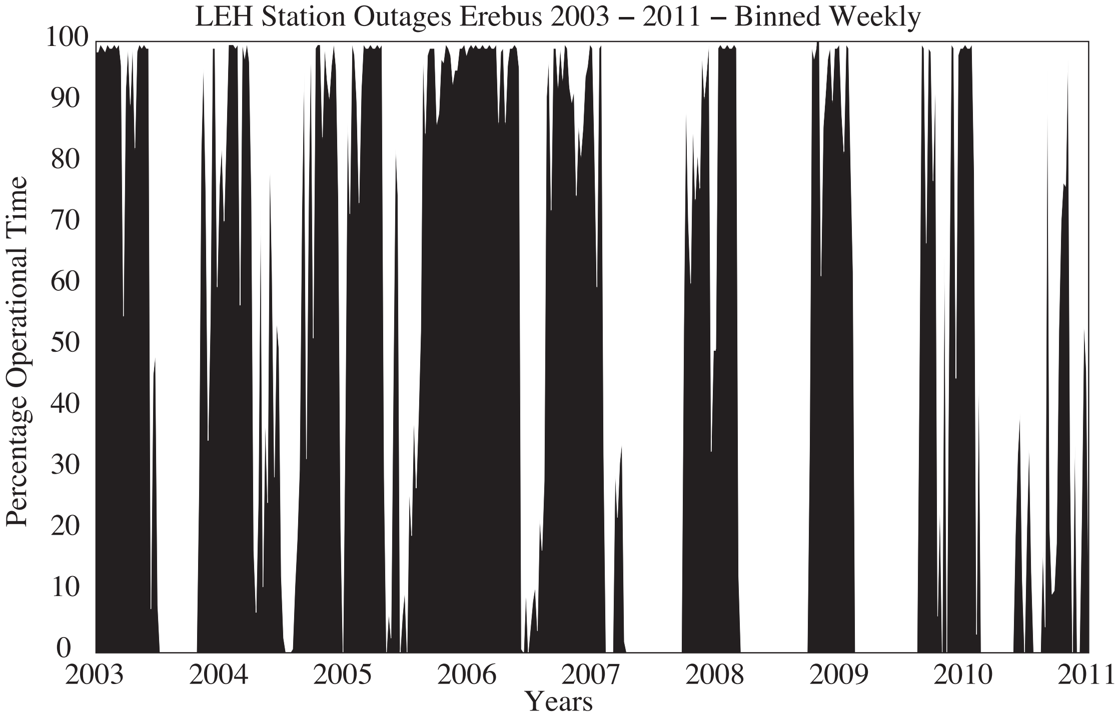

Figure D.6: LEH Seismic Station Up Times

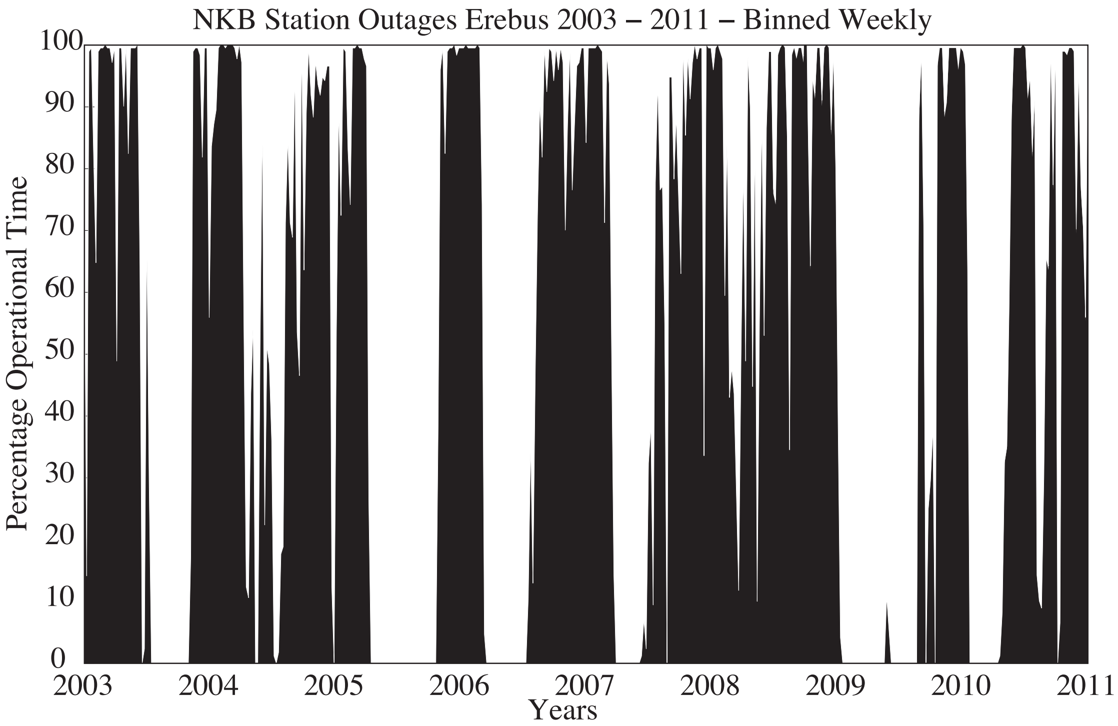

Figure D.7: NKB Seismic Station Up Times

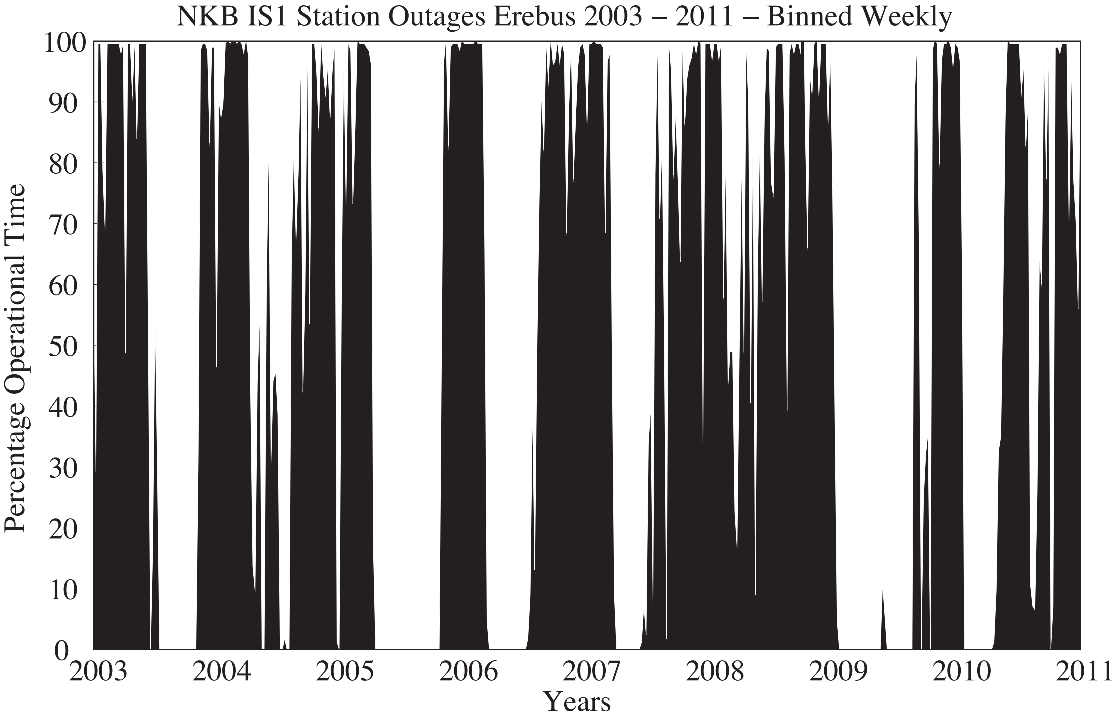

Figure D.8: NKB Infrasound Channel 1 Station Up Times

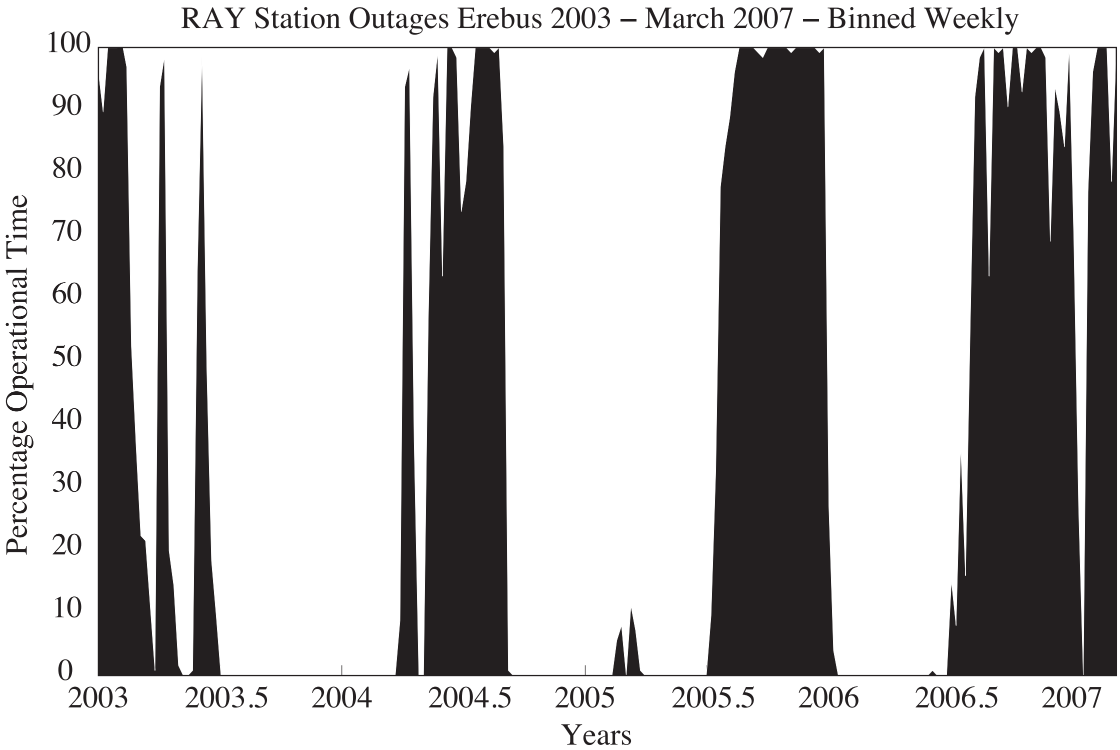

Figure D.9: RAY Seismic Station Up Times

APPENDIX E

TEMPORARY DEPLOYMENTS STATION METADATA

The information in this appendix pertains to the station metadata for each of the temporary deployments: ETB 2007-2008 and ETS 2008. The ETB deployment consisted of 24 CMG-40T seismometers deployed in two concentric rings, one at approximately 2,000 m a.s.l. and one at 3,000 m a.s.l. These stations recorded at 100, 40, and 200 samples per second for various time periods. One of these stations, ETB 9, was switched to an L-28 seismometer during the 2008 field season and shot program. The ETS station was comprised of 98 L-28 seismometers, twenty of which were deployed along the Erebus - Terror Axis from Cape Crozier to Cape Royds (ETS-2D). The remaining 78 were deployed on the upper plateau of Erebus Volcano (ETS-3D). These stations operated at 200 samples per second. The following tables/figures contain the DAS serial number, sensor serial number, first day of recording, last day of recording, latitude, and longitude for each station. For precise elevations please refer to Figure/Table E.10 and E.11.

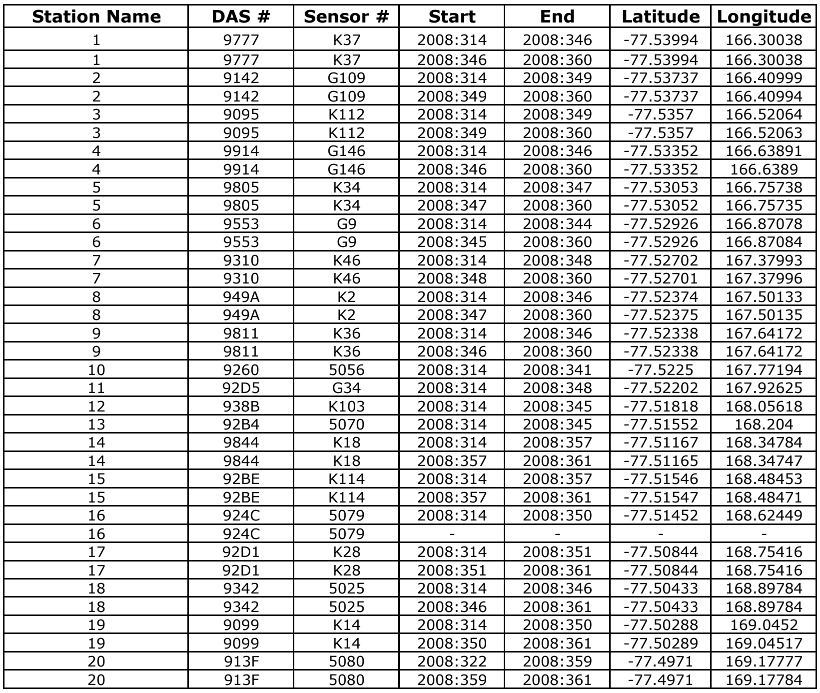

Station Name	DAS #	Sensor #	Start	End	Latitude	Longitude
1	9777	K37	2008:314	2008:346	-77.53994	166.30038
1	9777	K37	2008:346	2008:360	-77.53994	166.30038
2	9142	G109	2008:314	2008:349	-77.53737	166.40999
2	9142	G109	2008:349	2008:360	-77.53737	166.40994
3	9095	K112	2008:314	2008:349	-77.5357	166.52064
3	9095	K112	2008:349	2008:360	-77.5357	166.52063
4	9914	G146	2008:314	2008:346	-77.53352	166.63891
4	9914	G146	2008:346	2008:360	-77.53352	166.6389
5	9805	K34	2008:314	2008:347	-77.53053	166.75738
5	9805	K34	2008:347	2008:360	-77.53052	166.75735
6	9553	G9	2008:314	2008:344	-77.52926	166.87078
6	9553	G9	2008:345	2008:360	-77.52926	166.87084
7	9310	K46	2008:314	2008:348	-77.52702	167.37993
7	9310	K46	2008:348	2008:360	-77.52701	167.37996
8	949A	K2	2008:314	2008:346	-77.52374	167.50133
8	949A	K2	2008:347	2008:360	-77.52375	167.50135
9	9811	K36	2008:314	2008:346	-77.52338	167.64172
9	9811	K36	2008:346	2008:360	-77.52338	167.64172
10	9260	5056	2008:314	2008:341	-77.5225	167.77194
11	92D5	G34	2008:314	2008:348	-77.52202	167.92625
12	938B	K103	2008:314	2008:345	-77.51818	168.05618
13	92B4	5070	2008:314	2008:345	-77.51552	168.204
14	9844	K18	2008:314	2008:357	-77.51167	168.34784
14	9844	K18	2008:357	2008:361	-77.51165	168.34747
15	92BE	K114	2008:314	2008:357	-77.51546	168.48453
15	92BE	K114	2008:357	2008:361	-77.51547	168.48471
16	924C	5079	2008:314	2008:350	-77.51452	168.62449
16	924C	5079	-	-	-	-
17	92D1	K28	2008:314	2008:351	-77.50844	168.75416
17	92D1	K28	2008:351	2008:361	-77.50844	168.75416
18	9342	5025	2008:314	2008:346	-77.50433	168.89784
18	9342	5025	2008:346	2008:361	-77.50433	168.89784
19	9099	K14	2008:314	2008:350	-77.50288	169.0452
19	9099	K14	2008:350	2008:361	-77.50289	169.04517
20	913F	5080	2008:322	2008:359	-77.4971	169.17777
20	913F	5080	2008:359	2008:361	-77.4971	169.17784

Figure E.1: ETS 2-D Station Metadata

Station Name	DAS #	Sensor #	Start	End	Latitude	Longitude
21	978F	K9	2008:325	2008:362	-77.5099	167.16557
22	978A	G-056	2008:331	2008:360	-77.50983	167.14503
23	9874	G407	2008:317	2008:361	-77.5121	167.13493
24	929D	5-003	2008:330	2008:361	-77.51435	167.12445
25	92D6	5-083	2008:317	2008:361	-77.51212	167.11406
26	9240	G083	2008:330	2008:361	-77.51659	167.093
27	92A4	K121	2008:331	2008:362	-77.50987	167.20732
28	9828	5-066	2008:332	2008:362	-77.51208	167.19729
29	987D	G213	-	-	-	-
30	9896	G139	2008:322	2008:361	-77.52112	167.09288
31	945A	G028	2008:325	2008:361	-77.51889	167.10345
32	9140	5-100	2008:325	2008:361	-77.51606	167.10916
33	92EA	G035	2008:329	2008:362	-77.51213	167.1762
34	92F0	5-016	2008:329	2008:362	-77.51207	167.15577
35	92E4	G232	2000:001	2008:361	-77.51439	167.14486
36	92A0	K57	2008:331	2008:362	-77.51661	167.13501
37	9780	5091	2008:332	2008:361	-77.51859	167.12402
38	92E2	5-014	2008:331	2008:361	-77.52116	167.11426
39	92A5	G177	2008:329	2008:362	-77.52344	167.12413
40	92C9	5-020	2008:332	2008:360	-77.52567	167.11426
41	9261	K113	2008:330	2008:360	-77.52791	167.1031
42	9559	G119	2008:330	2008:360	-77.53006	167.09288
43	91F7	K101	2008:330	2008:361	-77.52342	167.10374
44	9917	G-175	2008:322	2008:360	-77.52564	167.09313
45	9294	G301	2008:325	2008:361	-77.51438	167.20756
46	9290	K12	2008:329	2008:361	-77.51662	167.19693
47	9283	G351	2008:325	2008:361	-77.51894	167.18651
48	983D	237	2008:325	2008:361	-77.51657	167.17658
49	9803	5052	2008:325	2008:361	-77.51435	167.16609
50	9912	G217	2008:330	2008:362	-77.51434	167.18666
51	9869	G323	2008:317	2008:361	-77.51882	167.16587
52	944C	G096	2008:317	2008:361	-77.52333	167.16593
53	9241	G311	2008:330	2008:361	-77.52119	167.17656
54	983E	G361	2008:325	2008:361	-77.51892	167.20757
55	91E5	G216	2008:331	2008:361	-77.52118	167.21802
56	990D	G046	2008:327	2008:361	-77.52329	167.18687
57	92F7	5-038	2008:329	2008:362	-77.51702	167.21719
58	9891	K64	2008:322	2008:361	-77.52345	167.20699
59	9446	K102	2008:330	2008:362	-77.52105	167.19776
60	924A	5048	2008:325	2008:361	-77.51439	167.10342
61	9864	5083	2008:332	2008:362	-77.51672	167.15409
62	9512	K-41	2008:317	2008:362	-77.52016	167.13886
63	947D	5-022	2008:332	2008:362	-77.5189	167.14537
64	9491	5054	2008:330	2008:362	-77.52115	167.15534
65	947A	G316	2008:331	2008:361	-77.52562	167.13679
66	924E	K51	2008:329	2008:359	-77.52785	167.14371
67	9453	G-153	2008:331	2008:362	-77.50768	167.15874
68	930A	G302	2008:322	2008:345	-77.53487	167.0934
69	9461	5026	2008:322	2008:360	-77.53218	167.10373
70	995C	G111B	2008:322	2008:360	-77.52748	167.12784
71	9466	K43	2008:329	2008:361	-77.53011	167.11364
72	9238	G068	2008:325	2008:360	-77.53485	167.113
73	9292	G134	2008:322	2008:361	-77.50758	167.17648
74	990F	5053	2008:322	2008:361	-77.50765	167.19571
75	92A1	5-094	2008:331	2008:362	-77.50758	167.11426
76	92DD	G-364	2008:330	2008:362	-77.50991	167.10369
77	929B	K23	2008:329	2008:360	-77.53509	167.15373
78	9293	K42	2008:331	2008:361	-77.53423	167.17502
79	9334	5095	2008:325	2008:360	-77.5324	167.12409
80	9791	K52	2008:317	2008:360	-77.5346	167.13564
81	980E	5075	2008:322	2008:360	-77.53256	167.14668
82	986C	K38	2008:317	2008:362	-77.52963	167.09758

Figure E.2: ETS 3-D Station Metadata

Station Name	DAS #	Sensor #	Start	End	Latitude	Longitude
83	9C30	G-383	2008:317	2008:362	-77.51224	167.09409
84	943F	K15	2008:331	2008:361	-77.51233	167.06478
85	9924	G060	2008:332	2008:361	-77.52435	167.23053
86	9462	G203	2008:332	2008:361	-77.52793	167.18616
87	9237	K117	2008:331	2008:361	-77.53258	167.1859
88	9926	G214	2008:331	2008:361	-77.53063	167.17526
89	9245	K32	2008:331	2008:362	-77.50752	167.13603
90	9009	G337	2008:331	2008:360	-77.53096	167.14265
91	956F	K20	2008:331	2008:363	-77.52572	167.07326
92	925D	G-034	2008:331	2008:362	-77.52332	167.14515
93	92F4	G221	2008:334	2008:361	-77.52562	167.21814
94	909A	G181	2008:336	2008:361	-77.52788	167.20786
95	9560	G403	2008:331	2008:361	-77.53015	167.19658
96	92C4	5-074	2008:331	2008:361	-77.53007	167.2178
97	92AC	G225	2008:331	2008:361	-77.52956	167.23168
98	991C	G122	2008:331	2008:361	-77.52537	167.15936
99	92AB	K190	2008:332	2008:363	-77.50123	167.20651
DOWNHOLE INST	9305					

Figure E.3: ETS 3-D Station Metadata

ETB 2007-11/2008 Station Information				
DAS #	STATION NAME	Lat	Long	Elev
9891	ETB1	-77.524500	166.964417	2100
9892	ETB2	-77.548567	166.972050	2066
9866	ETB3	-77.508133	166.931617	1952
9873	ETB4	-77.496500	166.965167	2055
9848	ETB5	-77.492300	167.077967	2516
9848	ETB5A	-77.492167	167.051167	2450
9915	ETB6	-77.492083	167.105167	2588
995F	ETB7	-77.562800	166.977700	1786
990B	ETB8	-77.504183	167.336983	2420
995D	ETB9	-77.542717	166.164600	21
9926	ETB10	-77.552350	167.282717	2325
9896	ETB11	-77.517917	167.151567	3493
985B	ETB12	-77.515117	167.109217	3364
9868	ETB13	-77.547933	167.360350	1999
9917	ETB14	-77.515417	167.194300	3456
9859	ETB15	-77.537333	167.144517	3097
995C	ETB16	-77.511700	167.079967	3266
995A	ETB17	-77.533283	167.208633	3108
9C30	ETB18	-77.524883	167.197683	3566
988F	ETB19	-77.505250	167.177533	3207
990F	ETB20	-77.525333	167.104700	3441
984D	ETB21	-77.500167	167.225217	3000
9920	ETB22	-77.518967	167.224267	3452
983E	ETB23	-77.523383	167.050150	3171
9876	ETB24	-77.575517	167.124017	1568

Figure E.4: ETB Station Metadata for 2007 through 11/2008

ETB - 11/2008-Pullout Station Information					
DAS #	STATION NAME	Lat	Long	Elev	Notes
9297	ETB1	-77.524500	166.964417	2100	
9892	ETB2	-77.548567	166.972050	2066	
9866	ETB3	-77.508133	166.931617	1952	
9873	ETB4	-77.496500	166.965167	2055	
9848	ETB5A	-77.492167	167.051167	2450	
9915	ETB6	-77.492083	167.105167	2588	
995F	ETB7	-77.562800	166.977700	1786	
990B	ETB8	-77.504183	167.336983	2420	
995D	ETB9	-77.542717	166.164600	21	Sensor Swapped for L-28 SN: G234
92C8	ETB10	-77.552350	167.282717	2325	Sensor T4896
976C	ETB11	-77.517917	167.151567	3493	
985B	ETB12	-77.515117	167.109217	3364	
9868	ETB13	-77.547933	167.360350	1999	
944B	ETB14	-77.515417	167.194300	3456	
9859	ETB15	-77.537333	167.144517	3097	
92D9	ETB16	-77.511700	167.079967	3266	
995A	ETB17	-77.533283	167.208633	3108	
995B	ETB18	-77.524883	167.197683	3566	
988F	ETB19	-77.505250	167.177533	3207	
953B	ETB20	-77.525333	167.104700	3441	
984D	ETB21	-77.500167	167.225217	3000	
9920	ETB22	-77.518967	167.224267	3452	
9343	ETB23	-77.523383	167.050150	3171	
9876	ETB24	-77.575517	167.124017	1568	

Figure E.5: ETB Station Metadata for 12/2008

All of the data from the temporary networks were submitted to the IRIS DMC. The continuous data from the ETB stations were submitted under the network code ZW, while the continuous data from the ETS stations were submitted under the network code Y4. As per the instructions of the IRIS DMC, the active shots conducted in December of 2008 were also cut from both the temporary networks. Note that the shots from the 2007-08 field season were not submitted as an assembled data set. Also, the shots were not cut from the MEVO permanent network (ER). This data was compiled as a PH5 data set and can be found through the IRIS DMC under Assembled Data Set ID 10-021. The PH5 data set references the stations with a four digit number. The following tables/figures relate the station names to the PH5 numbering convention.

Station or Shot Name	**PH5 Station Name**	**DAS Number**
ETS 1	2001	9777
ETS 2	2002	9142
ETS 3	2003	9095
ETS 4	2004	9914
ETS 5	2005	9805
ETS 6	2006	9553
ETS 7	2007	9310
ETS 8	2008	949A
ETS 9	2009	9811
ETS 10	2010	9260
ETS 11	2011	92D5
ETS 12	2012	938B
ETS 13	2013	92B4
ETS 14	2014	9844
ETS 15	2015	92BE
ETS 16	2016	924C
ETS 17	2017	92D1
ETS 18	2018	9342
ETS 19	2019	9099
ETS 20	2020	913F
ETS 21	3021	978F
ETS 22	3022	978A
ETS 23	3023	9874
ETS 24	3024	929D
ETS 25	3025	92D6
ETS 26	3026	9240
ETS 27	3027	92A4
ETS 28	3028	9828
ETS 29	3029	987D
ETS 30	3030	9896
ETS 31	3031	945A
ETS 32	3032	9140
ETS 33	3033	92EA
ETS 34	3034	92F0
ETS 35	3035	92E4
ETS 36	3036	92A0
ETS 37	3037	9780
ETS 38	3038	92E2
ETS 39	3039	92A5
ETS 40	3040	92C9
ETS 41	3041	9261
ETS 42	3042	9559

Figure E.6: ETS Station Relation to PH5 Assembled Data Set

Station or Shot Name	PH5 Station Name	DAS Number
ETS 43	3043	91F7
ETS 44	3044	9917
ETS 45	3045	9294
ETS 46	3046	9290
ETS 47	3047	9283
ETS 48	3048	983D
ETS 49	3049	9803
ETS 50	3050	9912
ETS 51	3051	9869
ETS 52	3052	944C
ETS 53	3053	9241
ETS 54	3054	983E
ETS 55	3055	91E5
ETS 56	3056	990D
ETS 57	3057	92F7
ETS 58	3058	9891
ETS 59	3059	9446
ETS 60	3060	924A
ETS 61	3061	9864
ETS 62	3062	9512
ETS 63	3063	947D
ETS 64	3064	9491
ETS 65	3065	947A
ETS 66	3066	924E
ETS 67	3067	9453
ETS 68	3068	930A
ETS 69	3069	9461
ETS 70	3070	995C
ETS 71	3071	9466
ETS 72	3072	9238
ETS 73	3073	9292
ETS 74	3074	990F
ETS 75	3075	92A1
ETS 76	3076	92DD
ETS 77	3077	929B
ETS 78	3078	9293
ETS 79	3079	9334
ETS 80	3080	9791
ETS 81	3081	980E
ETS 82	3082	986C
ETS 83	3083	9C30
ETS 84	3084	943F

Figure E.7: ETS Station Relation to PH5 Assembled Data Set

Station or Shot Name	PH5 Station Name	DAS Number
ETS 85	3085	9924
ETS 86	3086	9462
ETS 87	3087	9237
ETS 88	3088	9926
ETS 89	3089	9245
ETS 90	3090	9009
ETS 91	3091	956F
ETS 92	3092	925D
ETS 93	3093	92F4
ETS 94	3094	909A
ETS 95	3095	9560
ETS 96	3096	92C4
ETS 97	3097	92AC
ETS 98	3098	991C
ETS 99	3099	92AB

Figure E.8: ETS Station Relation to PH5 Assembled Data Set

Station or Shot Name	PH5 Station Name	DAS Number
ETB1	1001	9297
ETB2	1002	9892
ETB3	1003	9866
ETB4	1004	9873
ETB5A	1005	9848
ETB6	1006	9915
ETB7	1007	995F
ETB8	1008	990B
ETB9	1009	995D
ETB10	1010	92C8
ETB11	1011	976C
ETB12	1012	985B
ETB13	1013	9868
ETB14	1014	944B
ETB15	1015	9859
ETB16	1016	92D9
ETB17	1017	995A
ETB18	1018	995B
ETB19	1019	988F
ETB20	1020	953B
ETB21	1021	984D
ETB22	1022	9920
ETB23	1023	9343
ETB24	1024	9876

Figure E.9: ETB Station Relation to PH5 Assembled Data Set

As mentioned in Appendix B, the continuous data is also available in miniseed format as an Antelope Database. The shots were cut from this database in SAC format. The shots from field season 2007-2008 are available on the NMT server at /fs/eredata/Erebus/shot_data_07-08. The shots from field season 2008 are available at /fs/eredata/Erebus/shot_data_08.

During the course of the processing, it was discovered that the GPS elevations given by the stations were not accurate. These elevations have been fixed by referencing the two available DEMs in all places except in the shots. Note that the shots cannot simply be recut as valuable pick data will be lost. Therefore, the headers in the existing files will need to be fixed.

Station	Latitude	Longitude	Elevation (m)
ETB1	-77.524500	166.964417	2359
ETB2	-77.548567	166.972050	2114
ETB3	-77.508133	166.931617	2001
ETB4	-77.496500	166.965167	2143
ETB5	-77.492300	167.077967	2529
ETB5A	-77.492167	167.051167	2452
ETB6	-77.492083	167.105167	2583
ETB7	-77.562800	166.977700	1780
ETB8	-77.504183	167.336983	2495
ETB9	-77.542717	166.164600	16
ETB10	-77.552350	167.282717	2361
ETB11	-77.517917	167.151567	3494
ETB12	-77.515117	167.109217	3373
ETB13	-77.547933	167.360350	1979
ETB14	-77.515417	167.194300	3437
ETB15	-77.537333	167.144517	3405
ETB16	-77.511700	167.079967	3274
ETB17	-77.533283	167.208633	3437
ETB18	-77.524883	167.197683	3566
ETB19	-77.505250	167.177533	3290
ETB20	-77.525333	167.104700	3493
ETB21	-77.500167	167.225217	2951
ETB22	-77.518967	167.224267	3455
ETB23	-77.523383	167.050150	3236
ETB24	-77.575517	167.124017	1540
ETS 1	-77.53994	166.30038	173
ETS 2	-77.53737	166.40999	398
ETS 3	-77.5357	166.52064	633
ETS 4	-77.53352	166.63891	921
ETS 5	-77.53053	166.75738	1242
ETS 6	-77.52926	166.87078	1680
ETS 7	-77.52702	167.37993	2091
ETS 8	-77.52374	167.50133	1786
ETS 9	-77.52338	167.64172	1491
ETS 10	-77.5225	167.77194	1583
ETS 11	-77.52202	167.92625	2048
ETS 12	-77.51818	168.05618	1808
ETS 13	-77.51552	168.204	2007
ETS 14	-77.51167	168.34784	2501
ETS 15	-77.51546	168.48453	2925
ETS 16	-77.51452	168.62449	2860
ETS 17	-77.50844	168.75416	2317
ETS 18	-77.50433	168.89784	1841
ETS 19	-77.50288	169.0452	1346
ETS 20	-77.4971	169.17777	643
ETS 21	-77.5099	167.16557	3390
ETS 22	-77.50983	167.14503	3394
ETS 23	-77.5121	167.13493	3387
ETS 24	-77.51435	167.12445	3366
ETS 25	-77.51212	167.11406	3342
ETS 26	-77.51659	167.093	3345
ETS 27	-77.50987	167.20732	3361
ETS 28	-77.51208	167.19729	3382
ETS30	-77.52112	167.09288	3383
ETS31	-77.51889	167.10345	3377
ETS32	-77.51606	167.10916	3375
ETS33	-77.51213	167.1762	3399
ETS34	-77.51207	167.15577	3408
ETS35	-77.51439	167.14486	3417
ETS36	-77.51661	167.13501	3421
ETS37	-77.51859	167.12402	3446
ETS38	-77.52116	167.11426	3449
ETS39	-77.52344	167.12413	3573
ETS40	-77.52567	167.11426	3539
ETS41	-77.52791	167.1031	3512

Figure E.10: Corrected Station Elevations and Locations

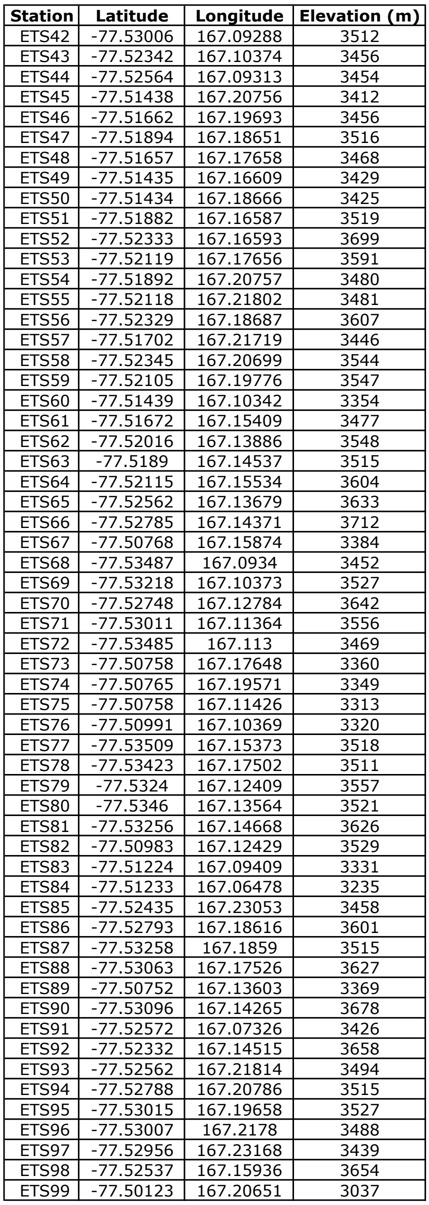

Station	Latitude	Longitude	Elevation (m)
ETS42	-77.53006	167.09288	3512
ETS43	-77.52342	167.10374	3456
ETS44	-77.52564	167.09313	3454
ETS45	-77.51438	167.20756	3412
ETS46	-77.51662	167.19693	3456
ETS47	-77.51894	167.18651	3516
ETS48	-77.51657	167.17658	3468
ETS49	-77.51435	167.16609	3429
ETS50	-77.51434	167.18666	3425
ETS51	-77.51882	167.16587	3519
ETS52	-77.52333	167.16593	3699
ETS53	-77.52119	167.17656	3591
ETS54	-77.51892	167.20757	3480
ETS55	-77.52118	167.21802	3481
ETS56	-77.52329	167.18687	3607
ETS57	-77.51702	167.21719	3446
ETS58	-77.52345	167.20699	3544
ETS59	-77.52105	167.19776	3547
ETS60	-77.51439	167.10342	3354
ETS61	-77.51672	167.15409	3477
ETS62	-77.52016	167.13886	3548
ETS63	-77.5189	167.14537	3515
ETS64	-77.52115	167.15534	3604
ETS65	-77.52562	167.13679	3633
ETS66	-77.52785	167.14371	3712
ETS67	-77.50768	167.15874	3384
ETS68	-77.53487	167.0934	3452
ETS69	-77.53218	167.10373	3527
ETS70	-77.52748	167.12784	3642
ETS71	-77.53011	167.11364	3556
ETS72	-77.53485	167.113	3469
ETS73	-77.50758	167.17648	3360
ETS74	-77.50765	167.19571	3349
ETS75	-77.50758	167.11426	3313
ETS76	-77.50991	167.10369	3320
ETS77	-77.53509	167.15373	3518
ETS78	-77.53423	167.17502	3511
ETS79	-77.5324	167.12409	3557
ETS80	-77.5346	167.13564	3521
ETS81	-77.53256	167.14668	3626
ETS82	-77.50983	167.12429	3529
ETS83	-77.51224	167.09409	3331
ETS84	-77.51233	167.06478	3235
ETS85	-77.52435	167.23053	3458
ETS86	-77.52793	167.18616	3601
ETS87	-77.53258	167.1859	3515
ETS88	-77.53063	167.17526	3627
ETS89	-77.50752	167.13603	3369
ETS90	-77.53096	167.14265	3678
ETS91	-77.52572	167.07326	3426
ETS92	-77.52332	167.14515	3658
ETS93	-77.52562	167.21814	3494
ETS94	-77.52788	167.20786	3515
ETS95	-77.53015	167.19658	3527
ETS96	-77.53007	167.2178	3488
ETS97	-77.52956	167.23168	3439
ETS98	-77.52537	167.15936	3654
ETS99	-77.50123	167.20651	3037

Figure E.11: Corrected Station Elevations and Locations

APPENDIX F

2007-08 SHOT INFORMATION

As mentioned above, the shot data from the 2007-2008 field season is available on the NMT server at /fs/eredata/Erebus/shot_data_07-08. These data are not part of the above mentioned PH5 Assembled Data Set and were not separately submitted to the IRIS DMC. They can be found in the continuous data for ZW and ER at the DMC. The following table/figure was contains the information for each of the shots.

Erebus Mini Controlled-Source Experiment Jan 2008

Products Used: **Amex 25 kg bags** **Boosters 400 g each** **Davey Dets - Seismic Caps**

	Depth (m)	Latitude (S)	Longitude (E)	Shot Day	Shot Time (UTC)	Amex (kg)	Boosters (g)	# Caps per Hole
Drill Site #1 - West								
Hole #1	9	77.50702	166.66895	19-Jan-08	255	75	1600	2
Hole #2	7	77.50724	166.66989		305	62.5	1600	2
Hole #3	7	77.50717	166.66974		305	62.5	1600	2
Fang								
Hole #1	15	77.49541	167.23105	19-Jan-08	130	100	3600	2
Hole #2	12.5	77.49545	167.23135		140	100	3600	2
*Hole #3	11.8	77.49541	167.23105		140	100	4000	3
Cones **								
Hole #1	6	77.53156	167.08541	30-Jan-08	1245	0	11200	2
Hole #2	12	77.53032	167.09233		1300	117	1600	2
Hole #3	12	77.53035	167.09220		1315	117	1600	2
Hole #4	12	77.53040	167.09208		1315	116	1600	2

*Sprung this hole **All Times for Cones are Local Times

Figure F.1: Shot Metadata 2007-2008 Field Season

APPENDIX G

2008-09 SHOT INFORMATION

As mentioned above, the shot data from the 2008-2009 field season is available on the NMT server at /fs/eredata/Erebus/shot_data_08 and as a PH5 data set under the Assembled Data Set ID 10-21 at the IRIS DMC. Again note that the elevations in the cut SAC files on the NMT server do not contain accurate elevation information. It is recommended that the existing files be fixed and not simply replaced since the files contain valuable pick information. The following three tables/figures were compiled to accurately describe the shot information. Note on the last table/figure the PH5 reference number for each of the shots is listed.

Shot information for MEVO 2009-2009 season

Shot Point name	# holes	depth (m)	ANFO/ TNT hole (kg)	Location (WGS84) Latitude	 Longitude	 Ellipsoid Height (m)	 Elev. MSL (m)	Date Local	Time (UTC) yyyy:jd:hr:mn:ss
comments	bottom to top. 2, 25Kg bags ANFO 1 capped booster, more bags ANFO and another capped booster, 1 Bag ANFO (125 Kg/hole). All shots with multiple holes are wired in series. Approx. 6 meters of stemming. ANFO holes had ~ 1 gallon water poured ~ meter below surface and holes left to sinter for 2 days.								
Windless Bight	4	15	500	77 44'48.01039"S	167 25'31.21759"E	-15.99	37.65	Dec. 11	2008:346:01:40:00
comments	Bottom to top. Same design above for the 4 outside holes the middle hole had 2 bags and 1 capped booster then another 2 bags and 15 boosters (1 capped). Approx. 5 - 6 meters of stemming.								
Cape Crozier	5	14.5	600	77 31' 13.95168"S	169 33'24.27598"E	-33.005	22.06	Dec. 11	2008:346:00:17:00
comments	This shot used det cord and dynamite. There was 1, 4" hole through the sea ice (5' thick). There were 5, 100' det cords with 22 - 23 sticks end to end on each. The top of the dynamite was 70' below ground surface (bgs). This was all fired with 1 cap. (5' ice and 65' water to top of first dynamite. Approx. 30' of charge.								
Cape Royd	1	water	200	77 34'40.79515"S	165 48'40.18351"E	-55.08	-1.46	Dec. 10	2008:345:05:17:00
comments	This shot point was moved uphill on the Island and they were drilled into ice 7-8 meters bgs. Bottom up booster w/ det cord and cap, 2bags ANFO 1 booster, 1 1/2 bags ANFO, booster, 1/2 bag ANFO. Det cord capped and shot from top to bottom. Approx. 5 to 6 meters of stemming.								
Crozier 2	5	15	500						2008:357:02:27:00
comments	This shot point had 3 holes 1 booster with cap and cord, 2 bags ANFO, 1 booster, 1 1/2 bag ANFO, 1 booster, 1/2 bag ANFO.								
FANG	3	15	300						2008:355:21:51:00
comments	These holes had 1 and 1/3 bags ANFO in each hole. 1 bag ANFO, 1booster w/cap and det cord. Top of explosives 3.79, 5.32, 3.25, respectively. Cratered.								
Cones2	3	6.13, 7.4, 5.98	100						2008:356:09:00:00
comments	This shot point 2 holes. From bottom up. 1 bag ANFO, 1booster w/cap and det cord, 2 bags ANFO, 1 booster, 1 bag ANFO. Approx. 8 meters of stemming. One hole held and one blew.								
Cones	2	14.9	200						2008:356:08:23:00
comments	1 bag ANFO, 1 booster w/cap and det cord, 2 bags ANFO, 1 booster. Approx. 14.5 meters of stemming. Blew clean. (unable to tamp stemming until 6 meters below ground surface (bgs) because only had 6 meters of drill string for tamping.								
CORR13	1	20	75						2008:356:07:50:00

Figure G.1: Shot Metadata 2008-2009 Field Season

Shot Point	#	depth	ANFO/ TNT	Location (WGS84)				Date	Time (UTC)
name	holes	(m)	hole (kg)	Latitude	Longitude	Ellipsoid Height (m)	Elev. MSL (m)	Local	yyyy:jd:hr:mn:ss
comments	This shot point had 1 bag, 1 booster w/cap and cord, 1/2 bag, Approx 5 and 3.4 meters of stemming. Note: possible void between ice/rock contact on hole 1. Approx. 4.9 and 3.5 meters of stemming, respectively. Cratered.								
Tramsw 2	2	6.8, 6.15	75						2008:356:09:45:00
comments	This shot point had 3 holes 1 bag ANFO, 1 booster with cord and 1/3 bag ANFO. Stemming 3.2, 3.4, 5.65 meters of stemming, respectively. Crater								
Sunshine Valley CornerSW	3	5.5, 5.8, 7.9	100						2008:359:00:30:00
comments	This shot point had 2 holes. 1 booster w/ cord, 1 bag ANFO, 1 booster, 1/2 bag ANFO. Stemming = 4.7 and 4.2, respectively. Crater								
HoleH	2	7.8, 8.15	75						2008:358:20:55:00
comments	This shotpoint has 2 holes. 1 booster w/ cord, 1 bag ANFO, 1 booster, 1/2 bag ANFO. Stemming is 5.4 and 5.65, respectively. Note: potential void in second hole. Crater.								
Stinky (13)	2	8.5, 8.1	75						2008:358:23:49:00
comments	This shotpoint has 2 holes. 1 booster w/cord, 1 1/2 bags ANFO, 1 booster, 1/2 bag ANFO. Stemming is 3.6 and 3.85, respectively. Crater								
Black (19)	2	7.5	100						2008:357:05:02:00
comments	This shotpoint has 2 holes. 1 booster, 1 1/2 bags ANFO, 1 booster, 1/2 bag ANFO. Stemming is 5 and 4, respectivley. Crater								
Tower (17)	2	8.7, 7.8	100						2008:357:05:28:00
comments	This shotpoint has 2 holes. 1 booster, 1 1/2 bags ANFO, 1 booster, 1/2 bag ANFO. Stemming is 5 and 5.2, respectively. Snow was sticky. Crater								
Fog (15)	2	8.6, 8.0	100						2008:357:05:55:00
comments	This shot had 2 holes. 1 booster w/ cord, 1 1/2 bags ANFO, 1 booster, 1/2 bag ANFO. Shallow holes and amount of stemming unknown. Crater								
Stuck (11)	2	6.2 7.1	100						2008:358:23:27:00

Figure G.2: Shot Metadata 2008-2009 Field Season

Shot Point	Shot Point	Location (WGS84)					Time (UTC)
ID #	name	Latitude	Latitude	Longitude	Longitude	Elevation	yyyy:jd:hr:mn:ss
4000	**Windless Bight**	77°44,8002088'S	77.74667015	167°25,5203557'E	167.4253393	38.774	2008:346:01:40:00
4001	**Cape Crozier**	77°31,2283634'S	77.52047272	169°33,4060221'E	169.556767	23.408	2008:346:00:17:00
4002	**Cape Royd**	77°34,6757798'S	77.57792966	165°48,6724012'E	165.8112067	-0.123	2008:345:05:17:00
4003	**Crozier 2**	77°31,9243266'S	77.53207211	169°04,7488243'E	169.0791471	792.162	2008:357:02:27:00
4004	**FANG**	77°29,7302642'S	77.4955044	167°14,0469502'E	167.2341158	2928.494	2008:355:21:51:00
4005	**Cones2**	77°32,0914606'S	77.53485768	167°06,1241404'E	167.102069	3494.562	2008:356:09:00:00
4006	**Cones**	77°31,7139839'S	77.5285664	167°05,0816730'E	167.0846946	3439.634	2008:356:08:23:00
4007	**CORR13**	77°31,0902241'S	77.5181704	167°05,2508532'E	167.0875142	3294.538	2008:356:07:50:00
4008	**Tramsw 2**	77°31,1863351'S	77.51977225	167°07,1808443'E	167.1196807	3421.712	2008:356:09:45:00
4009	**Valley CornerSW**	77°30,9900062'S	77.5165001	167°03,9055291'E	167.0650922	3225.665	2008:359:00:30:00
4010	**HoleH**	77°30,8005208'S	77.51334201	167°09,2198860'E	167.1536648	3424.817	2008:358:20:55:00
4011	**Stinky (13)**	77°30,8165079'S	77.51360847	167°10,7667471'E	167.1794458	3424.82	2008:358:23:49:00
4012	**Black (19)**	77°31,7519038'S	77.5291984	167°13,4745421'E	167.2245757	3461.882	2008:357:05:02:00
4013	**Tower (17)**	77°31,4493558'S	77.52415593	167°13,5119674'E	167.2251995	2928.494	2008:357:05:28:00
4014	**Fog (15)**	77°31,0684713'S	77.51780786	167°12,4120059'E	167.2068668	3466.01	2008:357:05:55:00
4015	**Stuck (11)**	77°30,3511113'S	77.50585186	167°10,7442551'E	167.1790709	3351.054	2008:358:23:27:00

Figure G.3: Shot Metadata 2008-2009 with PH5 Reference Numbers

APPENDIX H

MAPS

During the efforts of this dissertation, a set of GMT maps were generated to describe the two temporary deployments, the two shot programs, and the permanent network on the updated DEM. Figure H.1 shows an enlarged version of the entirety of Ross Island, while Figure H.2 shows a zoomed in version of the summit.

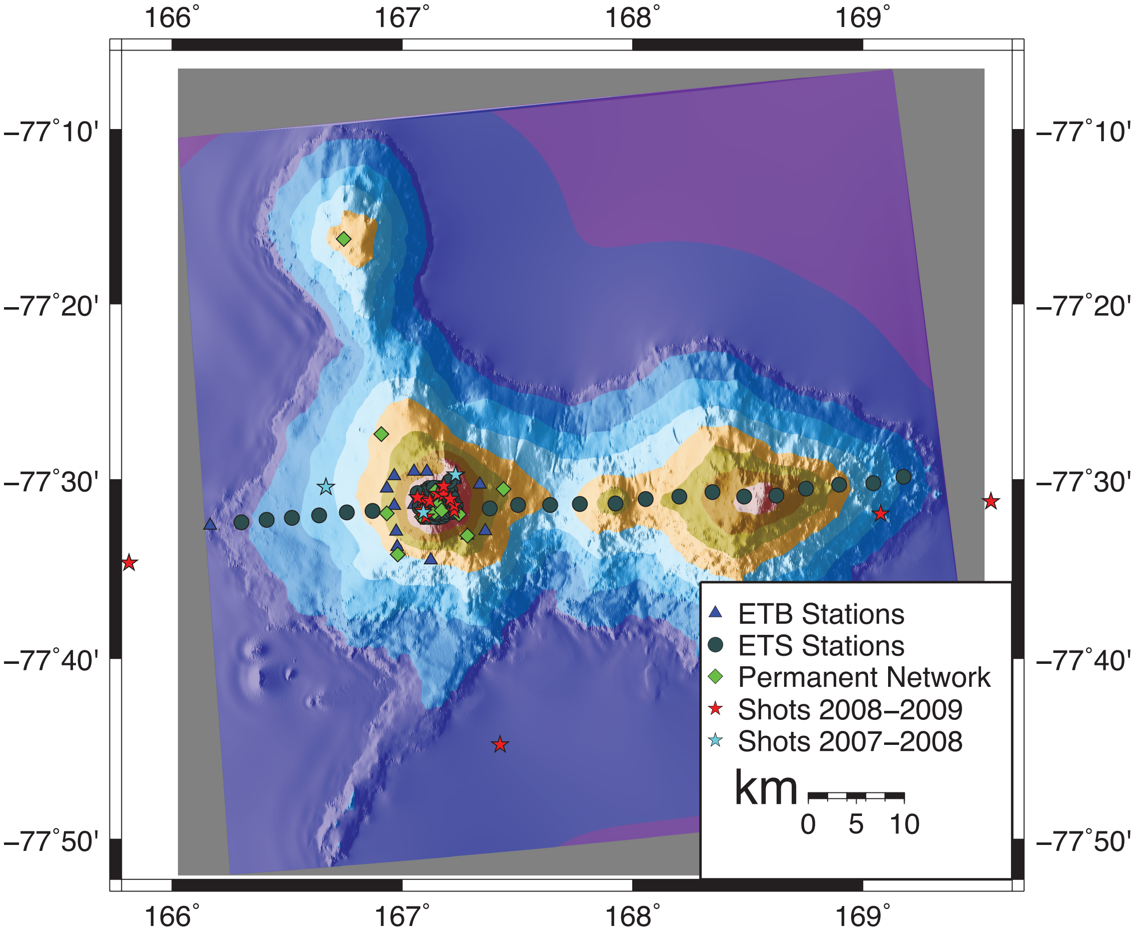

Figure H.1: DEM of Ross Island with all deployments and shot programs relevant to this work.

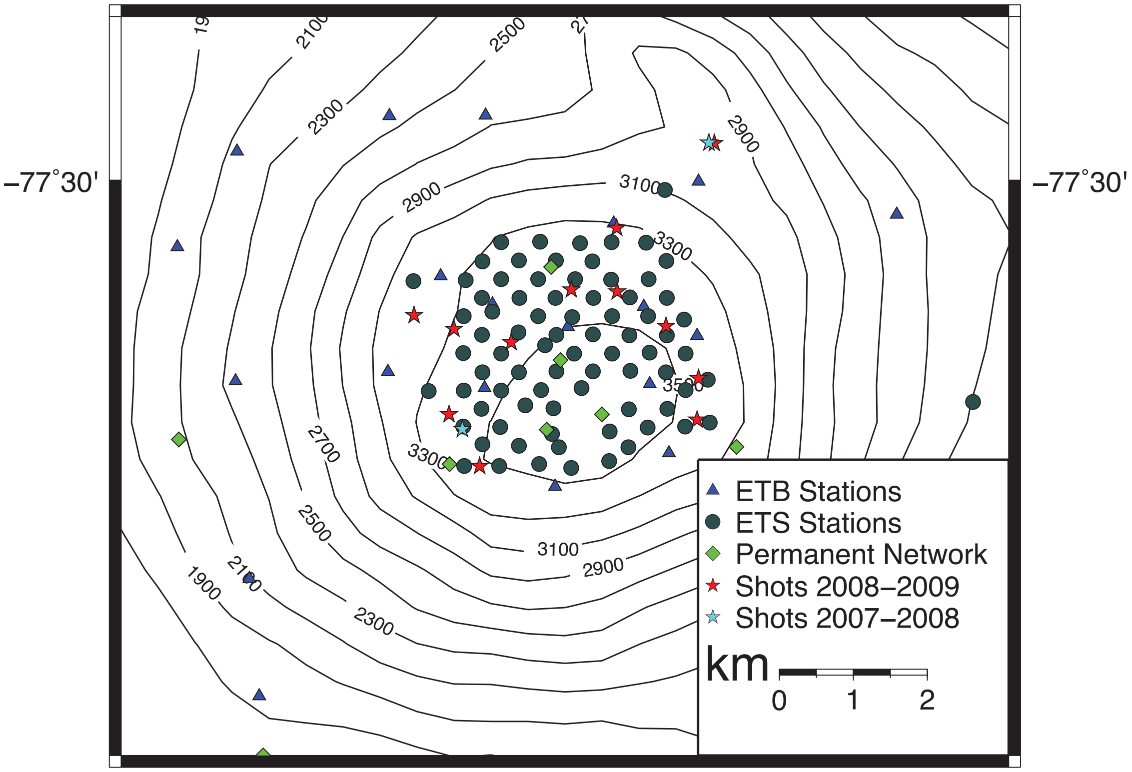

Figure H.2: Zoomed version of Figure H.1 showing the summit region.